Noise and Quasiparticle Dynamics in Single Photon, Superconducting Tunnel Junction Detectors

A Dissertation

Presented to the Faculty of the Graduate School

of

Yale University

in Candidacy for the Degree of

Doctor of Philosophy

by

Kenneth John Segall

Dissertation Director: Professor Daniel E. Prober

May 2000

© 2000 by Kenneth John Segall
All rights reserved.

Abstract

Noise and Quasiparticle Dynamics in Single Photon, Superconducting Tunnel Junction Detectors

Kenneth John Segall

2000

Superconducting Tunnel Junctions (STJs) have been studied as single photon x-ray detectors over the past several years because they combine high energy resolution with good quantum efficiency, large count rate and imaging capabilities. These detectors measure the energy of an x-ray by counting the number of quasiparticle excitations that are produced when the x-ray is absorbed in a superconducting film. The excitations are read out as an increase in the tunneling current of an STJ attached to the absorbing material. The use of two STJs with a single absorber also allows one to measure the absorption location of the photon, thus giving imaging capabilities to the detector system. We present the ongoing development of such imaging x-ray spectrometers based on Nb-Ta-Al-AlOx-Al thin film structures. These devices demonstrate an energy resolution of 25 eV FWHM for 6 keV x-rays, with a simultaneous position resolution of 0.4 μm over a detector area of 14 μm x 100 μm. This exceeds the energy resolution of conventional semiconductor detectors by almost a factor of five. A computer generated simulation models the detector response well and is used to extract the intrinsic physical parameters affecting the operation of the device. The incomplete thermalization of excited quasiparticles in the junction prior to tunneling is seen as a major effect, having significant impact on the device signal and noise. Separate experiments to quantify the known noise sources that limit the energy resolution reveal that the electronic readout is responsible for the majority of the energy width. These known noise sources combine to add up to the measured energy resolution. Such experiments suggest that with some device modification the energy resolution can be brought to within a factor of two of the theoretical limit.

Table of Contents

Table of Contents....iv
Acknowledgements....vi
List of Figures....viii
List of Tables.... x
List of Symbols and Abbreviations....xi

1 Introduction 1
  1.1 Motivation 1
  1.2 Operating Principle 3
  1.3 Thesis Organization/Previous Work 7
2 Experiment 9
  2.1 Device Design/Fabrication 9
    2.1.1 Materials 9
    2.1.2 Device Geometry 10
    2.1.3 Fabrication 12
  2.2 DC Biasing 12
  2.3 AC Current Amplifier 15
  2.4 Cryogenic Testing/Data Acquisition 18
3 Theory and Modeling 20
  3.1 Quasiparticle Diffusion 20
  3.2 Quasiparticle Inelastic Scattering/Trapping 21
  3.3 Quasiparticle Tunneling 24
  3.4 Quasiparticle Recombination 30
  3.5 Current Pulse Simulation 32
    3.5.1 Simulation Algorithm 32
    3.5.2 Junction Rate Equations 34
    3.5.3 Current Equation 36
4 Detector Physics 38
  4.1 Pulse Shapes 38
    4.1.1 Pulse Shape Fitting 38
    4.1.2 Device Parameters 43
  4.2 Dynamic I-V Curve 47
    4.2.1 Quasiparticle Energy Distribution 47

4.2.2 Charge versus Bias Voltage 49
4.2.3 Dynamic Resistance during a Pulse 50
4.3 Electron-Photon Scattering 55
4.3.1 Recombination 56
4.3.2 Thermalization 57
4.4 New Devices 58
4.4.1 Small Junction Device 59
4.4.2 Backtunneling Device 61
5 Detector Performance 63
5.1 Electronic Noise 63
5.1.1 Current Noise 64
5.1.2 Pulse Injection Tests 66
5.1.3 Noise in the Dynamic State 68
5.2 Bias Voltage Fluctuations 69
5.2.1 Energy Width 70
5.2.2 Low Frequency Amplifier Noise 72
5.2.3 Passive Voltage Bias 74
5.3 Statistical Noise 75
5.3.1 Gain/Loss Mechanisms 76
5.3.2 Energy Width 77
5.3.3 Loss, Trapping and Cancellation....................81
5.4 Energy Resolution....................83
5.4.1 Pulse Waveform Processing....................83
5.4.2 Energy Resolution....................85
5.4.3 Additional Noise Sources....................88
5.4.4 Summary....................92
5.5 Spatial Resolution....................92
5.6 Toward the Fano Limit....................94
Appendix A: Sample Parameters....................101
Appendix B: Data Analysis Proceedure....................102
Appendix C: Dates of Important Data Runs....................104
Appendix D: Active Voltage Bias Circuit Diagram....................105
References....................106

Acknowledgements

My time spent at Yale has been a lot of fun. In reading over this thesis I do get a sense of pride at what I was able to accomplish, but not without feeling a enormous amount of gratitude for those who made it possible. It is time to thank those people. I can see farther than others only because I have stood on the shoulders of giants.

My principal advisor, Dan Prober, has been everything I could ask for and more. I have valued all of my conversations with Dan and am especially grateful for his willingness to spend time with me and my questions (even late at night from his home!). He has been a role model both scientifically and otherwise and I thank him for going beyond the call of duty in my intellectual development.

I am also very appreciative of my other advisory committee members: Bob Wheeler, Peter Kindlmann, and Doug Stone. I have had many fruitful discussions with all of them, and have also had a good relationship with them outside of work. I thank them for their time spent helping me and serving on my committee. I must also thank our collaborators from NASA, Andy Szymkowiak and Harvey Moseley, who have been great supporters in our work. Andy, especially, has donated much time in guiding our efforts and being an outside reader for this thesis. He has also been a good friend. I must also, of course, thank NASA for the funding of our research.

It gives me great pleasure to thank the many graduate students who have been directly involved with this project. Mike Gaidis and Stephan Friedrich were the best mentors one could ask for, as well as being great friends. It was lots of fun to learn from both of them, especially Stephan, who was always unselfish in letting me try new things. In my mind my work is always second best to theirs. It has been fun to pass the torch to the new crew: Chris Wilson, Liqun Li, and Luigi Frunzio. Chris, especially, I have enjoyed many discussions with as well as many world traveling adventures (No Venezia...Roma!). They will all do a great job in the continuation of this work. I must also thank Andrea Davies, Rich Lathrop, Dave Toledano, Ben Mazin, Dave Schminovich and Adam Hect, who also spent time working with me on this project. A special thanks goes to Luigi Frunzio, who helped me with the editing of this thesis near its deadline.

I would also like to thank the many graduate students and postdocs who have been a constant help throughout the years, be it science conversations, group seminars, equipment training or moral support. They include the many members of Proberlab: Anurag Mittal, Peter Burke, Nick Rizzo, Jim McCambridge, Mark Keller, Alex Kozhevnikov, Irfan Siddiqi, and Rob Schoelkopf; the Clean Room Committee: Whye-Kei Lye, Brendan Gaffey, and Gabel Chong; and my classmates and friends from the start of it all: Scott Bukofsky, Craig Nakakura, and Justin Hartings.

I must also thank the staff at Yale, who were and continue to be always there for me as I bumble around the equipment, Yale forms, and quick orders: Pam Patterson, Jayne Miller, Mary Lally, Dexter Crowley, Lou Berman, Andy Morcus, and the late Marilyn Shanahan and Larry Forester.

Finally, I would like to thank my family and friends for the moral support over the last 6+ years. My friends here at Yale have kept me going, from dorm parties to meals together to conversations ranging from movies to the meaning of life. Thanks a million to Kevin Walsh, Jason Mezey, Zak Taylor, Thomas Moore, Jay Emerson, Helen Cullyer, Jason Cross, Laurie Ginsburg, Nigel Thalakada, Jake Boswell, David Legg, Rick Emery, Jim Schuck and Brendan Gaffey. And finally, my family, for whom no words can express my love and gratitude, has been the backbone of my emotional stability. Thanks Mom, Dad, Chris and Brad for everything, no matter where I go, you are still the most important people in my life. This thesis is dedicated to my uncle, Anthony LaGinestra, and my Grandfather, the late Nicholas LaGinestra, who helped instill the love of science in me from when I was a child.

Kenneth Segall, Ph.D.
February, 2000.

List of Figures

1.1.1 Transmission of atmosphere versus wavelength....................................3

1.2.1 Energy gap profile of double junction detector......................................5
1.2.2 Ideal plot of Q_1 versus Q_2..6

2.1.1 Schematic of device XN93..11
2.1.2 Schematic of device F99-14C..11
2.2.1 Junction I-V curves for XN93..13
2.2.2 Current/Voltage Bias Schematic..15
2.3.1 Schematic of composite current amplifier..16
2.3.2 Open loop gain versus frequency..18

3.2.1 Phonon scattering from E_i to E_j..23
3.2.2 Scattering times in Al versus energy..23
3.3.1 Tunneling diagram for an NIN junction..25
3.3.2 Tunneling diagram for an SIS junction, in semiconductor representation.........26
3.3.3 Subgap I-V curve for an SIS junction..28
3.3.4 Tunneling diagram for an SIS junction, in the excitation representation...........30
3.5.1 Schematic of current pulse simulation in the absorber..................................33
3.5.2 Schematic of current pulse simulation in the junction..................................33

4.1.1 Two coincident current pulses, with fit..39
4.1.2 Delay time versus absorption location, with fit..42
4.1.3 Q_1 versus Q_2 for two different temperatures, with fit..................................42
4.1.4 I_{pp1} versus I_{pp2}, with fit..43
4.2.1 Calculated energy distribution in Al trap..48
4.2.2 I-V curve in quiescent and dynamic state..49
4.2.3 Charge versus bias voltage, with fit..50

4.2.4 Peak current versus bias voltage, with fit....51
4.2.5 Simulation of R_{eff} during a pulse....51
4.2.6 Current/Charge division schematic....53
4.2.7 Q_1 versus Q_2 for different series resistances....53
4.2.8 Charge versus series resistance....54
4.3.1 Thermalization and recombination schematics....55
4.3.2 Charge versus temperature, with τ_0 varied....56
4.3.3 Charge versus bias voltage, with τ_0 varied....57
4.4.1 Q_1 versus Q_2 for small junction device....59
4.4.2 Q_1 versus Q_2 for backtunneling device....61

5.1.1 Noise schematic of current amplifier....65
5.1.2 Noise spectrum of current amplifier with junction....66
5.1.3 Energy width of injected pulses versus total current noise density....67
5.1.4 Total energy width versus voltage noise density....68
5.2.1 Noise schematic to calculate bias fluctuations....70
5.2.2 Bias fluctuations versus averaging time....71
5.2.3 Noise spectrum of current amplifer with 100 Ω resistor....72
5.2.4 Low frequency noise spectra with different blocking capacitors....73
5.2.5 Passive voltage bias schematic....74
5.3.1 Cascading of statistical noise....81
5.3.2 Trapping noise versus multiplication factor α....82
5.3.3 Statistical noise from absorber loss and cancellation versus signal gain....82
5.4.1 Q_1 versus Q_2 after filtering....84
5.4.2 Q_{tot} vs. x_0 after correcting for loss....85
5.4.3 Q_{tot} vs. x_0 for two different location cuts....86
5.4.4 Histogram of total charge with fitted energy resolution....87
5.4.5 Device schematic....90
5.6.1 Charge collection versus tunnel time....96
5.6.2 dE/dV versus bias voltage....96

List of Tables

4.1 Dependence of current pulse measurements on model parameters.............41

4.2 Device parameters for F99-11C and F99-14C.....................................58

4.3 Extracted fit parameters for XN93 and F99-11C..................................61

5.1 Statistical noise processes..80

5.2 Total noise budget..88

5.3 Energy width due to digitizing noise...91

5.4 Predicted resolution for new devices/experimental changes......................99

List of Symbols and Abbreviations

α	Trapping multiplication factor
α_L	Absorber loss parameter
A_{Jct}	Junction Area
A250	Amptek 250 transimpedance amplifier
Al	Aluminum
A_{OL}	Current amplifier open loop gain
B	Effective bandwidth
β	Quasiparticle loss fraction
BCS	Bardeen, Cooper and Schrieffer theory on superconductivity
C	Capacitance
C_{blk}	Blocking capacitor
CCD	Charge coupled device
D	Diffusion constant
D_{Al}	Aluminum diffusion constant
D_{exp}	Experimental diffusion constant
D_{normal}	Diffusion constant in normal metal
D_{Ta}	Tantalum diffusion constant
D_{th}	Theoretical diffusion constant
d_{trap}	Trap thickness
δ	Energy semi-interval
Δ	Energy gap
Δ_{Al}	Aluminum energy gap
Δ_{Ta}	Tantalum energy gap
ΔQ	Charge fluctuation
ΔQ_1	Charge fluctuation in Junction 1
ΔQ_2	Charge fluctuation in Junction 2
Δx_o	Photon spatial resolution
ΔE	Energy resolution
ΔE_{biasV}	Bias voltage fluctuation energy width
$\Delta E_{creation}$	Charge creation fluctuation energy width
ΔE_{FWHM}	Full-Width-Half-Maximum energy resolution
$\Delta E_{statistics}$	Statistical energy width
$\Delta N_{created}$	Fluctuation of the number of created quasiparticles
ΔV	Signal voltage bin size

ΔV_{rms}	Root-Mean-Square bias voltage fluctuations
ΔV_{tot}	Total bias voltage fluctuations
e	Elementary charge (1.609 x 10^{-19} Coulomb)
ε	Minimum excitation energy
E	Photon energy
E_f	Fermi Energy
e_{FET}	FET voltage noise density
E_i	Different quasiparticle energy
E_{phonon}	Phonon energy
e_s	Arbitrary voltage noise density
e_{tot}	Total voltage noise density
E_1^{qp}	Excitation energy for quasiparticle 1
E_2^{qp}	Excitation energy for quasiparticle 2
E_r	Right electrode excitation energy
E_x	X-ray photon energy
f	Frequency
F	Fano Factor
F_{eff}	Effective Fano Factor
F99-11C	Small junction device, 1999
F99-14C	Backtunneling Device, 1999
FET	Field Effect Transistor
FWHM	Full-Width-Half-Maximum
G	Goldie Factor for backtunneling
γ	Cancelled charge fraction
h	Planck constant
Jct 1	Junction 1
Jct 2	Junction 2
k	Momentum
K	Kelvin
K_α	Manganese emission duplet lines at 5895 eV
$K_{\alpha 1}$	Manganese emission duplet line at 5899 eV
$K_{\alpha 2}$	Manganese emission duplet line at 5888 eV
K_β	Manganese emission singlet line at 6490 eV
k_B	Boltzman constant
k_f	Fermi Momentum
I	Current

$I(t)$	Total detector current
I_1	Pulse peak current in junction 1
I_2	Pulse peak current in junction 2
I_A	Amplifier current
I_{bias}	Bias current
I_{dc}	DC detector current
I_{int}	Absorber-trap interface current
i_n	Current noise density
I_{nn}	Normal tunneling current
$i_{n,tot}$	Total current noise density
$i_{n,parallel}$	Parallel current noise density
I_{pp}	Pulse peak current
I_{tun}	Total tunneling current
$I_{x\text{-}ray}$	Excess x-ray triggered current
IR	Infrared
λ	Crank-Nicholson coefficient
L_{abs}	Absorber Length
L_{Jct}	Junction Length
l_{trap}	Trapping decay length in aluminum
l^*_{trap}	Equivalent trapping decay length in tantalum
m_I	(Energy resolution) versus (Total current noise density) fitted slope
m_V	(Energy resolution) versus (Total voltage noise density) fitted slope
M	Number of energy levels
n	Average quasiparticle tunneling number
n(x)	Quasiparticle spatial distribution
N	Quasiparticle number
N(E)	Density of states
N_o	Number of created quasiparticles
N_x	Excess quasiparticle number
n_{th}	Quasiparticle thermal density
N_{th}	Thermal quasiparticle number
$N_l(E)$	Left electrode density of states
$N_r(E)$	Right electrode density of states
$N_{created}$	Number of created quasiparticles
$N_{ce}[E_i]$	Number of quasiparticle in the counterelectrode at about energy E_i
N_{lost}	Number of quasiparticles lost in the absorber

N_{mult}	Number of quasiparticles that multiply upon trapping
N_{net}	Net number of tunneling events
N_{rev}	Number of reverse tunneling events
$N_{trap}[E_I]$	Number of quasiparticle in the trap at about energy E_I
Nb	Niobium
NIN	Normal metal-Insulator-Normal metal
p, q	Probability in binomial distributions
PVB	Passive voltage bias
Q	Total collected charge
Q_{center}	Charge collected for events near the absorber center
$Q_{created}$	Charge of created quasiparticles
Q_{edge}	Charge collected for events near the absorber edge
Q_{net}	Net charge of tunneling events
Q_{tot}	Total collected charge
Q_o	Initial quasiparticle charge, including multiplication
Q_1^{edge}	Charge collected in junction 1 for events near the absorber edge
Q_2^{edge}	Charge collected in junction 2 for events near the absorber edge
Q_1	Charge collected in junction 1
Q_2	Charge collected in junction 2
R	Quasiparticle recombination rate per unit density
R	Resistance
R_A	Amplifier resistance
R_{eff}	Effective junction resistance
$R_{eff,PVB}$	Passive voltage bias effective resistance
R_f	Feedback resistance
R_{inj}	Injection resistance
R_{Jct}	Junction resistance
R_{lead}	Lead resistance
R_{nn}	Tunnel barrier resistance in normal state
$R_{parallel}$	Parallel resistance
R_{quies}	Quiescent differential resistance
R_s	Series resistance
RF-SET	Radio Frequency Single Electron Transistor
SIS	Superconducting-Insulator-Superconducting
STJ	Superconducting Tunnel Junction
σ_n	Root-Mean-Square of the average quasiparticle tunneling number

$\sigma_{N_{net}}$	Root-Mean-Square of the net number of tunneling events
σ_{N_o}	Root-Mean-Square of the number of created quasiparticles
σ_α	Root-Mean-Square of the absorber-trap multiplication factor
σ_β	Root-Mean-Square of the quasiparticle loss fraction
σ_γ	Root-Mean-Square of the cancelled charge fraction
T	Temperature
$\|T\|^2$	Tunnel matrix square modulus
T_{bath}	Cryogenic bath temperature
T_c	Critical temperature
T_{eff}	Effective temperature
t_i	Time step
τ	Averaging time
τ_{delay}	Delay time
τ_{loss}	Loss time
τ_o	Material dependent electron-phonon coupling strength time constant
τ_{out}	Outdiffusion time
τ_{rec}	Recombination time
$\tau_{rec,eq}$	Equilibrium recombination time
τ_s	Scattering time
$\tau_s[E_i,E_j]$	Scattering time from E_I to E_J
τ_{self}	Self-recombination time
$\tau_{thermal}$	Thermal recombination time
τ_{trap}	Trapping time
τ_{tun}	Tunneling time
$\tau_{tun,ce}$	Tunneling time in the counterelectrode
$\tau_{tun,NIN}$	NIN junction tunneling time
$\tau_{tun,SIS}$	SIS junction tunneling time
$\tau_{tun,tr}$	Tunneling time in the trap
Ta	Tantalum
U(x,t)	Spatial and temporal quasiparticle distribution
UV	Ultraviolet
V	Voltage
V_{ce}	Counterelectrode volume
V_{ce+w}	Counterelectrode and wiring volume
V_{dc}	Bias voltage

V_{int}	Integrator and filter output voltage
V_{jct}	Junction voltage
V_{out}	Current amplifier output voltage
V_{signal}	Signal voltage
V_{trap}	Trap volume
x_i	Position mesh step
x_n	Different photon absorption location
x_o	Absorption location
X,V,U,W	Independent casual variables
XN93	X-ray imaging spectrometer, 1993
ω	Frequency
ω	Energy to charge conversion factor
Ω	Phonon energy
Ω_{max}	Maximum phonon energy
Ω_{min}	Minimum phonon energy

Chapter 1: Introduction

Scientific and technological advancements are often preceded by an improvement in measurement capabilities. In recent years there has been an increase in research activity in the development of new detection techniques for single particles and photons. Many of these new detectors work at cryogenic temperatures, as the small excitation energy in detector materials that are cooled to near absolute zero results in improved sensitivity. In this dissertation we describe the ongoing development of a new kind of cryogenic detector based on Superconducting Tunnel Junctions (STJs). These devices are designed to detect photons in the energy range 0.1 to 10 keV, for applications in x-ray astronomy. The theoretical predictions for their performance well exceed that of existing technology. The detectors have been demonstrated to work in previous laboratory experiments and at the writing of this thesis are now starting to be considered for potential use in actual astronomical observations.

A flurry of activity has occurred in the last ten years in the area of cryogenic detectors. Initial development efforts which began in the early 1980s were aimed at improving scientific measurement capabilities, primarily in high energy astrophysics, particle physics, and nuclear physics. Recently, however, applications are being explored in a wider array of scientific *and* technological fields including biophysics, semiconductor materials analysis, DNA sequencing, ultra-violet and x-ray fluorescence analysis, optical and infrared astronomy and dark matter searches. The detectors are no longer just used to study the detector physics, either; real experiments and applications are being carried out. The conference proceedings track the development in the field [Cooper, 1997; Ott, 1996; Labov, 1993]. Here we will be mostly concerned with detectors for x-ray astrophysics, since that is the application for which we are funded. However, it is important to recognize that our detector work is relevant for many of these broader applications as well.

1.1 Motivation

X-ray astrophysics has been in existence since the early 1960s, when the first celestial x-ray sources were discovered. Today it is a major part of the "all wavelength" astronomy that is being carried out by astronomers all over the world. There are over 60,000 classified x-ray sources in the sky, many of them having unexplained phenomena. An excellent review of x-ray astronomy is given in the book "Exploring the X-ray Universe", by Charles and Seward [Charles, 1995].

The types of objects that emit x-rays include those with surface temperatures of order one million degrees (10^6 K). Most stars have temperatures of order thousands of degrees, so for a long time it was believed that there were no astronomical x-ray sources. Ranging from the exotic to the mundane, there are presently seven major classifications of celestial x-ray sources:

- Supernova remnants
- Active galactic nuclei
- Accretion disks in binary systems
- Interstellar gas
- Stellar corona
- Gas in galactic clusters
- Diffuse x-ray background

The type of x-ray emissions from these sources include blackbody radiation, bremsstrahlung radiation, synchrotron radiation and emission from atomic transitions. In studying these objects one wants to know things like elemental abundance, electron temperature, electron density, and source velocity. The best method to measure these quantities is through high resolution spectroscopy. Energy resolutions of order a few eV out of several keV are needed to provide model-independent information. This is the primary motivation for the introduction of low temperatures to such experiments.

X-rays from outer space do not penetrate the earth's atmosphere. In Fig. 1.1.1 we show the transmission of the earth's atmosphere as a function of photon energy. Plotted is the altitude by which half of the flux at a given wavelength is attenuated. One can see from the plot that most x-rays are only visible from a rocket or satellite. This is the fundamental challenge in doing x-ray astrophysics, as even simple observations present significant engineering efforts. One must keep this in mind when developing a new detector.

The present x-ray detector technology consists of two major classes of detectors: dispersive gratings and non-dispersive ionizing detectors. Dispersive gratings have very good energy resolution ($\approx$ 1eV), but poor quantum efficiency. The non-dispersive class of detectors includes CCD's, solid state spectrometers and micro-channel plate detectors. They rely on the creation of excitations in a material by an absorbed photon, where the number of excitations are proportional to the photon's energy. They all have good quantum efficiency, but have energy resolution that is less than ideal ($\approx$ 100 eV) due to intrinsic fluctuations in the number of excitations created. Because of its smaller excitation energy ($\approx$ 1 meV compared to $\approx$ 1 eV for a semiconductor), superconducting detectors are predicted to have much better energy resolution without sacrificing quantum efficiency. That is the primary motivation for our work.

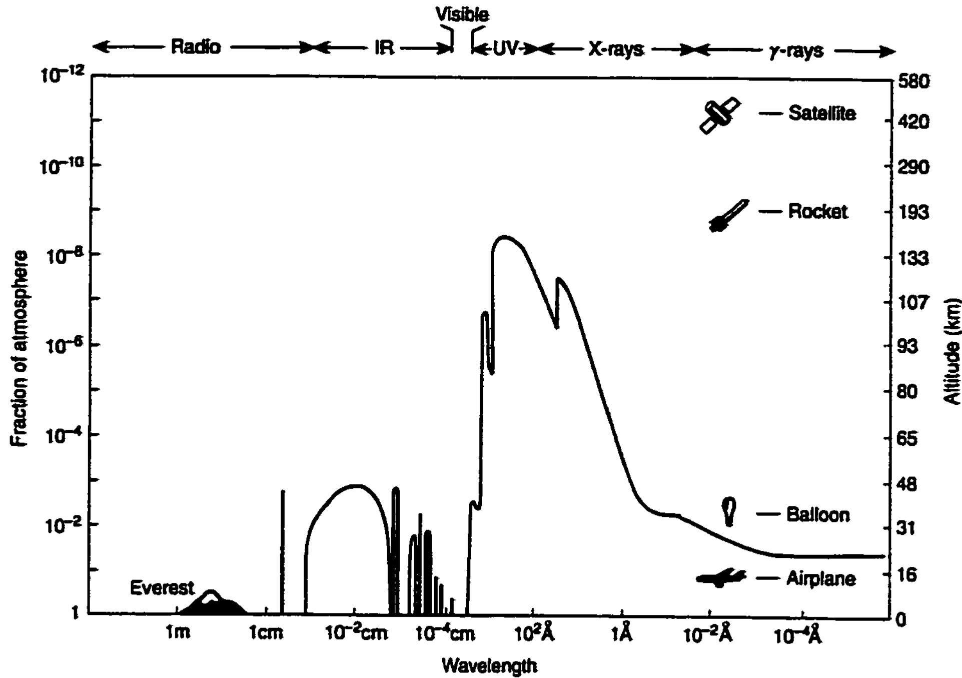

Fig. 1.1.1: Transmission of electromagnetic radiation by the earth's atmosphere. The solid lines show the altitude by which half the radiation from space has been attenuated. From Charles, 1995.

In addition to high energy resolution, imaging capabilities (spatial resolution) are also a desired detector characteristic. An increase in the spatial resolution of the detector allows one to resolve individual objects in crowded fields of view, and to image fine details in spatially extended sources. With the addition of cryogenic temperatures to these experiments, other issues like power consumption, complexity and heat dissipation from the signal amplifiers are problematic as well. Thus one would ideally like to get spatial information with as few readout channels and amplifiers as possible. This provides the motivation for our choice of detector design and experiments.

1.2 Operating Principle

X-rays absorbed in a superconducting material relax their energy through electron-electron interactions, electron-phonon interactions and phonon pairbreaking. In a time of order 100 ns the x-ray energy is converted into low energy quasiparticle excitations and subgap phonons. The number of quasiparticles that are created, $N_{created}$, is equal to the x-ray energy, E_x, divided by the minimum excitation energy ε:

$$N_{created} = \frac{E_x}{\varepsilon}. \qquad (1.1.1)$$

A naive estimate for the value of ε would be just Δ, the energy gap in the superconductor. However, since some of the energy is converted into phonons, the value of ε is somewhat higher. Kurakado [Kurakado, 1982] calculates from Monte Carlo simulations that $\varepsilon \approx 1.7\Delta$. This value for ε is significantly smaller than for semiconductors, due to the size of the superconducting energy gap.

The basic operation of our detectors is simple: a measurement of $N_{created}$ gives a measurement of E_x. Such a measurement is ultimately limited by statistical fluctuations in the number of quasiparticles created. The distribution for $N_{created}$ is Poisson-like, and as such it has fluctuations $\Delta N_{created}$ proportional to $\sqrt{N_{created}}$. A useful measure of the energy resolution in general is the full-width-at-half-maximum of a spectral line, ΔE_{FWHM}. The energy resolution expected from the statistics of the creation is given by:

$$\Delta E_{FWHM} = 2.355 \frac{\Delta N_{created}}{N_{created}} E_x = 2.355\sqrt{F\varepsilon E_x}, \qquad (1.1.2)$$

where F is called the Fano factor [Fano, 1947] and is equal to 0.2 in most superconductors [Kurakado, 1982]. The fact that the Fano factor is less than one means that the resolution is better than uncorrelated statistics (i.e. true Poisson behavior), for which F would equal one. One can see that the resolution scales with the square root of ε, which is why superconductors have a predicted resolution significantly better ($\approx$30) than semiconductors.

The method to read out the number of quasiparticle excitations is to use an STJ. An STJ consists of two superconductors separated by an insulator which is thin enough for quantum mechanical tunneling to take place. For finite bias voltages applied to the junction which are less than the gap voltage $2\Delta/e$, where e is the electron charge, the quasiparticles in the superconducting electrodes can tunnel while the Cooper pairs cannot. At zero temperature, there are no excited quasiparticles and thus no current. At finite temperatures, there is a small tunneling current proportional to the number of thermally excited quasiparticles. This is referred to as the subgap current. If an x-ray is absorbed in one of the electrodes, the x-ray deposits its energy and creates excess quasiparticles. The excess quasiparticles tunnel and cause a temporary increase in the subgap current. This current increase is read out by an amplifier and its integral, the total charge, is proportional to the energy.

While this basic operation is in principle very simple, several factors can serve to degrade the performance. The most basic difference between these superconducting

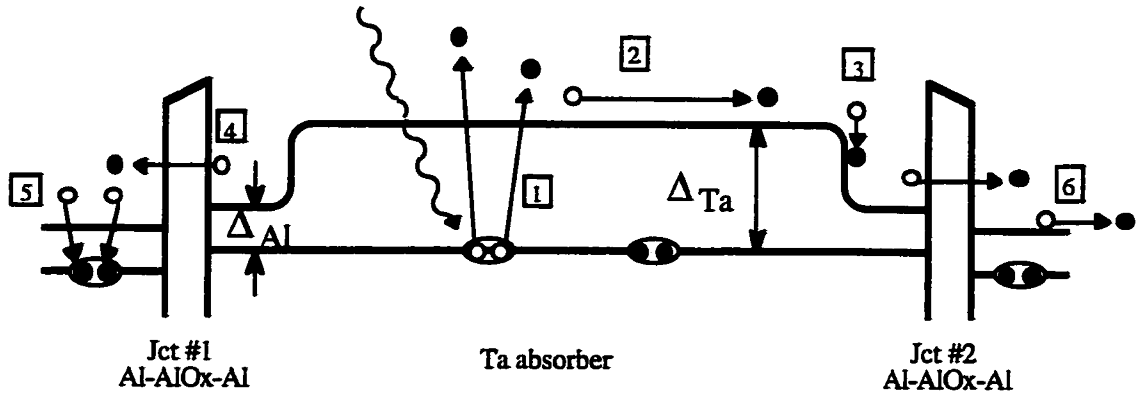

Fig. 1.2.1: Energy band diagram of our double-junction detector. The important quasiparticle processes are indicated: 1. Quasiparticle Generation, 2. Quasiparticle Diffusion, 3. Quasiparticle Trapping, 4. Quasiparticle tunneling, 5. Quasiparticle recombination, 6. Quasiparticle outdiffusion from the counterelectrode.

detectors and semiconducting detectors comes from the inability of superconductors to sustain an electric field. The quasiparticle transport in the superconducting electrode to the tunnel barrier must take place by diffusion instead of by electric field induced drift. In order for all of the charge to be collected, it is essential that the quasiparticles tunnel quickly before they recombine to form Cooper pairs. For this purpose, then, one would want to make the electrodes of the STJ as thin as possible, to decrease the diffusion time and increase the attempt frequency of quasiparticles impinging on the barrier. However, in order to absorb a large fraction of x-rays, one would want to make the electrode as thick as possible. These conflicting requirements make the simple approach described above somewhat impractical.

The solution to this problem is to use superconductor bandgap engineering, often referred to as quasiparticle trapping. The idea is to use superconductors of different size energy gaps to control the flow of quasiparticles. In Fig. 1.2.1 we show the energy diagram for our detector, which makes use of this concept. A large gap superconductor (tantalum) is put in proximity with two lower gap tunnel junctions (aluminum-aluminum oxide-aluminum). Due to its high atomic number, x-rays are absorbed mostly in the tantalum film where they generate quasiparticles. This region is called the absorber. It can be made thick to absorb a large fraction of x-rays. After being generated, the quasiparticles diffuse laterally in the absorber until they reach either of the two lower gap junctions. In these regions, called the traps, the quasiparticles scatter inelastically to lower energy and are prevented from returning to the absorber. They then tunnel through the barrier to the counterelectrode, where we detect them as an increase in the junction's subgap current. The trap regions can be made much smaller than the absorber, to ensure faster tunneling.

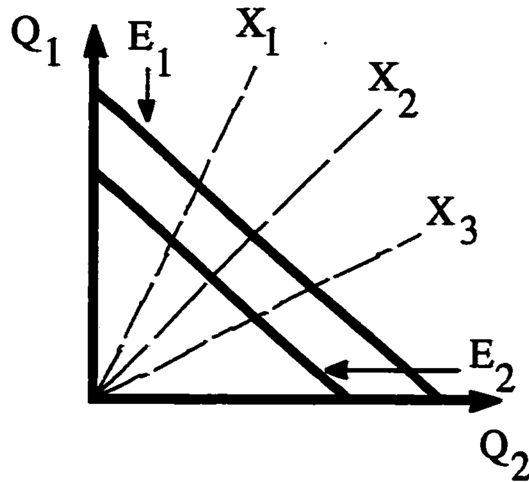

Fig. 1.2.2: Ideal plot of Q_1 vs. Q_2. Lines where $(Q_1 + Q_2)$ = constant indicate different energies (E_1, E_2), whereas lines where (Q_1/Q_2) = constant indicate different absorption positions (x_1, x_2, x_3).

After tunneling, the quasiparticles diffuse away from the counterelectrode into the leads. At any point in the process the quasiparticles can recombine to form Cooper pairs. In Fig. 1.2.1 we indicate these important quasiparticle processes.

The use of *two* junctions in our detector scheme is what allows for the intrinsic imaging capabilities. We label the junctions 1 and 2 in Fig. 1.2.1. Each photon now produces two current pulses with two collected charges: Q_1 in junction 1 and Q_2 in junction 2. The sum of the two charges is still equal to the total number of quasiparticles created initially, which is proportional to the photon's energy. However, now we can use the *ratio* of the two charges to obtain the photon's position. For example, a photon absorbed in the center of the absorber will have a ratio $Q_1/Q_2 = 1$, since both charges will be equal. A photon absorbed right next to junction 2, however, will have $Q_1/Q_2 \approx 0$, since almost all of the charge will be trapped in junction 2 while none is trapped in junction 1. Absorption events in-between will have ratios between 0 and 1, and so on. Note that it is the diffusive behavior of the quasiparticles that allows for this location extraction; if the transport were ballistic one would always collect half of the charge in each junction. The combination of energy and position information can be seen in a plot of Q_1 vs. Q_2 (Fig. 1.2.1). Lines where $(Q_1 + Q_2)$ = constant are lines of constant energy, whereas lines where Q_1/Q_2 = constant are lines of constant position. Fig. 1.2.2 is for the ideal case, with perfect trapping into the junctions and no quasiparticle losses in the absorber. If the trapping is not perfect, the plots will pull away from the edges, as there will be a finite minimum charge in each junction even for the case of absorption very close to the other junction. If there are quasiparticle losses in the absorber, the lines of constant energy will have curvature, as

events from the center must diffuse a longer average time than those from the edge and are thus more susceptible to loss.

1.3 Thesis Organization/Previous Work

At the writing of this dissertation, our work at Yale University on STJ detectors has been going on for the last ten years, with the author having been present for the last six. The program has enjoyed a reasonable amount of success, as we have achieved working detectors with good energy resolution and a good understanding of the detector physics and readout electronics. This thesis will focus on the most recent developments in our work, as we are not interested in repeating what has been said already by others. However, to form a complete picture we must first touch on the major developments leading up to the author's research. Here is our story thus far...

In the dissertation of Michael Gaidis [Gaidis, 1994] was described the work leading up to the first x-ray detection by our detectors: the initial theory and design of the detector, the choice of materials and geometry, the fabrication of high quality devices, initial DC testing and characterization, construction of the basic charge amplifier, and cryogenic testing. Devices with a 200 μm long tantalum absorber connected laterally to a single tunnel junction could resolve 6 keV x-rays with an energy resolution of 190 eV FWHM. The x-ray pulses were found to be slower than expected, along with a higher collected charge. The noise sources limiting the energy resolution were unknown.

In the dissertation of Stephan Friedrich [Friedrich, 1997b] was described the first testing of double junction detectors with spatial resolution. A new biasing circuit and current amplifier were constructed, which allowed more stable biasing and lower electronic noise (13 eV compared to 45 eV). The spatial resolution allowed the extraction of the relevant quasiparticle time scales. The cause of the slow pulses was revealed to be slow diffusion in the tantalum absorber; the large charge was revealed to result from backtunneling. The devices could resolve x-rays with an energy resolution of 54 eV over a 30 μm range of the absorber, with a corresponding spatial resolution of 1 μm. The sources of noise were still basically unknown.

In this work we will describe the extensive modeling and testing of the same devices, with the emphasis on new experiments and calculations which determine the noise sources that limit the energy resolution. Chapter 2 will review the basic experimental details, focusing on the changes made during the course of this thesis. Chapter 3 will describe the theory and modeling done by the author to determine the quasiparticle processes which contribute to the detector signal. Chapter 4 will detail the new experiments on the device physics, emphasizing the use of the modeling to extract time

scales and physical parameters. We will see a marked change in the behavior of the device during an x-ray pulse which had not been appreciated before. Finally, in chapter 5 we will review the experiments and calculations to determine the limiting factors in the energy resolution. We will end with suggestions for future work.

Chapter 2: Experiment

In this chapter we will review the details of the experiment to measure the performance of our double junction x-ray detectors. Laboratory testing of STJ detectors involves a full range of experimental challenges: device design and fabrication, DC characterization and biasing, low noise AC electronic readout, cryogenic testing, and data processing. We will give brief overview of all these topics.

2.1 Device Design/Fabrication

Despite the relatively simple operating principle for STJ detectors, the devices themselves have become rather complex. We have made efforts to choose materials and geometries which best optimize aspects of the detector performance: high x-ray absorption efficiency, efficient charge collection, durability, and good noise performance. Here we will review the important aspects of the device design and fabrication.

2.1.1 Materials

The major design considerations in choosing materials for our detectors were insensitivity to thermal cycles and energy gap size. The number of superconducting elemental metals is not particularly large, so several of the choices were relatively simple. We chose to stay with all refractory metals, as other groups have seen soft metals like lead and tin degrade with time and thermal cycles. Our devices have been thermally cycled repeatedly for over 6 years to date, and we continue to get quality performance. Bandgap engineering dictates a large gap difference between the absorber and the junction, so that is an important constraint as well. Below we list the materials for our devices:

• Absorber: One would like a high gap superconductor for the absorber, in addition to a high atomic number for good x-ray absorption properties. Tantalum is our choice, and is ideal in both respects. In addition, tantalum has no metallic oxides which could serve as trapping sites. It also has a fast electron-phonon scattering time, which results in efficient energy-to-quasiparticle conversion in the initial absorption event.

• Junction: Junctions made from aluminum (aluminum - aluminum oxide- aluminum) have a very robust oxide and display good subgap performance. In addition, aluminum also has a lower gap than tantalum, making it good for bandgap engineering. It has a much lower atomic number than tantalum, resulting in few unwanted absorption events in the junction.

Perhaps its only drawback is its slow electron-phonon scattering time, which we will explore more deeply in chapters 4 and 5.

• Contact: In constructing a double junction device one must make electrical contact to the absorber in order to be able to bias both of the junctions separately. The major constraint on the contact material is that it has a higher energy gap than the absorber, such that quasiparticles do not diffuse out of the absorber into the leads. Niobium is our choice, as its gap is over twice that of tantalum. Its drawback is that it is well known to form metallic oxides [Halbritter, 1987], which can act as trapping sites for quasiparticles.

• Wiring: The wiring leads from the counter electrode of the junctions (the geometry is discussed below) is made from aluminum in our devices. This was designed such that quasiparticles would diffuse quickly away from the junction such that they would not undergo multiple tunneling (section 3.3). This has turned out not to be the case, as the diffusion in aluminum was found to be slower than expected, and the quasiparticles in our devices tunnel on average about 2.5 times before they diffuse away.

• Substrate: The substrate plays an important role in the device performance. X-rays absorbed in the substrate create phonons which can cause an unwanted signal in one or both of the junctions. We use silicon substrates which have a layer of silicon dioxide (SiO_2) on them to act as a buffer layer for substrate phonons. We see good attenuation ($\approx$70%) of the signals from substrate events.

2.1.2 Device Geometry

The major device tested in this thesis is labeled XN93. We show its schematic in Fig. 2.1.1. The tantalum absorber is 200 μm x 100 μm, reflecting a compromise between the possibility (at the time of the design) of short quasiparticle lifetimes and the desire for large detection areas. The absorber is made thick, 6000 Å in XN93; this absorbs $\approx$ 25 % of the x-rays at 6 keV. The aluminum junctions overlap the absorber by 10 μm, such that good step coverage is ensured. The stretched out shape of the junction is chosen such that a small magnetic field can be applied while still obtaining good Josephson current suppression (see section 2.2), as there was initially a concern for keeping the value of applied magnetic field small. The length of the junction is 200 μm. In the figure we show the energy diagram and the side view, and indicate the absorber, trap, counterelectrode, and contact.

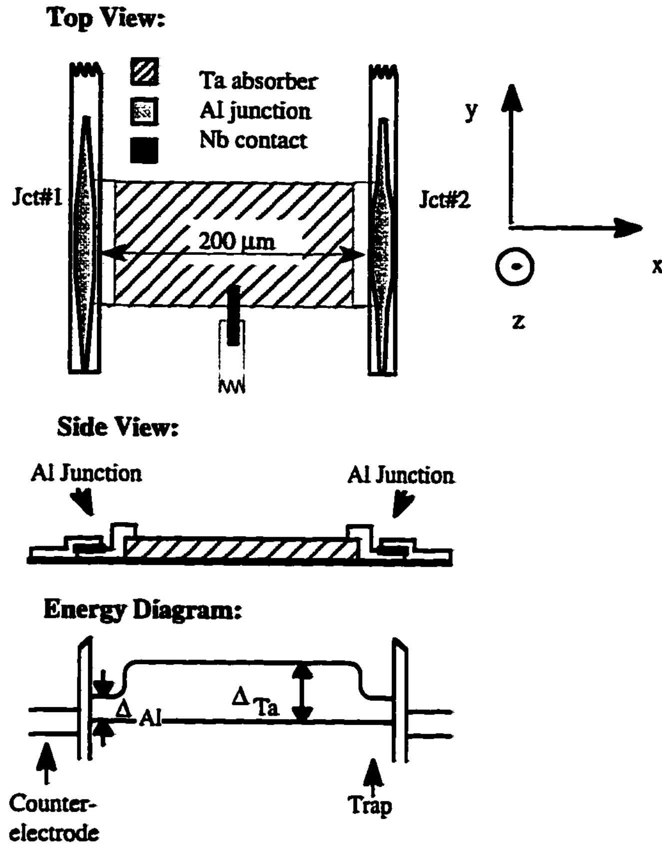

Fig. 2.1.1: Schematic of device XN93, showing the top view, side view, and energy diagram.

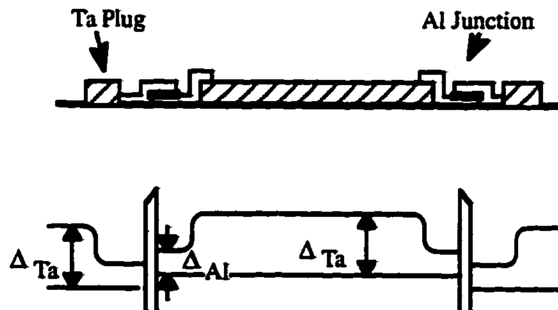

Fig. 2.1.2: Schematic of device F99-14C, showing the side view and energy diagram. The device has a Ta plug to prevent outdiffusion from the counterelectrode.

In addition to XN93, two other additional devices were tested during this thesis. The first is F99-11C, which is a device very similar to XN93 except in two respects: the junction has a smaller length (120 μm), and the wiring is wide instead of narrow along the junction length like in XN93. The other device, F99-14C, we show a side view of in Fig. 2.1.2. This device has a tantalum plug in the wiring layer. The high gap of tantalum

prevents quasiparticles from diffusing away from the junction region after they tunnel and allows us to study the effects of multiple tunneling.

2.1.3 Fabrication

The device fabrication has been thoroughly explained in the dissertation of Mike Gaidis [Gaidis, 1994], who fabricated the device XN93. The fabrication procedure has not changed since so we will just summarize it briefly here.

The tantalum absorber is sputtered at high temperatures (700 C) in order to obtain clean films with a high T_c (4.4 K). These films have a resistance ratio RRR = 30. The absorber is wet etched with a solution of iron-chloride and hydrofluoric acid. The junction is deposited in trilayer fashion, with both the aluminum trap and counterelectrode thermally evaporated. The junctions have normal state resistances (R_{nn}) of order 1 Ω and differential subgap resistances a factor of 10,000 higher. The junctions are also defined with a wet etch, using a standard aluminum etch. The niobium contact is sputtered, at room temperature. A layer of silicon monoxide (SiO) is thermally evaporated to passivate the junction. Photolithography is used to define all features in the device. An ion beam clean is performed prior to the deposition of each layer to remove any impurities and ensure good metallic contact between layers.

2.2 DC Biasing

In order to detect x-rays, STJs must be biased at finite voltages in the subgap region. To achieve optimum noise performance, it is best to bias in regions of low current and high differential resistance. The biasing of STJ detectors is not trivial by any means, as STJs have highly non-linear I-V curves, an extremely sensitive temperature dependence, and a variety of Josephson effects which can all introduce difficulties. In addition, in our experiments we must simultaneously bias *two* junctions, which can be challenging if the junctions have even slightly dissimilar characteristics.

In order to successfully bias an STJ detector, one must apply a small magnetic field ($\approx$ 10 Gauss) parallel to the junction in order to suppress the DC Josephson current. The mechanism for suppression is by phase modulation of the superconducting wavefunction on either side of the barrier [Van Duzer, 1981]. In zero field our junctions exhibit a DC Josephson current of typically around 500 μA. In order to successfully bias, one must suppress the Josephson current well below the subgap current, which is of order 20 nA. While this is achievable in a reasonably straightforward manner for a single junction, to

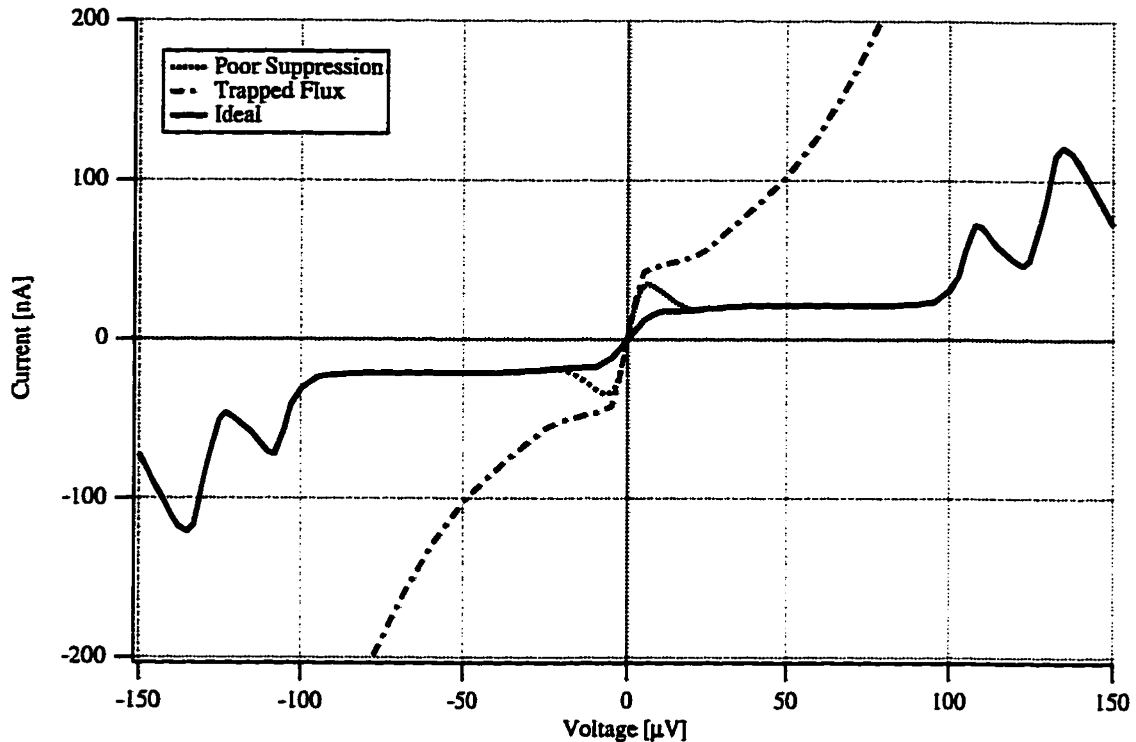

Fig. 2.2.1: Device I-V curves for XN93: ideal, with poor suppression, and trapped flux.

simultaneously suppress two junctions can be very difficult, since there will always be small differences (≈ 1-2 %) in the size/shapes of the two junctions.

In Fig. 2.2.1 we show an ideal I-V curve, along with two that are non-ideal. The ideal I-V curve has a subgap current of approximately 20 nA and a differential resistance of 15-20 kΩ in the region of 70-80 μV. This gives good noise performance. We will discuss the electronic noise more at length in section 5.1; most of the good noise performance was achieved with I-V curves that look similar to the ideal one in Fig. 2.2.1.

The first non-ideal I-V is labeled "Poor Suppression", and it is what the I-V looks like when the magnetic field does not perfectly suppress the Josephson current. The problem with imperfect suppression is that a switching instability can result, because the junction has two stable operating points – one in the subgap region and one on the zero voltage current. The result is a "bump" that occurs near zero voltage, which varies in size depending on how poor the suppression is. A small bump may not preclude successful biasing; however, the larger the bump is, the more likely an instability can result. Even a small bump can still be problematic, as we have seen poor suppression result in unwanted low frequency 1/f noise.

The other non-ideal I-V is labeled "Trapped Flux", and is what results when magnetic vortices become trapped in the junction. Flux trapping can occur in any number

of ways, most often during times of amplifier oscillation or saturation. A trapped flux I-V, as seen, increases the subgap current substantially and results in very poor noise performance. While a poorly suppressed I-V can sometimes still give good results, a trapped flux I-V more often than not signals the end of an experiment, as the junction must be warmed up above the critical temperature to drive out the vortices.

We highlight the non-ideal behavior to motivate our choice of biasing circuit. Earlier experiments in our lab had utilized a DC current bias circuit. This method simply biases the junction with a constant current source. The load line for such a circuit is horizontal, and requires near perfect suppression of the Josephson current to bias successfully. With the start of double junction experiments in our lab, we found that we could not achieve the level of suppression necessary to bias both junctions with a DC current bias. Therefore, an effort was made to switch to DC voltage bias. DC voltage bias is much more difficult to implement than DC current bias, but the benefit is significant, as the biasing becomes much more stable and the requirements on the suppression are much less strict. The I-V curves in Fig. 2.2.1 were all taken with DC voltage bias; the "Poor Suppression" I-V curve could not, in fact, be taken at all with DC current bias and its shallow load line.

The "peaks" in current on the ideal I-V at $\approx$ 110 μV and 140 μV are called Fiske modes. They are resonances of the AC Josephson field with the electromagnetic modes of the junction [Eck, 1964]. It is not advantageous to bias in their vicinity, as they give excess noise. However, the ability to trace them out without hysteresis is indicative of the stiff load line in our voltage bias circuit. We have measured a load line of approximately 6 Ω, which is practically vertical on the scale of Fig. 2.2.1.

We show our biasing circuit in Fig. 2.2.2. It actually utilizes both current and voltage bias. The voltage bias is done with an composite op-amp. It biases the junction relative to its inverting terminal, which is held at the bias voltage by feedback. The current bias is done with a voltage source and a 1 MΩ resistor. A switch allows selecting either one or the other to bias the junction. The reason for using both involves the behavior of the junction before the correct value of magnetic field is chosen. Ultimately, we want to end up using voltage bias, for the reasons stated above. However, since the voltage bias is done with an *active* circuit element, namely the op-amp, it is unstable and can saturate when presented with low source impedances. Putting is simply, it is difficult to voltage bias a short circuit. However, that is exactly what the junction behaves like if the correct value of magnetic field has not yet been set. If the junction is acting like a short and the op-amp saturates, trapped flux can result. This was the pattern of several of our experiments for a while, as quite often we could not find the correct value of magnetic field right away.

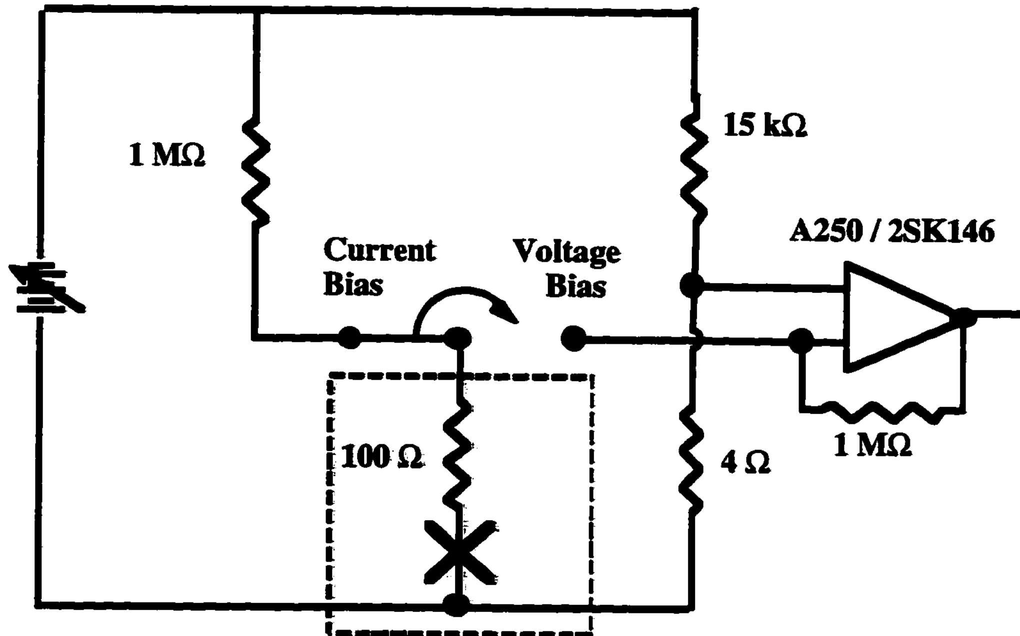

Fig. 2.2.2: Biasing circuit schematic. The circuit utilizes both current and voltage bias. The junction is represented by the X.

The current bias, however, is perfectly stable if the junction is behaving as a short. We implemented the combination of current and voltage bias to correctly select the value of magnetic field while still keeping the amplifier stable. We begin by biasing with current bias, select the correct value of magnetic field, and then switch over to voltage bias. The switch-over was problematic at first, but was solved by putting a 100 Ω cold resistor in series with the junction (see Fig. 2.2.2). The resistor seemed to be effective in attenuating any stray discharge currents from the abrupt switch-over. The resistor was made cold to reduce its Johnson noise. Future experiments may look to find ways around the extra series resistance, however, as it makes the amplifier look like more of a load to the x-ray current, resulting in unwanted charge division (see section 4.2).

2.3 AC Current Amplifier

The current pulses that result from an x-ray are typically of order 50 – 100 nA and contain signal frequencies between 1 and 100 kHz. The pulses must be amplified before they are digitized and recorded. Ideally, the noise from the amplifier will not exceed the intrinsic fluctuations of the detector. Noise considerations alone, however, do not dictate whether to use a voltage, current or charge amplifier. A charge amplifier seems appropriate, since the charge is a more direct measure of the energy of the x-ray. However, the current is more closely related to the time-dependent processes inside the

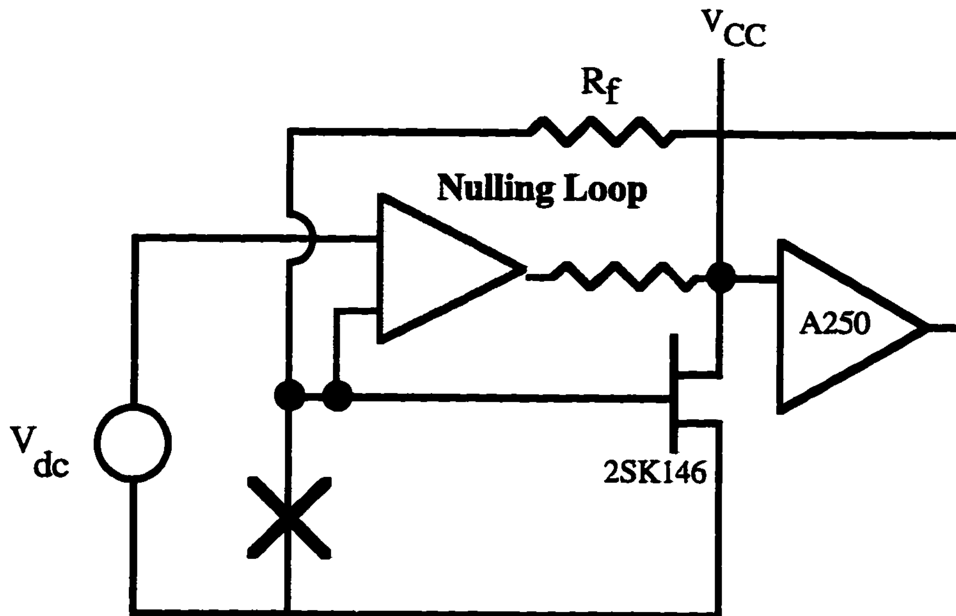

Fig. 2.3.1: Schematic of DC coupled composite amplifier. The nulling loop senses the gate voltage and feeds back to keep it fixed at the DC bias. It is indicated in gray.

detector, and as such gives additional information for device analysis. Therefore we use a current amplifier in our experiment, and obtain the charge by numerical integration in a later step. In addition to low noise, an ideal current amplifier would also have a large bandwidth for minimum pulse distortion and present a low impedance to the detector to collect the full signal.

We will discuss the electronic noise in more detail in section 5.1. The amplifier that provides the DC bias for the junction, shown in Fig. 2.2.2, also functions as the current amplifier for the pulse signal. In the figure we draw it as an op-amp, but in reality the amplifier is actually composed of a separate input FET followed by a transimpedence amplifier. By keeping the input FET separate, one can choose a FET which has low noise and is well matched to the device. We use a Toshiba 2SK146 JFET for the input, with a voltage noise of 0.4 $nV/\sqrt{Hz}$ and negligible current noise. The transimpedence amplifier that follows is the Amptek A250, which also has very good noise performance. The two act in conjunction to form a very low noise composite op-amp.

To DC couple this composite amplifier as we have done was not straightforward, however. There are complications in trying to DC couple a single FET op-amp, as we now describe. The drain voltage of the input FET is fixed by the A250 (see Fig. 2.3.1 for orientation). An appropriate drain current can be set such that the gate of the FET lies at ground, or at some chosen DC voltage. Such a composite amplifier can be DC coupled,

with the gate voltage appearing across the device. However, the drain current has a very sensitive temperature dependence, and as such will fluctuate with the ambient temperature of the environment. This causes the FET's gate voltage to fluctuate through feedback, and does not allow very stable DC biasing. Industrial op-amps which are DC coupled use a differential matched pair of transistors to circumvent this problem, using two FETs whose temperature dependencies cancel one another. However, it is very difficult to find good matched pairs with a high level of noise performance. We have not had success using a differential pair input FET.

Our solution to the problem was to add extra circuitry that compensates for the temperature drift of the FET's drain current. We added a so-called "nulling loop", whose purpose was to sense the gate voltage and add additional drain current accordingly in order to keep the gate voltage at the DC bias. Figure 2.3.1 shows the idea, with the nulling loop indicated. The nulling loop consists basically of an op-amp and a resistor, along with a filter (not shown in the schematic). The filter ensures that this "correcting" of the drain current only occurs at low frequencies, where the biasing is critical, while not interfering with the amplification at signal frequencies. This approach was met with success, as we were able to DC couple the composite amplifier while maintaining the good noise performance in the signal band. The details of the design and operation of the nulling loop and the current amplifier have been published [Friedrich, 1997a; Friedrich, 1997b]. A full circuit diagram showing all the details of the composite amplifier is also shown in Appendix D.

In addition to the requirements for noise and DC coupling, ideally one also wants the current amplifier to present a low impedance to the junction. This is an issue that is was not appreciated as much until recently, when we learned that the device resistance changes by almost an order of magnitude during a pulse (see sections 4.2 and 5.1). The resistance presented to the junction by the current amplifier, R_A, can be approximated as R_f/A_{OL}, where R_f is the feedback resistor and A_{OL} is the amplifier's open loop gain. In Fig. 2.3.2 we show the measured open loop gain as a function of frequency. The value of A_{OL} is around 10,000 in the signal band, so for a feedback resistor of 1 MΩ the value of R_A is approximately 100 Ω. We will use this number later in section 4.2.

In Fig. 2.3.2 we also show the open loop gain for different values of compensation capacitance connected to the A250. One can see a "peaking" in open loop gain for values of compensation capacitance less than a few pF. Similar peaking also occurs in the noise spectra. This is a sign of marginal phase stability of the current amplifier. The peaking is essentially an RLC resonance, as the amplifier behaves like an inductor since it has a gain which decreases with frequency. The compensation rolls off the open loop gain at lower

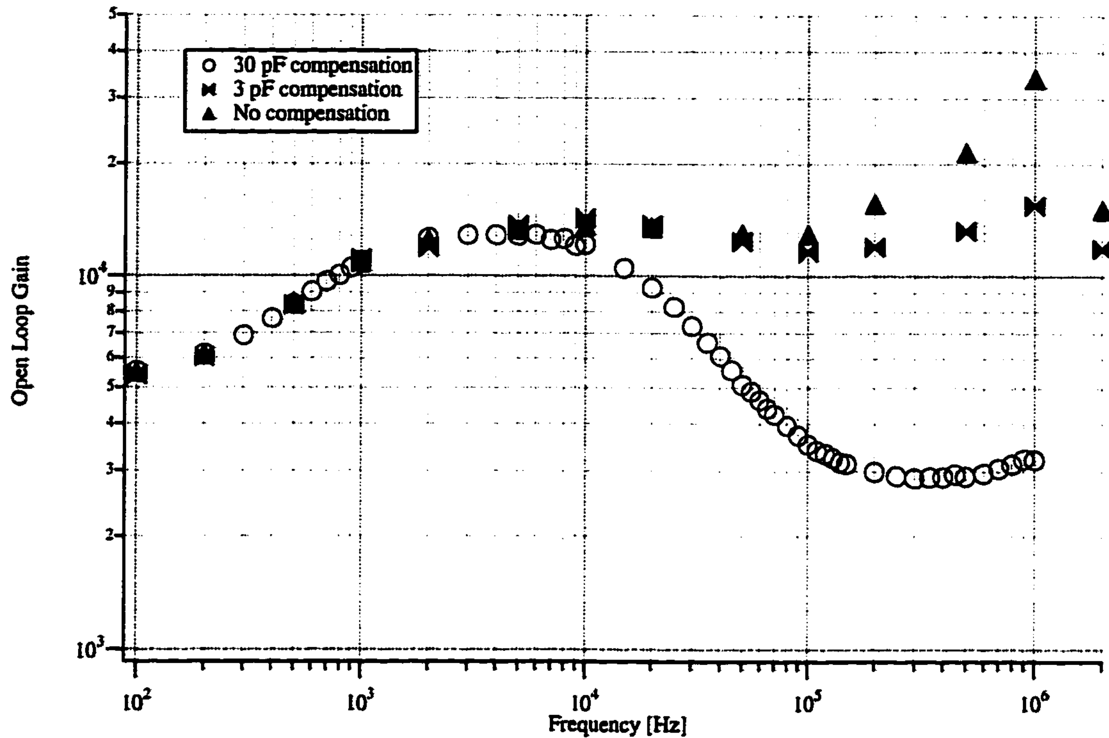

Fig. 2.3.2: Open loop gain versus Frequency, for different values of compensation capacitance.

frequency to help keep the loop stable and avoid the resonance. From the graph, 30 pF of compensation capacitance appears to be enough. We believe the peaking was affecting the device performance, so we now use 30 pF compensation for all experiments; we did in fact see an improvement in the energy resolution of ≈ 20% for the device by doing this.

The bandwidth of the current amplifier, f_c, is set by the capacitance in the feedback loop, C_f: $f_c = (2\pi R_f C_f)^{-1}$. In addition to increasing the compensation capacitance, we also found that increasing the feedback capacitance also helped with the phase stability. Earlier experiments had a feedback capacitance of approximately 0.5 pF, but recently we have found C_f values of order 1 pF are better. This helps the stability but limits the bandwidth, $f_c \approx 170$ kHz. This is fine for good energy resolution but results in some amount of pulse distortion. The pulse distortion can be problematic when trying to extract physical timescales from the current pulses. In the future we will use a lower feedback resistor for experiments where we would like to look at undistorted waveforms, and use our usual R_f = 1 MΩ to measure the energy resolution.

2.4 Cryogenic Testing/Data Acquisition

The use of aluminum as a junction material requires low temperatures (< 0.3 K) for good noise performance and large signals. We test our devices in a 2-stage ^{3}He cryostat.

The cryostat attains a base temperature of ≈ 0.22 K with a hold time of 8 - 12 hours. A Germanium Resistance Thermometer (GRT) from Lakeshore Cryogenics is used to measure the temperature; however, we have found that we cannot keep the thermometer connected while biasing the junctions, as there appears to be electromagnetic interference between the junction lines and the digital voltmeter that is used to monitor the GRT. Therefore we use the temperature dependence of the subgap current as our "thermometer" during an actual data run. The observed subgap current of ≈ 20 nA in our junctions agrees well with the BCS prediction for a temperature of 0.22 K with junctions of our resistance; this temperature was separately measured by the thermometer and also predicted by the various heat leaks into the cold stage in our cryostat [Friedrich, 1997b]. Details on the wiring and sample mount inside the cryostat have been described previously [Gaidis, 1994].

We illuminate the device with an ^{55}Fe x-ray source which emits 2 Mn lines: K_α at 5890 eV, 88%, and K_β at 6490 eV, 12%. The K_α line is actually composed of 2 lines itself spaced within a few eV of each other; we will see this is relevant when we try to fit the charge histograms from our device in chapter 5. The source is on a mechanical rotating arm which can be turned away to verify that all the events are in fact x-ray induced. The x-ray pulses which are amplified by the pulse amplifier are sent to an oscilloscope: either an HP33120A from Hewlett Packard, or more recently an Integra 40 from Nicolet Instruments. The Integra 40 has twelve bits of voltage resolution which reduces the digitizing noise (see section 5.4) and also has the ability to take very long time traces (≈ 10^6 points). The latter is useful in taking noise spectra, as one can sample at a high frequency to avoid aliasing while still maintaining low frequency information. The digitized waves are downloaded to disk where we can do analysis on the unfiltered waveforms for detector physics and then apply digital filtering routines to filter out the electronic noise and obtain the optimum energy resolution. The digital filtering and the Fourier transforms to obtain noise spectra are done using standard LabVIEW routines.

Chapter 3: Theory and Modeling

The excess quasiparticles which are generated by an absorbed photon in our detector are subject to many physical processes before they are counted as a charge in our amplifier. The major processes include quasiparticle diffusion, inelastic scattering, tunneling and recombination. In this chapter we will introduce the theory and modeling of these processes, taking each one individually. Then we will discuss how we have incorporated all the processes into a single model of the current pulse. The model generates a full theoretical current pulse which can be compared directly with the digitized pulses from our amplifier. In this chapter we will review the development of the model, and then in Chapter 4 we will apply it to the data from our experiment.

To fully determine the shape of the current pulse, one would in general want to know the time evolution of the location *and* energy of each excited quasiparticle in the detector. This would lead to a very complicated analysis, so we have made two important simplifications in our model: we ignore the energy distribution in the absorber and ignore spatial effects in the junction electrodes. Both in fact are fairly good approximations. The scattering times in the tantalum absorber are relatively fast, so we can assume that all quasiparticles thermalize to near the gap energy fairly quickly, before the quasiparticles diffuse a significant distance. Effects from a non-zero energy spread in the absorber should thus be small. The trap has a much smaller volume than the absorber and aluminum has a much larger diffusion constant than tantalum, so quasiparticles in the trap should spread out to a spatially uniform distribution very quickly. Thus assuming a uniform spatial distribution in the trap is fairly accurate as well. The lateral diffusion in the absorber and the energy dependence of quasiparticles in the junction are the major effects in determining the signal, so this is where we have concentrated our modeling efforts.

3.1 Quasiparticle Diffusion

Following the absorption of an x-ray, the excess quasiparticles propagate through the absorbing film by diffusion. A diffusion framework is appropriate because typical quasiparticle mean free paths (tenths of microns) are much smaller than typical device dimensions (tens of microns). We use the one-dimensional diffusion equation to describe the spatial and temporal distribution $U(x,t)$ of quasiparticles in the absorber:

$$\frac{\partial U}{\partial t} - D\frac{\partial^2 U}{\partial x^2} = 0. \qquad (3.1.1)$$

Here D is the diffusion constant, in the usual manner. The x direction is the direction connecting the line drawn between the two junctions (see chapter 2 for orientation). The film is thin enough to ignore the z direction. If we assume specular reflection at the edges of the film, the y-dependence cancels out as well.

There are several methods to treat the diffusion equation numerically [Press, 1989; Burden, 1989]. We have chosen the Crank-Nicholson formalism because it offers unconditional stability and is accurate to first order in both space and time. We assume a spatial grid of spacing dx and time steps of size dt. For a given value of x and t, we first take the forward time difference of equation (3.1.1) at time t:

$$\frac{U(x,t+dt)-U(x,t)}{dt}-D\frac{U(x+dx,t)-2U(x,t)+U(x-dx,t)}{(dx)^2}=0 \tag{3.1.2}$$

We can also take the backward time difference at time (t + dt):

$$\frac{U(x,t+dt)-U(x,t)}{dt}-D\frac{U(x+dx,t+dt)-2U(x,t+dt)+U(x-dx,t+dt)}{(dx)^2}=0. \tag{3.1.3}$$

The average of equations (3.1.2) and (3.1.3) give the Crank-Nicholson approximation [Burden, 1989], where we use $\lambda = D\frac{dt}{(dx)^2}$:

$$U(x+dx,t+dt)\left(\frac{-\lambda}{2}\right)+U(x,t+dt)(1+\lambda)+U(x-dx,t+dt)\left(\frac{-\lambda}{2}\right)=$$
$$U(x+dx,t)\left(\frac{\lambda}{2}\right)+U(x,t)(1-\lambda)+U(x-dx,t)\left(\frac{\lambda}{2}\right). \tag{3.1.4}$$

Equation (3.1.4) can be cast in matrix form:

$$\begin{pmatrix} (1+\lambda) & -\lambda/2 & & \\ -\lambda/2 & (1+\lambda) & -\lambda/2 & \\ 0 & -\lambda/2 & (1+\lambda) & -\lambda/2 \\ & & & \cdots \\ & & & \end{pmatrix}\begin{pmatrix} U[x_0,t_1] \\ U[x_1,t_1] \\ U[x_2,t_1] \\ \cdots \\ \end{pmatrix}=\begin{pmatrix} (1-\lambda) & \lambda/2 & & \\ \lambda/2 & (1-\lambda) & \lambda/2 & \\ & \lambda/2 & (1-\lambda) & \lambda/2 \\ & & & \cdots \\ & & & \end{pmatrix}\begin{pmatrix} U[x_0,t_0] \\ U[x_1,t_0] \\ U[x_2,t_0] \\ \cdots \\ \end{pmatrix} \tag{3.1.5}$$

which relates the full spatial distribution at any time step t_{i+1} to that at t_i. We will discuss the boundary conditions in the next section.

3.2 Quasiparticle Inelastic Scattering/Trapping

After the quasiparticles have diffused through the absorber, they reach the interface between the absorber and the aluminum trap. The inelastic scattering of quasiparticles with phonon emission in the aluminum causes them to be confined to the junction region. Here

they are "trapped", and tunnel through the barrier instead of diffusing back into the absorber. The initial scattering in aluminum is thus referred to as quasiparticle trapping. The scattering rate determines the trapping rate, assuming that there is good metallic contact between the absorber and the trap. In addition, the inelastic scattering rate determines the energy distribution of the quasiparticles in the junction before they tunnel. Later in chapter 4 we will see how this energy dependence has a large effect on the signal.

The inelastic scattering time has been calculated for quasiparticles in near-equilibrium by Kaplan, et al. [Kaplan,1976]. We will refer often to this work. The scattering rate, $1/\tau_s$, for a quasiparticle at energy E_i to emit a phonon of energy $\Omega_{min} \leq \Omega \leq \Omega_{max}$ is given by:

$$\frac{1}{\tau_s} = \frac{1}{\tau_0}\left(\frac{1}{k_B T_c}\right)^3 \int_{\Omega min}^{\Omega max} \Omega^2 N(E_i - \Omega)\left[1 - \frac{\Delta^2}{E_i(E_i - \Delta)}\right] d\Omega. \tag{3.2.1}$$

Here k_B is Boltzman's constant, T_c is the critical temperature of the film, $N(E_i - \Omega)$ is the density of final electron states, and τ_0 is a material dependent constant. The value τ_0 is the electron-phonon interaction parameter, as the integral term gives just the energy dependence independent of the material. The integral in equation (3.2.1) can be solved analytically. Using the variable changes $x = \frac{E_i - \Omega}{\Delta}$ and $y = \sqrt{x^2 - 1}$ we find:

$$\frac{1}{\tau_s} = \frac{1}{\tau_0}\left(\frac{\Delta}{k_B T_c}\right)^3 \cdot$$

$$\left[\frac{y^3}{3} + (3 + E_{i\Delta})y - \left(E_{i\Delta} + \frac{1}{2E_{i\Delta}}\right)y\sqrt{y^2+1} - \left(2E_{i\Delta} + \frac{1}{2E_{i\Delta}}\right)\ln\left(y + \sqrt{y^2+1}\right)\right]_{y(\Omega_{min})}^{y(\Omega_{max})}. \tag{3.2.2}$$

Here we use $E_{i\Delta} = E_i/\Delta$. In our model it is useful to define the rate $1/\tau_s[E_i,E_j]$ to scatter from an energy E_i to an energy E_j, where E_i and E_j are located at the center of energy intervals of size 2δ. Equation 3.2.2 is used with $\Omega_{min} = [E_i - (E_j + \delta)]$ and $\Omega_{max} = [E_i - (E_j - \delta)]$. We use this in section 3.5. This idea is shown in Fig. 3.2.1.

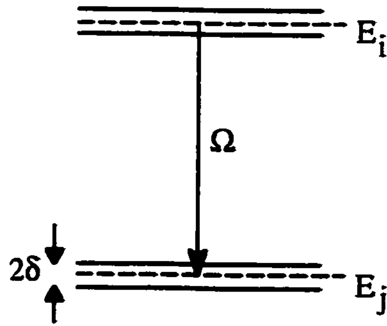

Fig. 3.2.1: Schematic of phonon scattering from E_i to E_j.

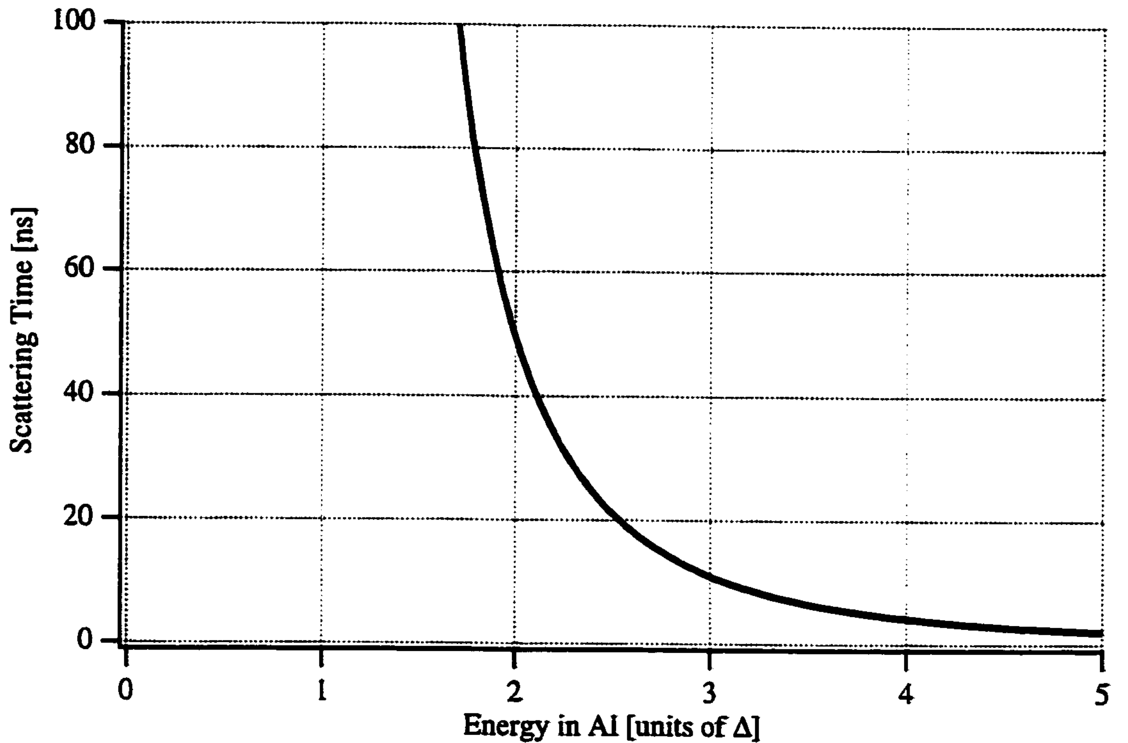

Fig. 3.2.2: Scattering time in aluminum. The energies are in units of the aluminum gap.

If we insert $\Omega_{min} = 0$ and $\Omega_{max} = (E_i - \Delta)$, then equation 3.2.2 gives the *total* scattering rate, the time for a quasiparticle at E_i to emit a phonon of any size allowed by energy conservation. We plot this time in Fig. 3.2.2. If $E_i = \Delta_{Ta} \approx 4\Delta_{Al}$, then the total scattering time is the trapping time τ_{trap}. This value is about 6 ns.

The trapping of quasiparticles into the junction is modeled by a boundary condition at the absorber-trap interface. Let us consider the distribution of quasiparticles n(x) *above the gap of tantalum.* Assume the absorber-trap interface is located at x = 0, with the

absorber to the left (negative x) and the trap to the right (positive x). This distribution decays exponentially into the aluminum trap, because in the trap quasiparticles are "lost", since they scatter below Δ_{Ta}. The time for them to scatter is τ_{trap}. The decay length, l_{trap}, is simply given by $l_{trap} = \sqrt{(D_{Al}\tau_{trap})}$. To derive the boundary condition we require that the diffusion current be continuous across the absorber-trap interface:

$$D_{Ta}\left.\frac{\partial n}{\partial x}\right|_{x=0^-} = D_{Al}\left.\frac{\partial n}{\partial x}\right|_{x=0^+}. \tag{3.2.3}$$

Here D_{Ta} and D_{Al} are the diffusion constants in tantalum and aluminum, respectively. Since the distribution in the aluminum trap is exponential, we can also write,

$$\left.\frac{\partial n}{\partial x}\right|_{x=0^+} = \frac{\partial}{\partial x}\left[n\left(x=0^+\right)e^{-x/l_{trap}}\right]_{x=0^+} = -\frac{n\left(x=0^+\right)}{l_{trap}}. \tag{3.2.4}$$

Combining equations (3.2.3) and (3.2.4) we find the boundary condition:

$$\left.\frac{\partial n}{\partial x}\right|_{x=0^-} = -\frac{n(x=0^-)}{l^*_{trap}}, \tag{3.2.5}$$

with $l^*_{trap} = \sqrt{D_{Ta}\left(\frac{D_{Ta}}{D_{Al}}\right)\tau_{trap}}$. Here we have assumed that $n(x = 0^+) = n(x = 0^-)$, i.e. that the function n is continuous. This equation can be inserted into the Crank-Nicholson algorithm, equation (3.1.5). We approximate equation (3.2.5) with a difference equation at the endpoint x_0 (and also x_{max}) for all times t:

$$\frac{U[x_1,t]-U[x_0,t]}{dx} = -\frac{U[x_0,t]}{l^*_{trap}}. \tag{3.2.6}$$

The boundary condition allows us to treat the effects of the trapping without explicitly keeping track of the spatial distribution in the junction. Note that the boundary condition is only valid if the value l_{trap} is smaller than the actual size of the trap, or the distribution cannot be approximated as exponential. This is true in our devices. The current that flows across the absorber-trap interface, I_{int}, with the boundary condition from (3.2.5) is the current that is trapped. I_{int} is given by either side of equation (3.2.3). We will return to this in section 3.5.

3.3 Quasiparticle Tunneling

Tunneling is the process by which quasiparticles are detected as a charge in our devices, and as such a good grasp of quasiparticle tunneling is essential to understand the

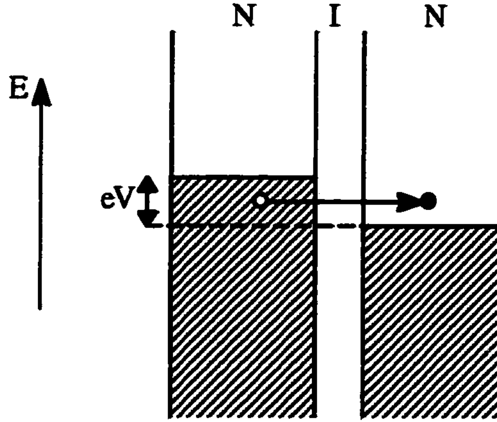

Fig. 3.3.1: Tunneling diagram for an NIN junction. The shaded regions represent filled states.

detector operation. Excellent treatments of superconductor tunneling are given in Van Duzer [van Duzer, 1981], Tinkham [Tinkham, 1996] or Gray [Gray, 1980]. In this section we will be explicitly interested in calculating the tunnel rate, $1/\tau_{tun}$, and in understanding how the I-V curve for a superconducting tunnel junction comes about.

We start by considering a normal metal tunnel junction (Normal-Insulator-Normal or NIN junction). The energy diagram at T = 0 is shown in Fig. 3.3.1. A filled Fermi sea exists on both sides of the barrier with the two Fermi energies separated by the energy eV of the bias. Tunneling of electrons occurs whenever filled states on one side face empty states on the other side. The total tunneling current can be calculated by Fermi's Golden Rule [Van Duzer, 1981]. At sufficiently low temperatures and voltages the tunneling current, I_{nn}, is ohmic and is given by

$$I_{nn} = \frac{V}{R_{nn}}. \tag{3.3.1}$$

Here R_{nn} is the resistance of the tunnel barrier, given by

$$R_{nn} = \left[\frac{2\pi e^2 A_{Jct}}{\hbar} |T|^2 N_l(E_f) N_r(E_f) \right]^{-1}, \tag{3.3.2}$$

where A_{Jct} is the area of the tunnel barrier, $|T|^2$ is the matrix element for transmission across the barrier, $N_{l/r}(E_f)$ is the density of states on the left/right hand side at the Fermi energy, e is the charge of the electron and $\hbar$ is Plank's constant.

The tunneling time τ_{tun} for an arbitrary tunneling current I is defined through the relation

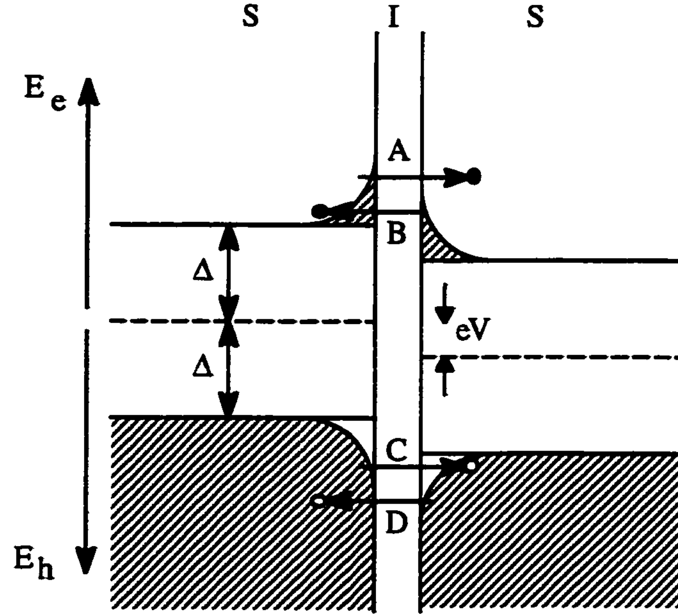

Fig. 3.3.2: Tunneling diagram for an SIS junction, in the Semiconductor representation. The closed circles represent electrons tunneling, the open circles represent holes tunneling.

$$I = \frac{eN}{\tau_{tun}}, \tag{3.3.3}$$

where N is simply the number of electrons (or quasiparticles) that can tunnel. In the case of two normal metals as in Fig. 3.3.1, the only electrons that can tunnel are the ones within eV of the Fermi energy on the left side. Thus $N = N_l(E_f) \cdot eV \cdot V_{elec}$, where V_{elec} is the volume of the electrode on the left. We can then use equations (3.3.1) and (3.3.3) to obtain an expression for τ_{tun} for an NIN junction:

$$\tau_{tun,NIN} = e^2 \cdot N_l(E_f) \cdot R_{nn} \cdot V_{elec}. \tag{3.3.4}$$

Note that although the density of states on the left side, $N_l(E_f)$, appears explicitly in equation (3.3.4), in reality the tunnel time is proportional $N_r(E_f)^{-1}$, due to the dependence of R_{nn} on $N_l(E_f)$ and $N_r(E_f)$.

If we now consider both metals to be superconducting, two important modifications occur. The first is simply that the density of states is modified to be the density of states for quasiparticles, in the usual fashion. The second modification, however, is more subtle. We plot the energy band diagram in Fig. 3.3.2 for a superconducting tunnel junction using the so-called "semiconductor representation". Recall that in a superconductor, quasiparticles are split into electron-like ($k > k_f$) and hole-like ($k < k_f$) quasiparticles. In using the semiconductor representation, we remove the mixed character of the

quasiparticles and assumes that all electron-like quasiparticles have a negative charge and all hole-like quasiparticles have a positive charge. This gives the correct tunneling current because of the symmetry of the BCS ground state around k_f. The energies for electrons (E_e) are plotted in the positive direction while the energies for holes (E_h) are plotted in the negative direction. The lowest energy excitations for both electrons and holes are at an energy Δ, the energy gap of the superconductor. If the junction is at $T = 0$, there are no excitations; all electron states are empty and all hole states are filled. If instead the junction is at a finite temperature T_{bath}, there will be excited electrons and holes spread over an energy $k_B T_{bath}$ in their respective bands.

We demonstrate the possible tunneling processes in the diagram, labeling the processes A through D. If the junction is biased at a voltage $V < k_B T_{bath}/e$, then both electrons and holes can tunnel from either side of the barrier and all four tunnel processes are possible. If, however, the junction is biased at a voltage $V >> k_B T_{bath}/e$, then only electrons on the left side and holes on the right side can tunnel (A and D). This is because holes on the left and electrons on the right face unavailable states on the other side of the barrier. If we want to consider N in equation (3.3.3) to be the *total* number of quasiparticles on either side of the barrier, then the tunnel time *per quasiparticle* is twice as long as we have derived previously. Thus the tunnel time in equation (3.3.4) must be multiplied by a factor of two. Note that even though only half the quasiparticles can tunnel at a given time, all the quasiparticles still eventually tunnel, as the ones which cannot tunnel will eventually branch mix [Kaplan, 1976], changing from an electron to a hole or vice-versa.

We can now re-write the tunnel time for an SIS junction, inserting the modification in the density of states and the factor of two for electrons and holes:

$$\tau_{tun,SIS} = 2e^2 N_I(E_f) R_{nn} \cdot V_{elec} \cdot \frac{\sqrt{(\Delta + E_r)^2 - \Delta^2}}{\Delta + E_r}. \tag{3.3.5}$$

This is the time for a quasiparticle to tunnel from the left hand side to the right hand side, ending at an energy E_r above Δ; V_{elec} here is the volume on the left. We modify the density of states for the energy E_r on the right hand side, namely the density of states into which the quasiparticle tunnels. The factor of two enters, again, because only half the quasiparticles on the left hand side can tunnel.

Equation (3.3.5) is usually written with $E_r = eV$ [de Korte, 1992]. This is then tunnel time for a quasiparticle right at the gap edge on the left hand side. By using this equation with $E_r = eV$ to calculate the current, one assumes that *all* quasiparticles have

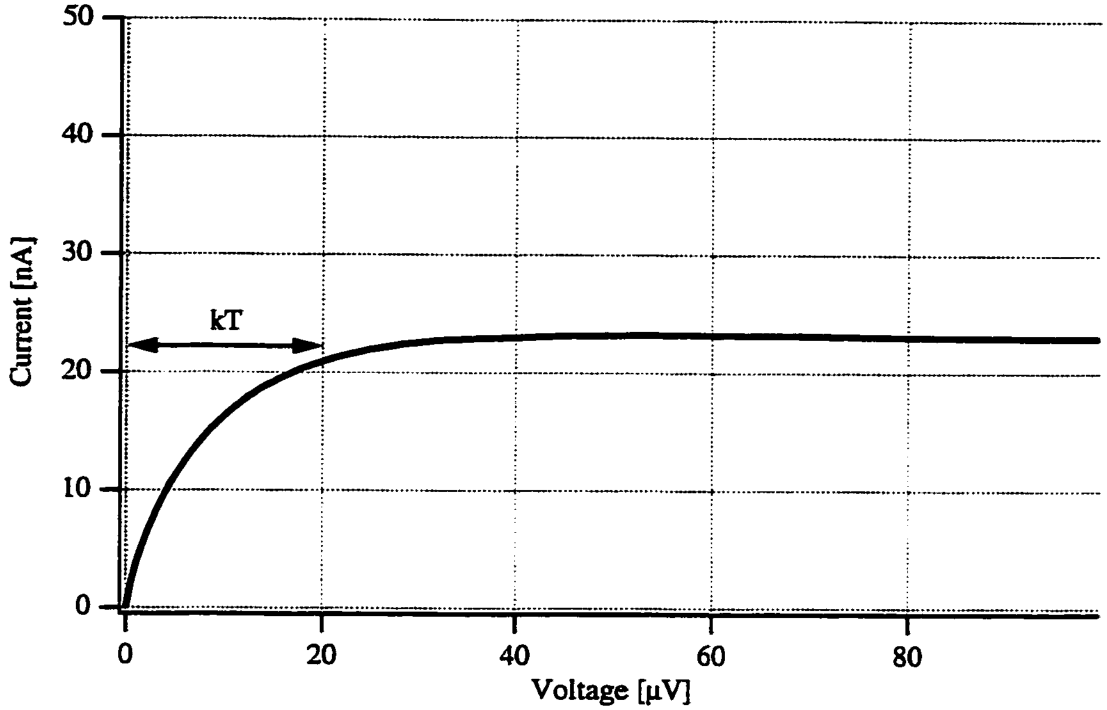

Fig 3.3.3: Subgap I-V curve for an SIS junction. The current rises below voltages less than k_BT/e, and is constant far above k_BT/e.

scattered to the gap edge before they tunnel. We do not wish to make this assumption, so that is why we have written (3.3.5) in a more general form. Note the tunnel time is a strong function of energy near the gap ($E_r \rightarrow 0$), but approaches a constant value of $2\tau_{tun,NIN}$ at high energies. If one is tunneling into a range of energies 2δ about E_r, we use the average value of the tunnel rate over that energy range:

$$1/\tau_{tun}[E_r] = \frac{1}{2\delta}\int_{E_r-\delta}^{E_r+\delta} dE \left[2e^2 N_r(E_f) R_{nn} \cdot V_{elec} \cdot \frac{\sqrt{(\Delta+E)^2-\Delta^2}}{\Delta+E} \right]^{-1} . \qquad (3.3.6)$$

We will use expression (3.3.6) when we describe the full current pulse simulation in section 3.5. Note that we have dropped the 'SIS' part of the subscript, as τ_{tun} will now indicate the tunnel time in the superconducting case since we will no longer be dealing with normal metals.

Having already introduced the semiconductor representation, it is an easy task to determine the I-V curve in the subgap region. Let us consider only the excitations on the left hand side (the same argument can be applied to the right hand side, with electrons and holes reversed). At low bias voltages, ($V < k_BT_{bath}/e$), both electrons and holes can tunnel. Since electrons and holes carry opposite charge, their currents cancel each other, and we

have little net electron current. As we raise the voltage, some of the holes are prevented from tunneling because they face forbidden states. Thus, we get an increased electron current. As we raise the voltage further, more and more of the holes are prevented from tunneling, and the electron current continues to increase. Finally, when we reach $V >> k_B T_{bath}/e$, none of the holes can tunnel and the electron current remains constant. Thus the I-V curve has a low bias region ($V < k_B T_{bath}/e$) where the current is increasing, and a high bias region ($V >> k_B T_{bath}/e$), where the current is constant. This is plotted in Fig. 3.3.3. We will see later in chapter 4 that T_{bath} will be replaced by a 'warmer' distribution characterized by T_{eff} during an x-ray pulse, but the same arguments regarding the structure of the I-V curve will still hold.

Before we leave this section, it is necessary to relate the semiconductor representation which we have used so far to the so called 'excitation representation', which is used most often in this field. This is shown in Fig. 3.3.4. In this representation the electrons and holes are not distinguished. However, we now show the pairs explicitly. The tunnel processes A-D that were shown in Fig. 3.3.2 are indicated. The tunneling processes which correspond to electrons, A and B, look essentially the same. However, the hole processes C and D look quite different. One has to remember that the semiconductor representation in Fig. 3.3.2 corresponds to excitations with respect to the *BCS ground state*, not the filled Fermi sea of a normal metal. Consider a hole excitation on the left side tunneling to the right (process C). Initially, the hole on the left corresponds to an unoccupied pair state. In order to transfer that excitation to the right side (i.e. for it to "tunnel"), one must reform a pair on the left and break up a pair on the right. This fills the hole on the left and creates one on the right. This is illustrated explicitly in the excitation representation. The excitation diagram has the advantage of showing the charge transfer explicitly, with the disadvantage of not showing the symmetry of the I-V curve. The hole tunneling from the right hand side (process D), which transfers an electron from left to right, is often referred to as backtunneling. This gives an increase in the overall signal from an x-ray. In accordance with the rest of the field, we will use the excitation representation in the remainder of work.

One additional piece of notation: when we refer to a hole tunneling from the left hand side and an electron tunneling from the right hand side, we call it a "reverse process", since in both cases a charge (electron) is transferred from right to left, against the bias. Thus B and C are reverse processes. When a reverse process "cancels" the current from a normal (forward) process, we call that cancellation. In section 5.3 we will calculate the shot noise that results from the canceled currents.

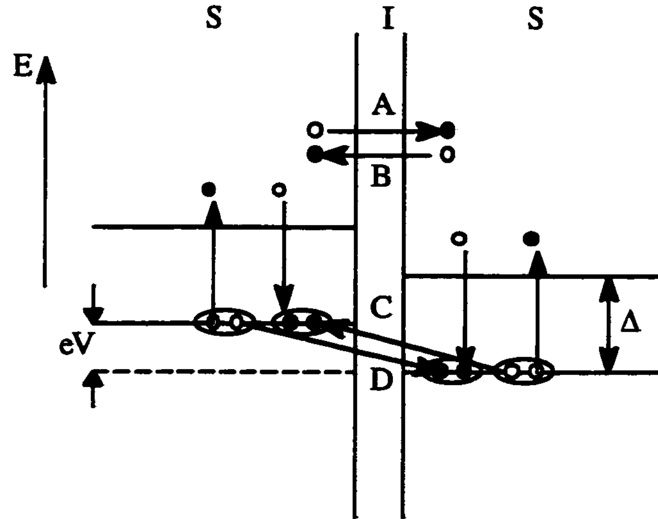

Fig. 3.3.4: Tunneling diagram for an SIS junction, using the excitation representation.

3.4 Quasiparticle Recombination

The recombination of quasiparticles back into Cooper pairs is an extremely important effect in our detectors. Quasiparticles which recombine rather than tunnel reduce the overall electronic signal while increasing the noise, as there are statistical fluctuations in the number of quasiparticles lost from one photon to the next. The theoretical recombination lifetimes have been calculated by Kaplan, et al. [Kaplan, 1976] for superconductors in near equilibrium, i.e. for small numbers of excess quasiparticles. Typical treatments of recombination for the non-equilibrium case also use Kaplan, et al.'s numbers, although one must be wary that the theory is not strictly valid in these limits. Our experiments find recombination times consistent with these predictions in aluminum, but far from these predictions in tantalum. Here we will review the formalism and show how we have modeled the loss of quasiparticles to recombination in the absorber and in the junctions.

The near-equilibrium recombination time for quasiparticles in the low temperature limit, $1/\tau_{rec,eq}$, is given by [Kaplan, 1976]:

$$\frac{1}{\tau_{rec,eq}} = \frac{1}{\tau_0}\pi^{1/2}\left(\frac{2\Delta}{k_B T_c}\right)^{5/2}\left(\frac{T}{T_c}\right)^{1/2} e^{-\Delta/k_B T}. \qquad (3.4.1)$$

Values for this recombination time at 0.2 K are ≈ 400 μs in aluminum and > 1s in tantalum. For the non-equilibrium case we define a general τ_{rec} which is determined by

$$\left.\frac{\partial N}{\partial t}\right|_{rec} = \frac{N^2 R}{V} = \frac{N}{\tau_{rec}}. \tag{3.4.2}$$

Here R is defined as the recombination rate per unit density of quasiparticles. The factor of N^2 occurs because there are $N(N-1)/2 \approx N^2/2$ ways to form pairs from N quasiparticles; the factor of two is lost because each recombination event eliminates two quasiparticles. In general N is equal to the number of excess quasiparticles, N_x, plus the number of thermal quasiparticles, N_{th}. The number of thermal quasiparticles is given by $n_{th}V$, where V is the volume of the superconductor and n_{th} is the thermal density of quasiparticles:

$$n_{th} = N(E_f)\sqrt{2\pi\Delta k_B T}e^{-\Delta/k_B T}. \tag{3.4.3}$$

Using (3.4.1) - (3.4.3) in the limit of no excess quasiparticles ($N_x \to 0$), one can solve for the recombination rate R:

$$R = \left(\frac{2\Delta}{k_B T_c}\right)\frac{1}{2N(E_f)\Delta\tau_0}. \tag{3.4.4}$$

In the case where N_x is significant we can then solve for τ_{rec} using (3.4.2):

$$\frac{N}{\tau_{rec}} = \frac{R}{V}\left(N_x^2 + 2N_x n_{th} V\right), \tag{3.4.5}$$

where the term independent of excess quasiparticles is lost because it is exactly canceled by thermal generation. The first term is usually referred to as the "self-recombination" rate, as it depends only on the number of excess quasiparticles, while the second term is referred to as the thermal recombination rate, as it depends on the thermal background of quasiparticles. Note the factor of 2 in the thermal term. Physically this is a simple permutation effect, as the first quasiparticle can be thermal and the second one excess, or vice versa.

Equation (3.4.5) will be used as the expression for recombination in the junction electrodes, as it is fairly straightforward to incorporate both terms into our simulation. In the absorber, however, the introduction of an N^2 term into the diffusion equation makes it a non-linear differential equation and precludes the use of the numerical method described in section 3.1. We therefore ignore self-recombination in the absorber. This appears to be valid, since experimentally we see negligible non-linearity in our energy response, which would not be the case if we had significant self-recombination. Future modeling should, however, seek a new diffusion algorithm to incorporate the self-recombination. We do nonetheless introduce a constant loss term ($1/\tau_{loss}$) into the diffusion equation to account for recombination in the absorber. This is an "adjustable" parameter in our model, since

the theoretical value for τ_{loss} (the thermal term in equation (3.4.5)) would be negligible for tantalum. It is incorporated into the Crank-Nicholson algorithm by simply subtracting a term $1/\tau_{loss}$ from the diagonal elements in the matrix in equation (3.1.5). Physical interpretations of τ_{loss} include trapping into regions of lower gap due to flux penetration, at the edges of the film, or at the Nb contact.

3.5 Current Pulse Simulation

The various processes that we have discussed thus far all contribute to the size and shape of the current pulse. The challenge in interpreting the observed current pulses from our detector lies in separating out the individual effects, as all the processes described above have comparable time scales. To aid in our understanding, we have incorporated all of the modeling into a single algorithm which produces a theoretical current pulse. These pulses can then be compared directly with experiment. In this section we will discuss the development of the current pulse model.

3.5.1 Simulation Algorithm

As explained previously, we keep track of the spatial distribution of quasiparticles in the absorber and the energy distribution of quasiparticles in the trap. The spatial distribution in the absorber is represented by a one-dimensional vector U whose values $U[x_i]$ gives the number of quasiparticles about the spatial grid point x_i. Typically we use 200 grid points for our 200 μm absorber, so the spacing is $dx = 1$ μm. Similarly, the energy distribution of quasiparticles in the trap and counterelectrode are represented by vectors $N_{trap}[E_i]$ and $N_{ce}[E_i]$ whose values give the number of quasiparticles about the energy E_i. We use 52 energy intervals for the 520 μeV between Δ_{Al} and Δ_{Ta}, giving a energy spacing of $2\delta = 10$ μeV per energy interval. The spatial distribution evolves via the diffusion equation with the trapping boundary condition, as described in sections 3.1 and 3.2. The energy distribution in the trap and counterelectrodes evolve through rate equations for tunneling, scattering and loss. We will describe these below. At each time step we update the distributions U, N_{trap} and N_{ce} and then calculate the total current. The full current pulse is generated and then its size and shape are computed (total charge, peak current, risetime, falltime, delay time). These values can then be compared with the data.

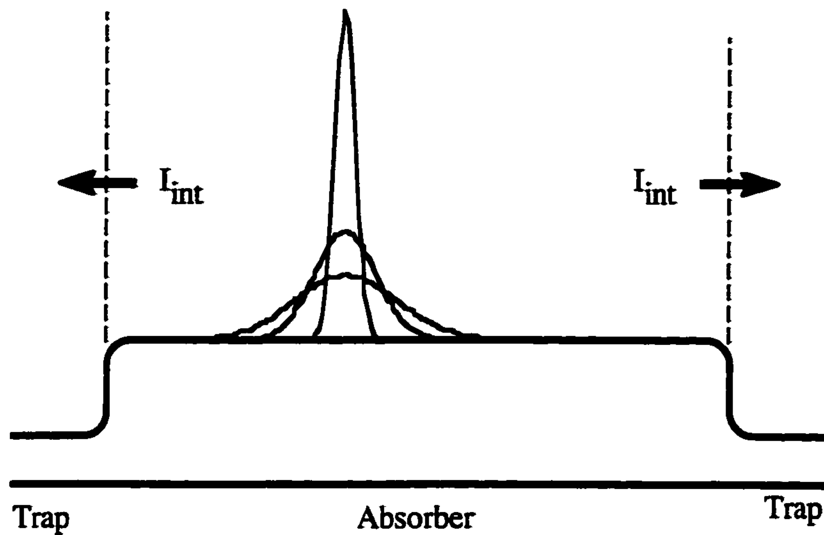

Fig. 3.5.1: Schematic of the current pulse simulation in the absorber. The diffusion equation is iterated to compute the interface current, I_{int}

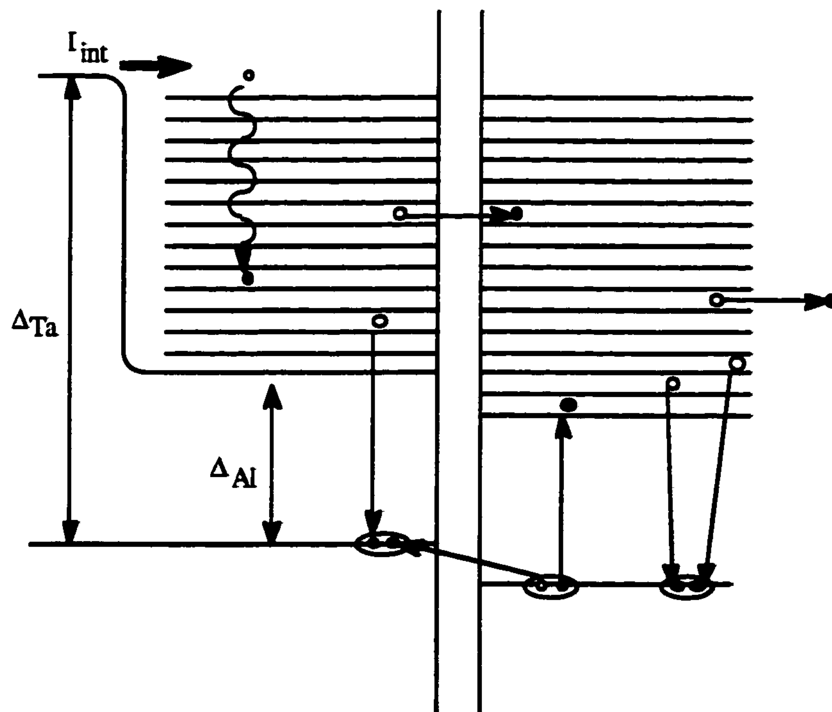

Fig. 3.5.2: Schematic of the current pulse simulation in the junction. The junction is divided into energy intervals, in which the time evolution of the quasiparticle density is calculated. The interface current I_{int} is the output from the absorber part of the simulation.

In Fig. 3.5.1 and 3.5.2 we illustrate schematically the two parts of the simulation. In the absorber part (Fig. 3.5.1), we iterate the diffusion equation with the trapping

boundary condition to calculate the interface current, I_{int}, which is the current that flows across the absorber-trap interface into either trap. The interface current enters the topmost energy interval in the trap, where the quasiparticles can undergo several processes: inelastic scattering to lower energy, tunneling to and from the counterelectrode, recombination into Cooper pairs, and outdiffusion from the counterelectrode. The combination of these processes form the junction part of the simulation. These are illustrated in Fig. 3.5.2. The interface current is the "connection" between the two parts of the simulation, namely the output of the absorber part and the input to the junction part.

The initial condition for the simulation is a gaussian of quasiparticles in the absorber at a location x_0. The total charge in the gaussian is equal to Q_0, one of the input parameters. The width of the delta function is typically a few microns, set to match the expected width of the hotspot region. Following the initial condition each time step proceeds as follows:

(1) Iterate the diffusion equation to obtain a new distribution U in the absorber.
(2) Calculate the interface current flowing into the trap.
(3) Inject the interface current into the uppermost energy interval in the trap.
(4) Iterate the junction rate equations to obtain new energy distributions N_{trap} and N_{ce}.
(5) Calculate the total tunneling current from the distributions N_{trap} and N_{ce}.

The simulation continues until all quasiparticles are lost via recombination or outdiffusion. We have described already steps (1) and (2) in the sections on diffusion and trapping. We will now describe steps (3) – (5).

3.5.2 Junction Rate Equations

Fig. 3.5.2 illustrates the various quasiparticle processes in the junction electrodes. We are interested in the total time rate of change dN/dt of quasiparticles in the energy interval E_i. From Fig. 3.5.2, we consider the change due to the interface current, inelastic scattering, tunneling, recombination, and outdiffusion:

$$\frac{dN[E_i]}{dt} = \left.\frac{\partial N[E_i]}{\partial t}\right|_{int} + \left.\frac{\partial N[E_i]}{\partial t}\right|_{scat} + \left.\frac{\partial N[E_i]}{\partial t}\right|_{tun} + \left.\frac{\partial N[E_i]}{\partial t}\right|_{rec} + \left.\frac{\partial N[E_i]}{\partial t}\right|_{out} . \qquad (3.5.1)$$

Here "N" can be considered to be N_{trap} or N_{ce}, although the individual terms are not the same for both. The first term, the change due to the interface current, is obvious:

$$\left.\frac{\partial N_{trap}[E_M]}{\partial t}\right|_{int} = \frac{I_{int}}{e} \qquad (3.5.2)$$

This term only occurs on the trap side for the topmost energy $E_M = \Delta_{Ta}$.

The second term in equation (3.5.1), the change due to inelastic scattering, is given by the number that scatter into energy E_i from higher energies minus the number that scatter out of energy E_i into lower energies:

$$\left.\frac{\partial N[E_i]}{\partial t}\right|_{scat} = \sum_{j=i+1}^{M} \frac{N[E_j]}{\tau_s[E_j,E_i]} - \sum_{k=0}^{i-1} \frac{N[E_i]}{\tau_s[E_i,E_k]}, \tag{3.5.3}$$

where $\tau_s\,[E_i,E_j]$ is the scattering time from E_i to E_j defined in section 3.2. This term is the same for both the trap and the counterelectrode.

The third term, the change due to tunneling, is given by the number of quasiparticles that tunnel into E_i minus the number that tunnel out of E_i. Recalling section 3.3, there are two processes for entering and two for leaving that conserve energy:

$$\left.\frac{\partial N_{trap}[E_i]}{\partial t}\right|_{tun} = -\frac{\partial N_{trap}[E_i]}{\tau_{tun,tr}[E_i + eV]} - \frac{\partial N_{trap}[E_i]}{\tau_{tun,tr}[E_i - eV]} + \frac{\partial N_{ce}[E_i + eV]}{\tau_{tun,ce}[E_i]} + \frac{\partial N_{ce}[E_i - eV]}{\tau_{tun,ce}[E_i]}. \tag{3.5.4}$$

Here $1/\tau_{tun}\,[E_i]$ is the tunneling rate into energy E_i. The terms in equation (3.5.4) correspond to tunnel processes A, C, B, and D, respectively, that were described in section 3.3. Processes A and C remove a quasiparticle from energy interval E_i while B and D put a quasiparticle into E_i. Note that the tunnel rates for processes B and C are zero if $E_i < (\Delta + eV)$. We have written equation (3.5.4) for the trap, but a similar relationship exists for the counterelectrode.

The fourth term in equation (3.5.1) is the change due to recombination. This was discussed in section 3.4:

$$\left.\frac{\partial N[E_i]}{\partial t}\right|_{rec} = \frac{R}{V}\left[\left(\sum_{j=1}^{M} N[E_j]\right) + 2n_{th}V\right] N[E_i], \tag{3.5.5}$$

where the first term is the self-recombination term and the second is the thermal recombination term. This equation is identical for the trap and the counterelectrode.

Finally, the last term in equation (3.5.1) is the change due to outdiffusion. This is simply a constant loss term $1/\tau_{out}$ which occurs only in the counterelectrode:

$$\left.\frac{\partial N_{ce}[E_i]}{\partial t}\right|_{out} = \frac{N_{ce}[E_i]}{\tau_{out}}. \tag{3.5.6}$$

We have now defined all the terms in equation (3.5.1). There is a rate equation for the M energy intervals in the trap and counter-electrode. As mentioned previously, typically M = 52 in our simulation. The resulting system of 104 coupled differential equations are iterated with the Modified Euler method [Burden, 1989] because only full time steps are used. The usual Runga-Kutta methods were not chosen because the interface current cannot be computed at half time steps [Burden, 1989].

We can also use the rate equations to look at just the energy distribution due to inelastic scattering alone, to isolate the effect of quasiparticle cooling. We do this by setting all other terms on the right hand side of equation (3.5.1) equal to zero except for the second one, the change due to scattering. We then iterate the rate equations only, without the simulation in the absorber. We use this to calculate the energy distribution in Ta after an x-ray is absorbed to check for a possible reduction in diffusion constant (section 4.1) and also to calculate the energy distribution in Al while tunneling (section 4.2). The materials parameters are chosen appropriately for Al or Ta.

3.5.3 Current Equation

Having solved for the distributions N_{trap} and N_{ce} as a function of time, it is a fairly simple matter to calculate the current. In general the current from a given energy interval is simply the number divided by the tunnel time, via equation (3.3.3). We simply have to sum over all energy intervals and over the different processes (A - D in section 3.3), keeping in mind that half of the processes contribute a positive current and half contribute a negative current. The total tunneling current I_{tun} is given by:

$$\frac{I_{tun}}{e} = \sum_i \left[\frac{N_{trap}[E_i]}{\tau_{tun,tr}[E_i + eV]} - \frac{N_{trap}[E_i]}{\tau_{tun,tr}[E_i - eV]} + \frac{N_{ce}[E_i]}{\tau_{tun,ce}[E_i + eV]} - \frac{N_{ce}[E_i]}{\tau_{tun,ce}[E_i - eV]} \right] \tag{3.5.7}$$

Before finishing, we list the specifics for the simulation:

• <u>Experimental constants</u>: Absorber length (L_{abs}), bath temperature (T), trap and counterelectrode volume (V_{trap} and V_{ce}) are all set by the device geometry and experiment.

• <u>Physical constants</u>: Electron-phonon scattering time (τ_0), energy gap in aluminum junction (Δ), density of states at Fermi Surface in aluminum ($N(E_f)$), normal metal tunnel time (τ_{tun}) are all considered constants. The tunnel time and energy gap come from measurements of

the resistivity and the DC I-V curve respectively; $N(E_f)$ and τ_0 come from theory [Kaplan, 1976]. We do vary the value of τ_0 some to compare with theory, which is discussed in section 4.3.

• Adjustable parameters: Trapping time (τ_{trap}), tantalum diffusion constant (D), absorber loss time (τ_{loss}), initial charge (Q_0), outdiffusion time (τ_{out}) are fit with the experiment; see section 4.1.

• Other inputs: Bias voltage (V_{dc}), absorption location (x_0).

• Numerical methodology: Diffusion equation approximated by Crank-Nicholson algorithm, junction rate equations solved by Modified Euler method. Typical spatial grid of $dx = 1\ \mu m$ and energy spacing $2\delta = 10\ \mu eV$. Typical time steps of 10 ns.

Chapter 4: Detector Physics

The double junction geometry that we employ in our detectors provides a good system to study non-equilibrium quasiparticle dynamics. The shapes and time scales of the current pulses provide information about quasiparticle diffusion, tunneling, recombination, and inelastic scattering. Work in this area has been published already by our group [Segall, 1997; Friedrich, 1997b; Friedrich, 1997c] and continues to be a major focus of our research efforts. In this chapter we will discuss experiments related to the detector physics. We will use the model for the pulse shapes developed in chapter 3 to extract various physical parameters related to the device operation. We will be particularly concerned with how certain quasiparticle processes affect the signal charge, which has implications for noise and device performance. Finally, we will extend the analysis to newer devices and explore some different geometries and detector parameters. A full discussion of the detector performance will follow in chapter 5.

4.1 Pulse Shapes

The absorption of an x-ray in our detector leads to the creation of millions of excited quasiparticles. These quasiparticles then diffuse through the absorber, are trapped in either junction, tunnel through the barrier and finally diffuse away into the leads. Each time a given quasiparticle tunnels, it is registered as a charge by the amplifier. The full current pulse is then determined by when and how often each quasiparticle tunnels. In this section we will discuss how the various quasiparticle processes – diffusion, scattering, tunneling, recombination – affect the size and shape of the current pulse. We will emphasize the use of the model developed in Chapter 3.

4.1.1 Pulse Shape Fitting

A typical pair of current pulses is shown in Fig. 4.1.1. These are the two pulses from a *single* x-ray event, one that was closer to one of the junctions (junction 1) than the other. The pulses have a finite rise time followed by a longer fall time. This overall behavior is easily understood. Because the junction volume is small, we assume that *all* the quasiparticles that are in the junction at a given time can tunnel; thus the total tunneling current is simply proportional to the *number* of quasiparticles that are in the junction. When there are more quasiparticles entering the junction than leaving, the current (number) is increasing; when there are more quasiparticles leaving than entering, the current is decreasing. The rise of the pulse (time during which it is increasing) is thus associated

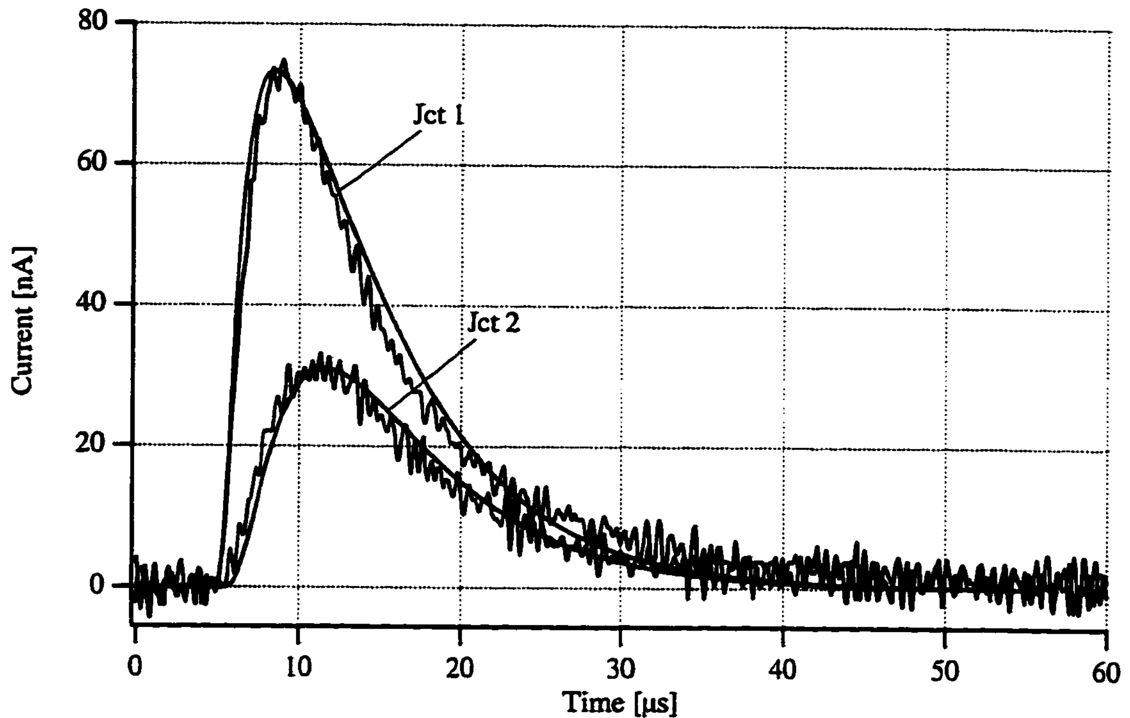

Fig. 4.1.1: Two current pulses from a single x-ray absorption event, with fits from the model. (7/9/97)

with how quasiparticles enter the junction: diffusion through the absorber and scattering into the trap region. Similarly, the fall of the pulse is associated with how quasiparticles leave the junction: tunneling through the barrier and diffusing away into the leads.

Shown also in Fig. 4.1.1 are the fits from the model, and one can see we find very good agreement with the data. The fits have certain values chosen for the model's input parameters. The input parameters are D, the diffusion constant in the absorber; τ_{trap}, the trapping time; τ_{loss}, the loss time in the absorber; Q_0, the initial quasiparticle charge; and τ_{out}, the outdiffusion time away from the junction, from the counterelectrode into the leads. The parameters are constrained by measurements of the current pulses. The number of parameters in the model is equal to the number of measurements, thus leaving no adjustable parameters in the fit. Below we list each measurement, and the key parameters that affect it.

(1) Charge Division (Q_1^{edge}/Q_2^{edge}): The ratio of the integrated charge in each junction for absorption events near the edge of the absorber (Q_1^{edge}/Q_2^{edge}) is a measurement of the charge division and the strength of the trapping. Consider an event very close to junction 1. If the trapping is strong, the quasiparticles will be trapped in junction 1 almost

immediately upon being generated and very few will diffuse to junction 2. Thus the value Q_1^{edge}/Q_2^{edge} will be very large (≈ 100 or greater). For weaker trapping, some charge will not be trapped and more will diffuse to junction 2; the ratio Q_1^{edge}/Q_2^{edge} will then be less. The charge division is only related to the strength of the trapping; thus the trapping time τ_{trap} is the only parameter that really affects it.

(2) Delay Time (τ_{delay}): Quasiparticles from events which are not exactly at the center of the absorber must diffuse different distances before reaching either junction. This results in different arrival times for the two current pulses. The delay time, τ_{delay}, is the difference in the two arrival times defined at a certain threshold current. By fitting τ_{delay} as a function of absorption location, one obtains an almost direct, "time of flight" measurement of the diffusion constant. The diffusion constant D is thus the only parameter that seriously affects the delay time.

(3) Curvature (Q_{center}/Q_{edge}): Quasiparticles created in the center of the device must diffuse a longer average distance/time than those created near the edge. If there are recombination losses in the absorber, the total charge will be less for events in the center. This gives curvature to the Q_1 vs. Q_2 plot. The ratio of the total charge in the center as compared to the edge (Q_{center}/Q_{edge}) indicates the amount of curvature. The curvature gives a measure of the ratio of loss time to diffusion time, so it is affected by both the diffusion constant (D) and the loss time (τ_{loss}).

(4) Peak Current (I_{pp}): We measure the peak current, I_{pp}, of each pulse. The value of the peak current scales with the initial charge of the pulse. It also depends on how quickly the charge reaches the junction – the faster the charge reaches the junction, the higher the peak current. If the charge reaches the junction more slowly, the tunneling current is spread over time and the peak current is reduced. Thus I_{pp} is most affected by the initial charge (Q_0), and somewhat less by the diffusion constant (D).

(5) Total Charge (Q_{tot}): The value of the total charge Q_{tot} scales with the initial charge, Q_0, and the outdiffusion time, τ_{out}. The outdiffusion time is relevant because it affects how many times each quasiparticle backtunnels.

In table 1 below we present the full spectrum of such information, the relative dependence of each measurement on each parameter. The dependencies are rated from 1 to 4, a '1' indicating a very weak dependence and a '4' indicating a very strong dependence, e.g. linear. The table then indicates the best way to extract all the parameters for a given device. We use the measurement with the strongest dependence to constrain each parameter. We start with the charge division and vary the value of τ_{trap} until the ratio (Q_1^{edge}/Q_2^{edge}) is fit. Since the charge division only really depends on the trapping time, we do not have to worry about the other parameters at this point. Similarly, we use the delay time to fit the value of D. Once we have constrained D, we vary τ_{loss} to fit the curvature. Then we fit Q_0 with the peak current, and τ_{out} with the total charge. This was the procedure used to obtain the fits in Fig. 4.1.1.

Measure-ment	τ_{trap}	D	τ_{loss}	Q_0	τ_{out}
Charge Division	4	1	2	1	1
Delay Time	2	4	1	1	1
Curvature	1	4	4	1	1
Peak Current	2	3	2	4	2
Total Charge	2	2	2	4	4

Table 4.1: relative dependence of the measured aspects of the current pulse on the model parameters. 1 = very weak dependence; 2 = weak dependence; 3 = strong dependence; 4 = very strong dependence

Note that we have neglected the tunnel time (τ_{tun}) from this discussion, not listing it as an "adjustable" parameter. The tunnel time affects the peak current and the total charge, but it is determined by the resistance of the tunnel barrier (equation 3.3.5), which we measure separately.

In Figs. 4.1.2-4.1.4 we show examples of the fits made for each parameter. Fig. 4.1.2 shows a plot of delay time vs. location, for two different values of threshold current. This measurement is used to fit the diffusion constant D. Note that a single value of D fits both sets of data, throughout the whole absorber. Fig. 4.1.3 shows a plot of Q_1 vs. Q_2, for different temperatures. (The temperature dependence of the charge will be explained later in section 4.3.) Note that the model fits the charge values well from the entire absorber, as one can see the effects of loss and trapping in the fits. Fig. 4.1.4 shows a plot

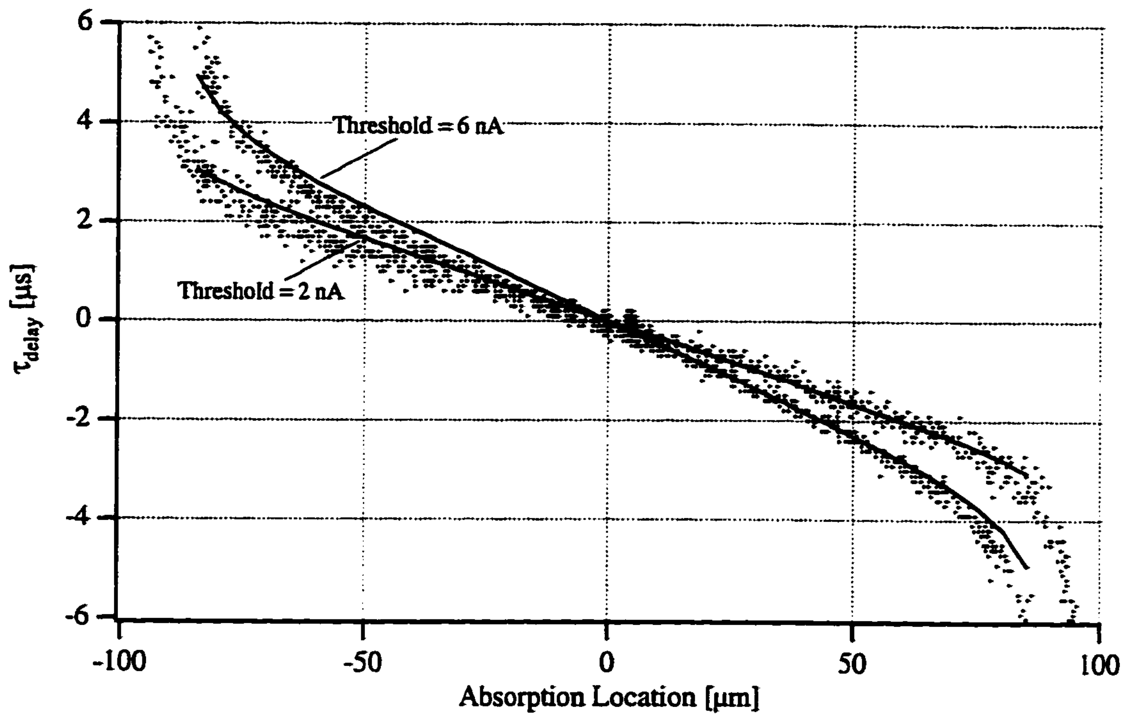

Fig. 4.1.2: Delay time versus absorption location, for threshold current of 2 nA and 6 nA. The fits from the model both assume a value of 8.5 cm^2/s for the value of D in tantalum. (8/7/96)

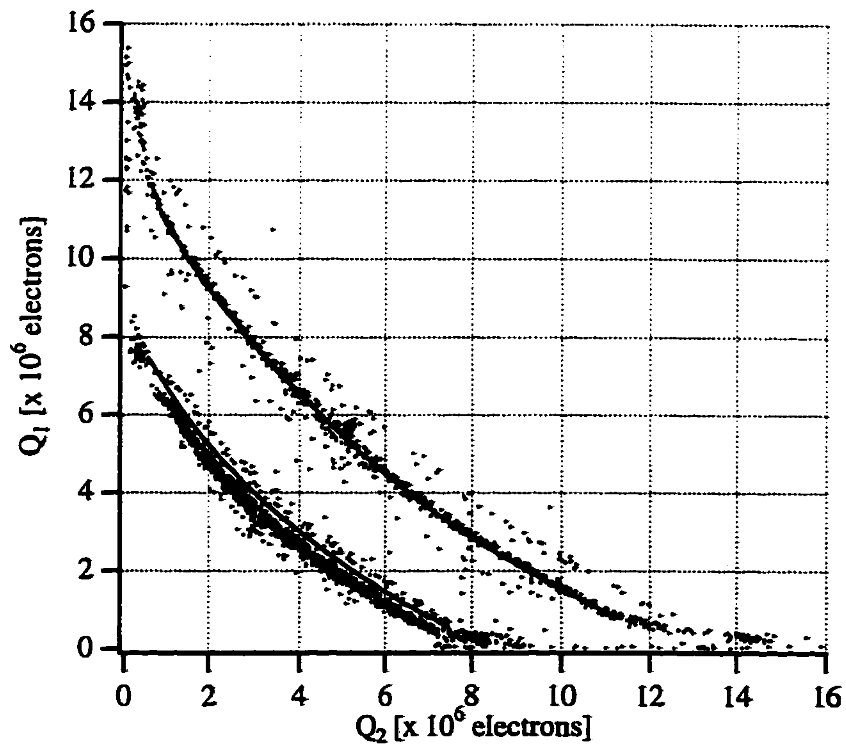

Fig. 4.1.3: Q_1 versus Q_2 for T = 0.225 K and T = 0.312 K. The solid lines show the fits from the model. (8/7/96)

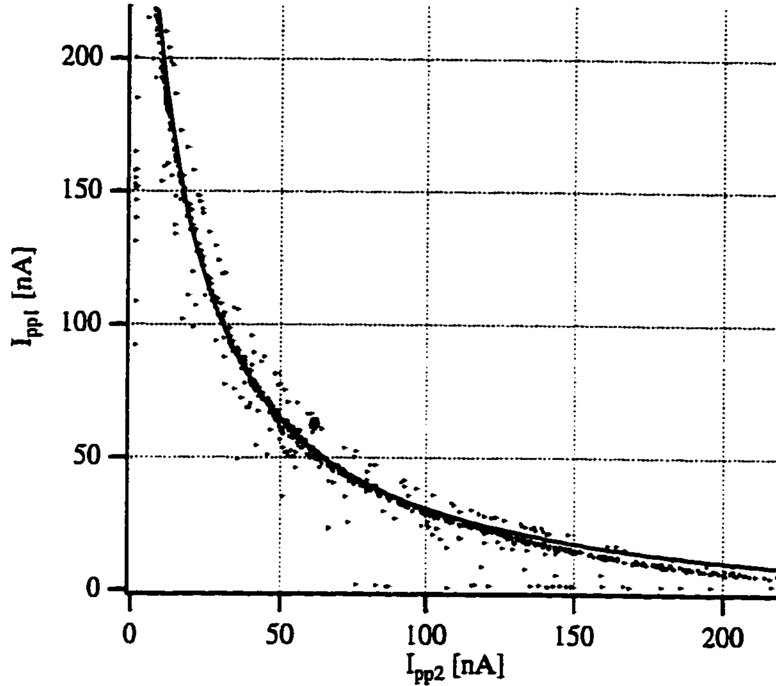

Fig 4.1.4: I_{pp1} versus I_{pp2}, with model fit. Data were taken at T = 0.225K. (8/7/96)

of the peak currents, I_{pp1} vs. I_{pp2}. The quality of the fit is good in all three cases. All three graphs are from the same cryogenic cooldown, and the fits are with all the same set of parameters. The ability to fit all measurements with a single set of parameters indicates the relative independence of each measurement, confirming that we have obtained a good physical understanding of the processes inside the detector.

4.1.2 Device Parameters

We have shown how to choose values for the input parameters that best fit the current pulse shapes. What remains is to discuss the physical implications of the parameter values – τ_{trap}, D, τ_{loss}, Q_0, τ_{out} – that best fit our devices. We discuss specifically the XN93 device, since this is the device measured most. Later in section 4.4 we will discuss the device fitting for newer devices and the contrast to XN93. Below we make comparisons to theory, comment on the implications for device operation, and compute several quantities which will be used later in the thesis. We discuss each parameter separately.

Trapping Time (τ_{trap}): The value for the trapping time is obtained by fitting the charge division. In the XN93 device it is found to be 10 ns. This compares favorably with a theoretical scattering time of 6 ns for a quasiparticle in aluminum at the gap energy of

tantalum. The fitting for τ_{trap} is not precise enough to be considered an actual measurement of the scattering time, but it does indicate consistency with the theory. The value of 10 ns indicates strong trapping and effective charge separation, which gives good spatial resolution. It also indicates good metallic interfaces between the tantalum absorber and the aluminum trap. If there were poor interfaces, the experimental value of τ_{trap} would be much larger than the scattering time of 6 ns (i.e. $\approx$ 100 ns - 1 μs).

Diffusion Constant (D): The diffusion constant is obtained by fitting the delay time versus absorption location throughout the whole absorber. Its experimental value in the XN93 device is $D_{exp} = 8.5$ cm^2/s. This is almost a factor of 5 lower than the theoretical prediction, $D_{th} = 40$ cm^2/s. The value for D_{th} is obtained from the value of D in the normal state times a reduction in the superconducting state. The value of D in the normal state is calculated from the Einstein equation, using the low temperature resistivity of our tantalum [Friedrich, 1997c]. This has a value $D_{normal} = 180$ cm^2/s. In the superconducting state D is reduced because the quasiparticle dispersion relation has a minimum near the gap edge causing the group velocity to go to zero. The degree of reduction depends on how close to the tantalum gap edge the quasiparticles relax. Using the simulation for quasiparticle relaxation only (see section 3.5), we find that the quasiparticles relax to a distribution with an effective diffusion constant of $D_{th} = 40$ cm^2/s. Thus the diffusion in the tantalum appears to be significantly slower than expected.

The slow diffusion is puzzling and has yet to have a satisfactory explanation. It is also seen by other groups [Cristiano, 1999; van den Berg, 1999], in more than one material. We speculate that it is due to small variations in the energy gap inside the absorber films. Quasiparticles would be temporarily trapped or restricted to the "valleys" of the gaps and be confined to the absorber for longer times. We have simulated this, and find that a small gap variation ($\approx$ 1%) is enough to explain the discrepancy in D. However, it is not yet clear that this gap variation should exist in our tantalum films; future experiments will hopefully shed more light on this. From a detector point of view it is also problematic, because it limits the size of the absorber.

Absorber Loss (τ_{loss}): The loss time in the absorber is obtained by fitting the curvature of the Q_1 versus Q_2 plot, the diffusion constant having been constrained by delay time measurements. We find a value of $\tau_{loss} = 30$ μs in the XN93 device. The loss is independent of temperature over the range of temperatures studied in our experiments. One

can see this from Fig. 4.1.3, where the degree of curvature in the Q_1 vs. Q_2 plots does not vary with temperature. Thus we see that the loss is due to some non-thermal process. We believe that it is due to quasiparticle trapping sites at the niobium contact in the center of the absorber, as niobium is well known to form metallic oxides. This is also believed to be a source of spatial noise in our detector (see discussion in section 5.4).

The combination of the slow diffusion and the loss time puts a limit on the size of the absorber one could eventually use. Astrophysical observations require x-ray absorbers of order millimeters in size. With the loss and diffusion times for the XN93 device, an absorber 1 mm in length would result in a factor of 10 lower signal than at present for events in the center. The present energy resolution is limited by electronic noise, which would be the same in the 1 mm device; hence the resolution for the 1 mm absorber would degrade by the same factor of 10 as the signal. This would be problematic. However, the situation is improving, as more recent devices do not seem show the same degree of loss (section 4.4). Since neither the diffusion nor the loss agree with their theoretical predications, one might be optimistic that future devices will do even better.

For noise considerations, the absorber loss can result in extra noise, as there are statistical fluctuations in the number of quasiparticles lost from one photon to the next. We calculate this in section 5.3. It is useful to know the constant β, which is the fraction of quasiparticles lost in the absorber. With a loss time of 30 μs the value of β is $\beta = 0.25$ for events in the center ($x_0 = 0$ μm), and $\beta = 0.12$ for events near the edge ($x_0 = 75$ μm).

Initial Charge (Q_0): The initial charge in the device is obtained by fitting the values of the peak currents, after the values of τ_{trap}, D, and τ_{loss} have already been constrained. We find a value of 8 x 10^6 electrons for the XN93 device.

The gap difference between tantalum and aluminum is more than twice the gap of aluminum: $\Delta_{Ta} - \Delta_{Al} \approx 3\Delta_{Al}$. When a quasiparticle enters the aluminum trap, it thus emits a phonon with an energy from 0 to $3\Delta_{Al}$. If a phonon is emitted with energy greater than $2\Delta_{Al}$, it can break a pair and create two quasiparticles. This results in multiplication of the initial charge. In our simulation we do not differentiate which fraction of charge is created in the initial absorption and which fraction comes from multiplication upon trapping. The value of Q_0 is thus the product of the created charge, $Q_{created}$, and the multiplication factor, α: $Q_0 = \alpha\, Q_{created}$. The created charge has been estimated from simulations of the initial

energy cascade. Using Kurakado's [Kurakado, 1982] estimate that $Q_{created} = E_x / (1.7\ \Delta)$, we find $Q_{created} \approx 5 \times 10^6$ electrons in tantalum at 6 keV. Thus we estimate $\alpha = 1.6$, which agrees well with our calculations [Friedrich, 1997b]. We will use this factor in the calculation of the trapping noise (section 5.3).

Outdiffusion Time (τ_{out}): The outdiffusion time is fitted last and is chosen to match the total charge. Larger values of the outdiffusion time give more charge due to increased backtunneling. The outdiffusion time for the XN93 device is 7.1 μs, although this parameter can vary by ≈ 25% over different cooldowns. We believe that the variation is due to small amounts of trapped flux in the aluminum junctions, which can act as trapping sites for quasiparticles. This would be indistinguishable from outdiffusion, since both outdiffusion and trapping sites remove quasiparticles from the tunneling region in a temperature-independent fashion. The value of τ_{out} is somewhat consistent with the measured [Friedrich, 1997c] diffusion constant in aluminum ($D_{Al} = 60\ cm^2/s$).

The value of the outdiffusion time determines how much signal increase is obtained from backtunneling. In the limit where outdiffusion from the counterelectrode is the dominant process which removes quasiparticles from the tunneling region, the average number of times a quasiparticle tunnels, $\bar{n}$, is given by

$$\bar{n} = 1 + 2\frac{\tau_{out}}{\tau_{tun,CE}}, \qquad (4.1.1)$$

where $\tau_{tun,CE}$ is the tunnel time from the counter-electrode. In the XN93 device the counter-electrode has approximately four times the volume as the trap, making $\tau_{tun,CE}$ four times larger than τ_{tun}, the tunnel time from the trap ($\tau_{tun} = 2.4\ \mu s$). From equation 4.1.1, then, an outdiffusion time of 7.1 μs gives $\bar{n} = 2.5$. An initial charge of 8 million electrons times a backtunneling gain of 2.5 gives 20 million, or 10 million per junction for events in the center. In the center we lose 25%, so this reduces to 7.5 million. We actually collect 5.2 million electrons (see Fig. 4.1.3). The other 30 % of the charge is canceled by reverse processes (section 3.3). This results in a value of $\gamma = 0.15$, where γ represents 1/2 the fraction of the canceled charge. This is used in the noise calculations (see section 5.3).

4.2 Dynamic I-V Curve

The discussion of the device physics so far has been focused mainly on dynamics, namely the time evolution of the quasiparticle spatial distribution after a photon is absorbed. No mention yet has been given to the quasiparticle *energy* distribution. A major step forward in our understanding of the device physics was made after carefully considering the energy distribution of quasiparticles during tunneling. The effects of the quasiparticle energy distribution are seen in the *voltage* dependence of the current and charge. In this section we discuss the dynamic I-V curve and its impact on the signal and the noise.

4.2.1 Quasiparticle Energy Distribution

After the quasiparticles have diffused through the absorber and reached the aluminum trap, they scatter inelastically toward the aluminum gap energy. We assume they have fully thermalized to the gap edge in tantalum, so they enter the aluminum trap at an energy of Δ_{Ta} = 700 μV≈ $4\Delta_{Al}$. The scattering time in aluminum for a quasiparticle at an energy of $4\Delta_{Al}$ is rapid, τ_{scat} = 6 ns. This is much faster than the tunnel time, τ_{tun} = 2.4 μs. One might conclude from this that the quasiparticles will have thermalized completely before they tunnel, having all scattered to within an energy of ≈ $k_B T_{bath}$ of Δ_{Al}. However, τ_{scat} is the time for a quasiparticle to scatter to *any* energy below $4\Delta_{Al}$, not necessarily to an energy within $k_B T_{bath}$ of the gap. The time for the whole distribution to thermalize is in fact much longer. This is because the inelastic time is a very strong function of energy, with lower energies giving much longer scattering times (see section 3.2). Hence quasiparticles that do not scatter to within $k_B T_{bath}$ of Δ_{Al} on their first scattering will survive much longer at their new energy, and the full thermalization will take much longer than the initial 6 ns.

Since the scattering times are a function of energy, one needs an iterated computer algorithm to calculate the quasiparticle energy distribution. This was described in section 3.5. In Fig. 4.2.1 we plot the calculated energy distribution of quasiparticles in the Al trap after 0.1 μs and 1 μs. The quasiparticles were started at an energy of Δ_{Ta} = 700 μV. One can see that even after 1 μs there are still a significant number of quasiparticles in the energy range 70 – 100 μeV above the aluminum gap. Although this is clearly a non-equilibrium situation, it is convenient to describe this distribution with an "effective temperature" (T_{eff}). Here T_{eff} is defined as the temperature of the thermal distribution which most closely approximates the actual quasiparticle distribution. From the figure we estimate $k_B T_{eff}$ ≈ 60 μeV; thus T_{eff} ≈ 0.7 K, significantly larger than T_{bath} = 0.22 K.

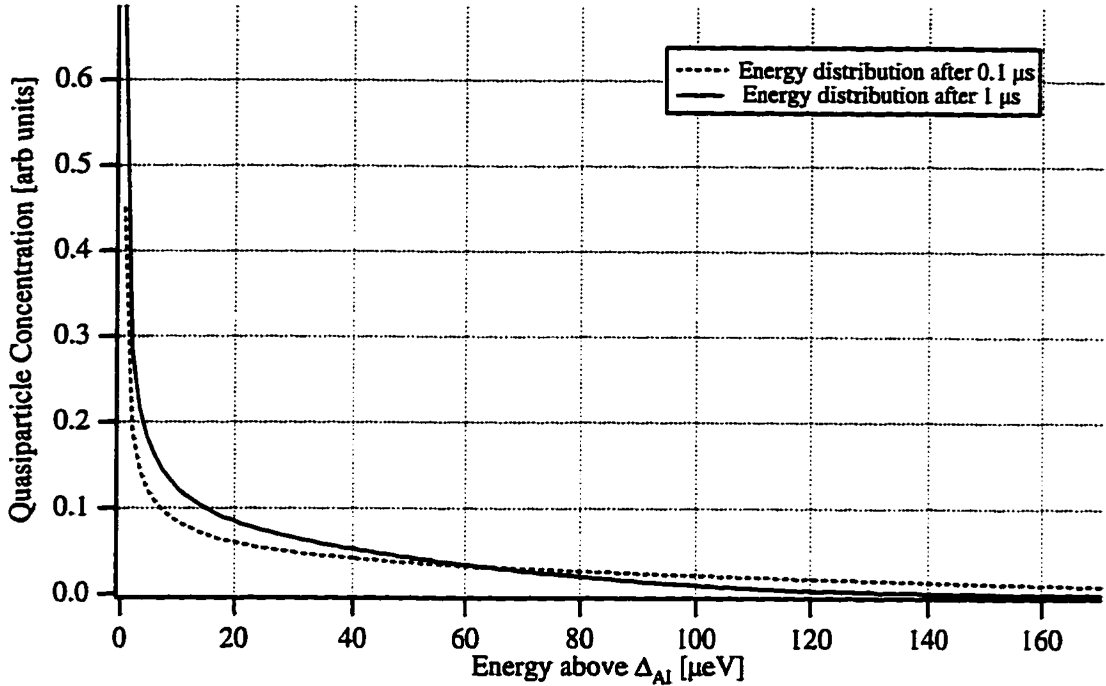

Fig. 4.2.1: Calculated energy distribution in Al trap during tunneling, after 0.1 μs and 1 μs. The effective temperature after 1 μs is estimated at T_{eff} = 0.7 K.

In section 3.3 we discussed the thermal I-V curve of an SIS junction, and saw how the current is increasing in the region where $V_{dc} < k_B T_{bath}/e$ (low bias), and is constant in the region where $V_{dc} > k_B T_{bath}/e$ (high bias). In Fig. 4.2.2 we plot the thermal I-V curve for our device. We next draw in schematically an I-V curve with T_{bath} replaced by T_{eff} (keeping the value of $\Delta = \Delta(T_{bath})$). This is our estimation of the I-V curve during a pulse (the dynamic I-V curve), since during tunneling the quasiparticles are at the elevated temperature of T_{eff}. Our typical bias voltage is V_{dc} = 70 μV. A bias voltage of 70 μV is in the high bias region (constant current) in the quiescent case, with no x-ray current flowing. However, in the dynamic state the same bias point moves into the low bias region (increasing current). Note that we are not able to bias any higher than 70 μV with the existing junctions due to the presence of Fiske modes (see Fig. 4.2.2), which give excess noise when biasing in their vicinity. From Fig. 4.2.2, then, we see that the slope of the I-V curve has increased significantly in the dynamic state. This change in slope is of particular significance for device operation. There are two major implications of this: the integrated charge is an increasing function of bias voltage, and the differential resistance, dV/dI, is decreased during a pulse. We discuss these below.

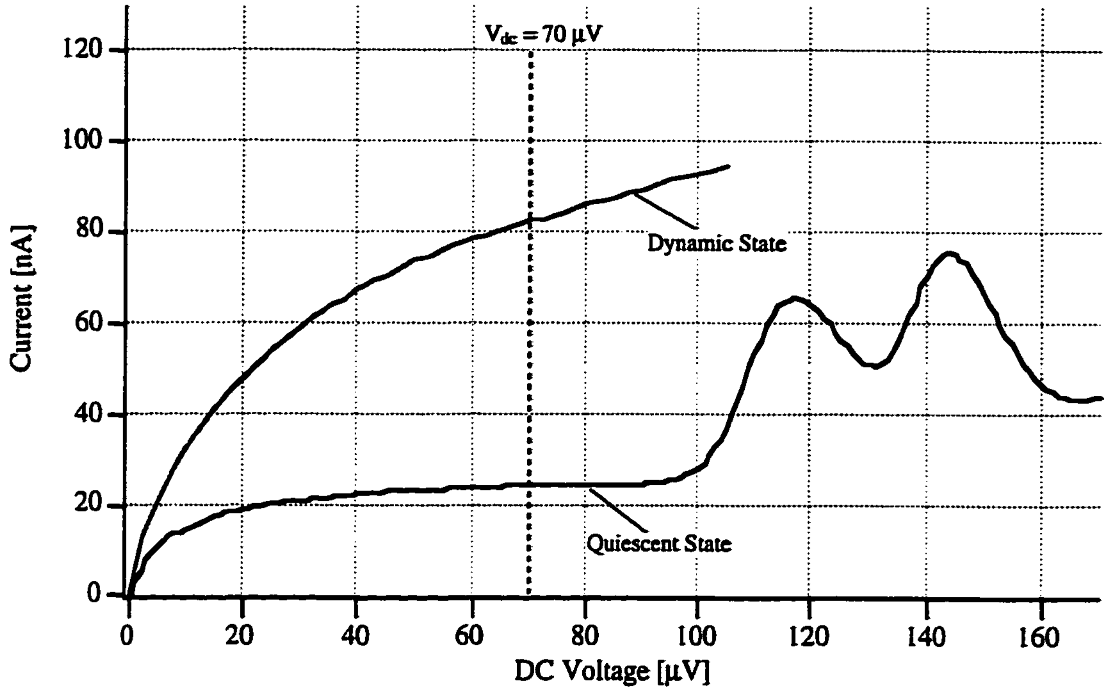

Fig. 4.2.2: I-V curve for our device in the quiescent state and the dynamic state. The I-V in the quiescent state is measured, whereas the one in the dynamic state is our estimate of the behavior.

4.2.2 Charge versus Bias Voltage

The total collected charge (Q) from an x-ray photon is simply the time integral of the total current, I(t), minus the DC current, I_{dc}:

$$Q = \int [I(t) - I_{dc}] dt. \tag{4.2.1}$$

In the voltage range $20\ \mu V < V_{dc} < 80\ \mu V$, above the initial current increase and before the Fiske modes, the DC current can be considered to be constant. In this region, then, we would expect the voltage dependence of the charge Q to be the same as the current I(t). In Fig. 4.2.2 we approximated I(t) as being similar to a thermal I-V curve with an effective temperature T_{eff}, estimated to be $\approx$ 0.7 K. One would then expect similar qualitative behavior from the Q-V curve.

The plot of collected charge versus bias voltage is shown in Fig. 4.2.3. The markers are the experimental points and the solid line is a fit from the model of the current pulse. We see that the charge is an increasing function of voltage even as high as 60 µV, indicating that our qualitative picture of an elevated temperature for the quasiparticles is confirmed. If the quasiparticles were instead at the bath temperature, one would expect the charge to be constant above $k_B T_{bath}/e \approx 20\ \mu V$. The fit from the model is of good quality, indicating that we seem to have accounted well for the elevated quasiparticle temperature. Recall that the model does not use the approximation of an effective temperature but rather

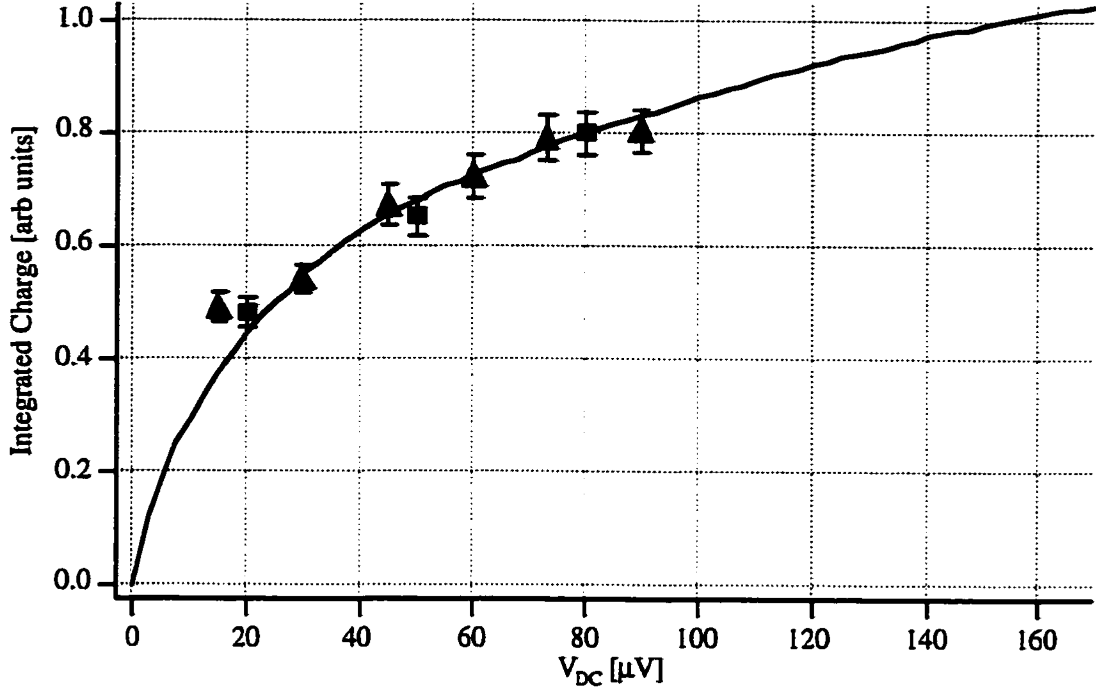

Fig. 4.2.3: Charge versus bias voltage, with fit from the current pulse model. (1/20/97 and 1/11/99)

uses the full time evolution of the quasiparticle energy distribution in the junction. Future experiments may shed more light on this issue, but it is clear that our picture so far is at least a good estimate of this complex behavior. For noise purposes it is useful to know the slope of the Q versus V curve in Fig. 4.2.3 at a typical bias point, normalized to units of energy. We find that $\left[{}^{E_x}\!/_{Q}\right]{}^{dQ}\!/_{dV} = 30\,{}^{eV}\!/_{\mu V}$ from Fig. 4.2.3 at 70 μV.

4.2.3 Dynamic Resistance during a Pulse

In addition to affecting the voltage dependence of the integrated charge, the change in the I-V curve during a pulse also causes a decrease in the differential resistance, $(dI/dV)^{-1}$. We will denote the differential resistance as R_{eff}, where $R_{eff} = R_{quies}$ in the quiescent state but decreases to a smaller value in the dynamic state. An estimate of R_{eff} can be obtained from a plot of peak current (I_{pp}) versus bias voltage, shown in Fig. 4.2.4. We have plotted the peak currents for events from the center (x_0 = 0 μm) and near the edge (x_0 = 75 μm). The slope of the graph, dI_{pp}/dV_{dc}, has units of Ω^{-1} and its inverse, $(dI_{pp}/dV_{dc})^{-1}$, gives the value of the differential resistance at the peak of the pulse. From the graph we

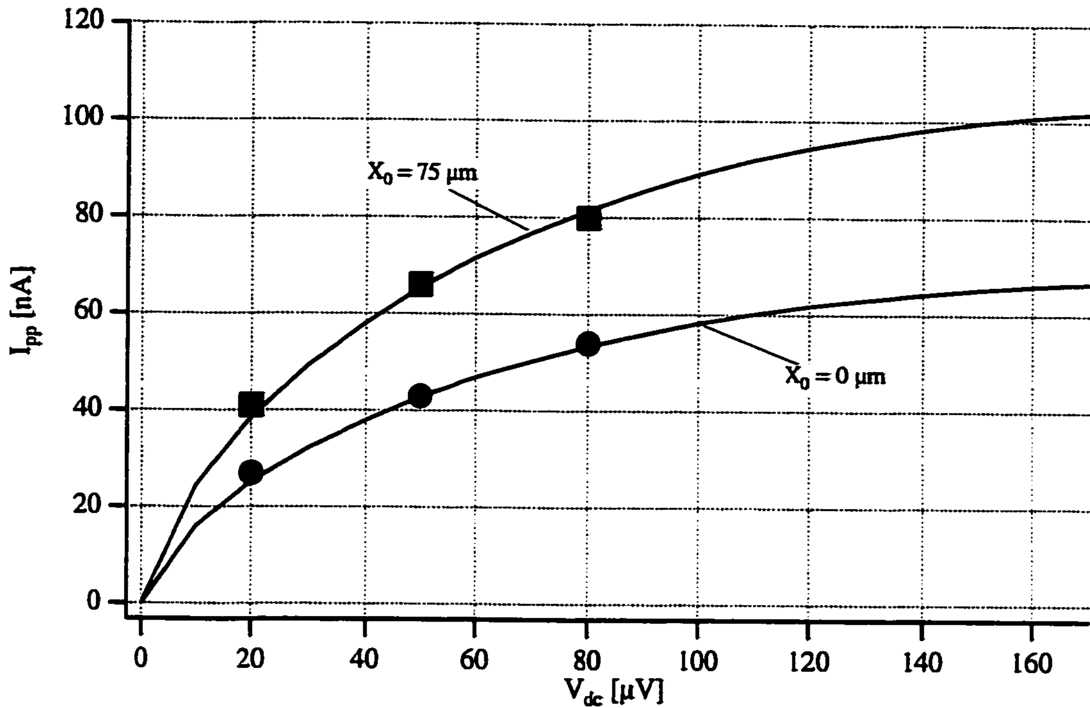

Fig. 4.2.4: Peak current versus bias voltage, for events from the center and the edge. The events from the edge have a smaller resistance (larger slope). The solid lines are fits from the model. (1/20/97)

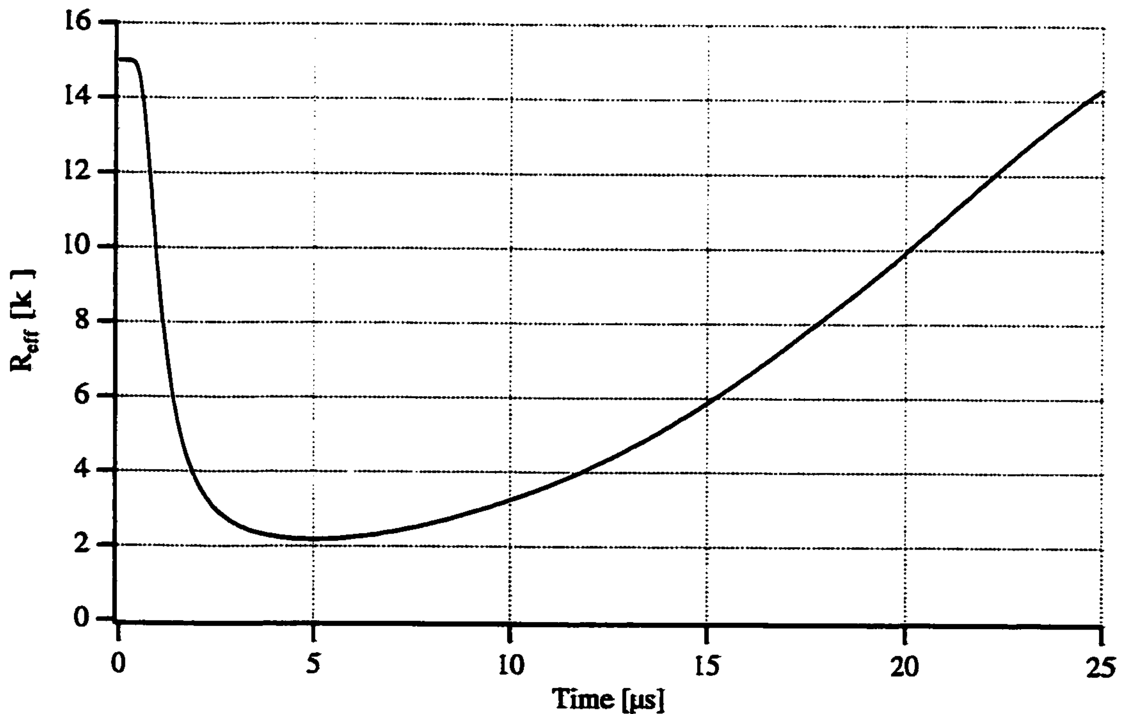

Fig. 4.2.5: Simulation of R_{eff} during a pulse from the current pulse model, considering an event from the center. The value of R_{eff} is lowest at the peak of the pulse.

find a value of ≈ 2.5 kΩ in the center and ≈ 1.5 kΩ near the edge. This is considerably lower than the resistance in the quiescent state, R_{quies} ≈ 15 kΩ.

In general the value of R_{eff} is time dependent: it starts with a value of R_{quies} at the beginning of the pulse, decreases to a smaller value at the peak of the pulse, and then returns to the value of R_{quies} at the end of the pulse. Fig. 4.2.5 shows a simulation of R_{eff} versus time from the model of the current pulse for an event from the center. The values obtained from Fig. 4.2.4 are from the peak of the pulse, so they represent the *lowest* value that R_{eff} reaches. The pulses from the edge events have higher peak currents, so they give correspondingly lower values of R_{eff}. Note that the same holds true for events with higher *energy* – they have higher currents (from a higher initial charge), so have lower values of R_{eff}. This is an important point, that the decrease of R_{eff} scales with the photon energy.

The decrease in R_{eff} during a pulse has implications for the signal and the noise. The electrical representation of the junction, the Norton equivalent [Johnson, 1989], is a current source in parallel with a source resistance. The junction is a highly non-linear device, but for small signals and noise the source resistance can be approximated as the differential resistance R_{eff}. The current amplifier has a non-zero input resistance due to the finite value of its open-loop gain (A_{OL}). In chapter 2 we found the amplifier resistance to be $R_A \approx 100\Omega$. Additional resistance in series with the junction (R_S), including the lead resistance, also adds to R_A. The finite value of R_{eff} then gives current division between the amplifier and the junction (see Fig. 4.2.6). For lower values of R_{eff}, more current flows through R_{eff} and less flows through the amplifier. This reduces the current through the amplifier (I_A) from the initial x-ray current $I_{x\text{-ray}}$:

$$I_A = I_{x-ray}\frac{R_{eff}}{(R_A + R_S) + R_{eff}}. \qquad (4.2.2)$$

If the value of R_{eff} is the quiescent value, R_{quies} = 15 kΩ, then this is a negligible effect (<1%). However, if the value of R_{eff} is closer to the $\approx$ 1-2 kΩ estimated from Fig. 4.2.4, then the current division in equation (4.2.2) is important ($\approx$ 10%).

We have seen from Fig. 4.2.4 that the events from the edge of the absorber have higher peak currents than those in the center, resulting in lower values of R_{eff}. If the current division from equation (4.2.2) is significant in our devices, one would then expect it to be more pronounced for events from the edge. In Fig. 4.2.7 we demonstrate this with scatter plots of Q_1 versus Q_2 for different values of the amplifier plus series resistance (R_A + R_S). We can increase R_S by simply adding extra resistance in series with the junction. We see that larger values of (R_A + R_S) cause a reduction in the amount of curvature in the Q_1 vs. Q_2 plots. The reduction in curvature is simply because the edge events have lost more charge from the current division in equation (4.2.2) than events from the center. This once again demonstrates that the edge events have lower values of R_{eff}, and also indicates that the effect of the charge division is clearly significant.

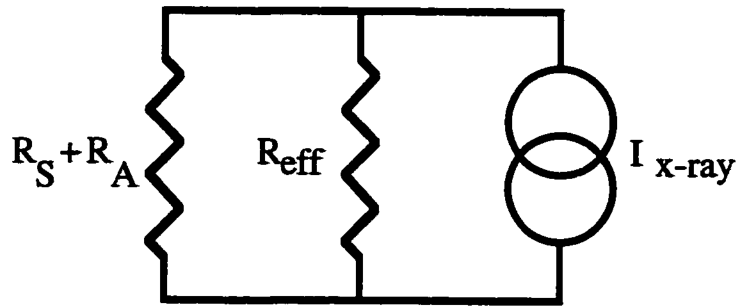

Fig. 4.2.6: Current and charge division from the finite amplifier (R_A) and series (R_S) resistance. The junction impedance is approximated as R_{eff}

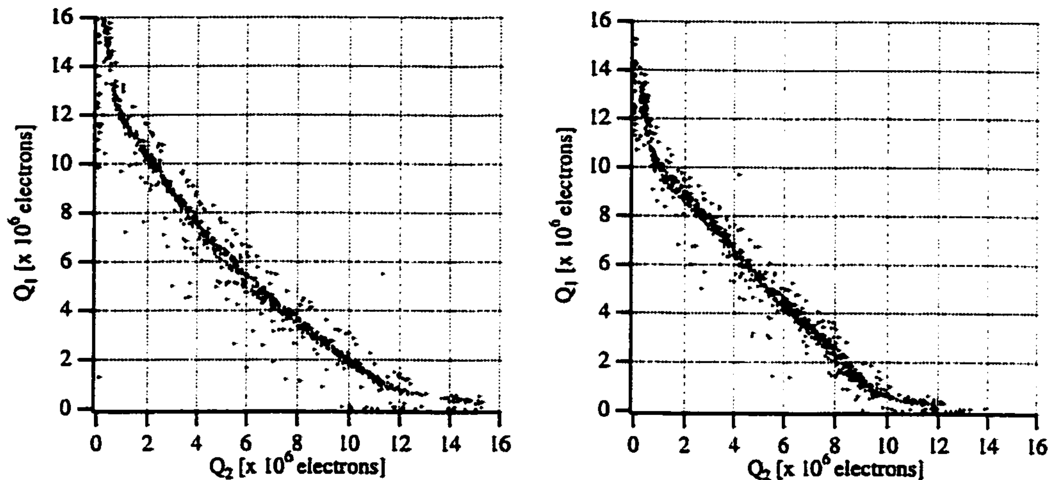

Fig. 4.2.7: Q_1 versus Q_2 for different values of series resistance. The plot on the left has R_s = 100Ω, while the plot on the right has R_s = 400Ω. The curvature is different in the two plots. (12/16/98)

The charge division is more magnified for larger values of (R_A + R_S), and at high values of series resistance (R_S = 400 Ω) the Q_1 vs. Q_2 straightens out completely.

The change in curvature is problematic because it affects the extraction of the loss time (see section 4.1). The straight Q_1 vs. Q_2 might be thought to falsely indicate there are no absorber losses. Experiments where we extract the loss time therefore have amplifier and series resistances which are as small as possible. One might suggest that the addition of extra series resistance could be used to remove the effect of the losses, making the extraction of the photon's location simpler. However, this would not work in a real experiment, since there would be photons of different energy hitting the detector. The value of R_{eff}, as mentioned previously, depends on the energy. The chosen value of series resistance would only straighten out the Q_1 vs. Q_2 for one particular energy.

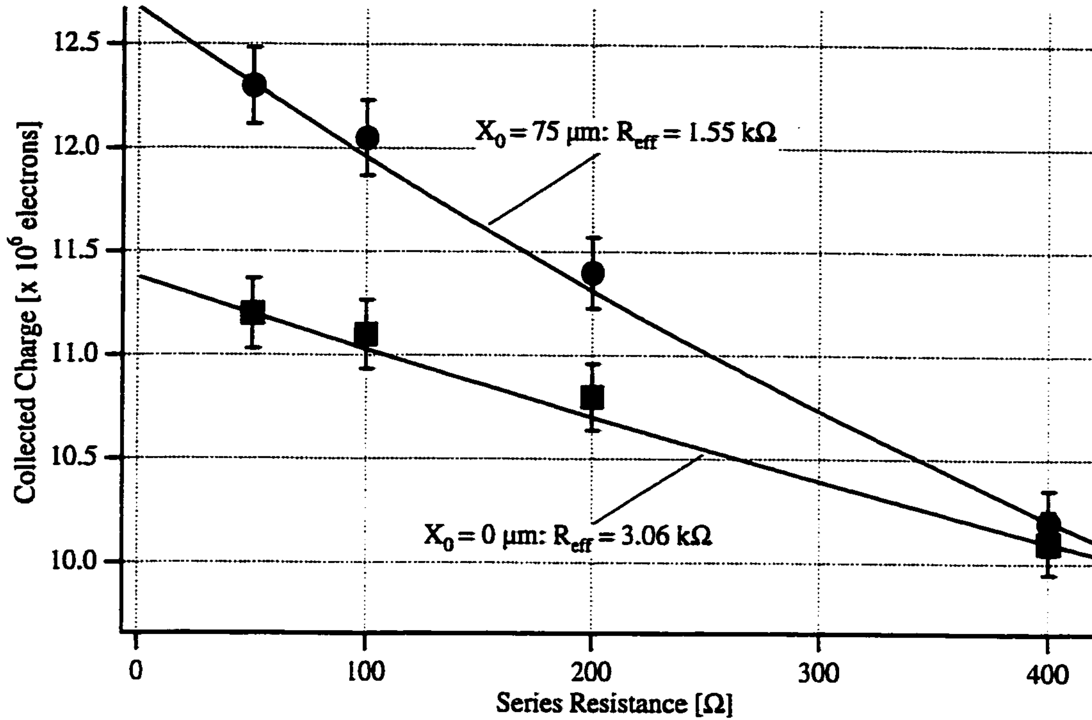

Fig. 4.2.8: Charge versus series resistance, for events from the center and the edge. The data are fit with the current division equation (4.2.2), and the values for R_{eff} are extracted. (12/16/98)

In Fig. 4.2.8 we use the additional series resistance to calculate the value of R_{eff} using the charge division. We plot the total charge versus series resistance (R_S) for events in the center and at the edge. The amplifier resistance in this plot is constant. The charge loss for higher values of series resistance is fit using the current division from equation (4.2.2). We find a value of $R_{eff} = 3060\ \Omega$ for events from the center ($x_0 = 0\ \mu m$) and $R_{eff} = 1550\ \Omega$ for events from the edge ($x_0 = 75\ \mu m$). Both fits assume $R_A = 100\ \Omega$. Because they are fit using the *charge*, these values for R_{eff} are somewhat larger than the values from Fig. 4.2.4, which uses the peak current. The values extracted from Fig. 4.2.7 represent the time average of R_{eff}. This is, in general, the best approximation to R_{eff} if it is assumed to be a single number. We will see that the number of 1.55 kΩ on the edge also agrees well with R_{eff} extracted from the noise (see section 5.1).

• • • • • • • •

In summary, the change in the slope of the I-V curve during a pulse has two major effects: the integrated charge is a function of bias voltage and the differential resistance is reduced. We have seen how they impact the signal from our detector; later in chapter 5 we will see they impact the noise as well. The incomplete thermalization of quasiparticles in the trap before tunneling is thus seen as a major effect in our devices.

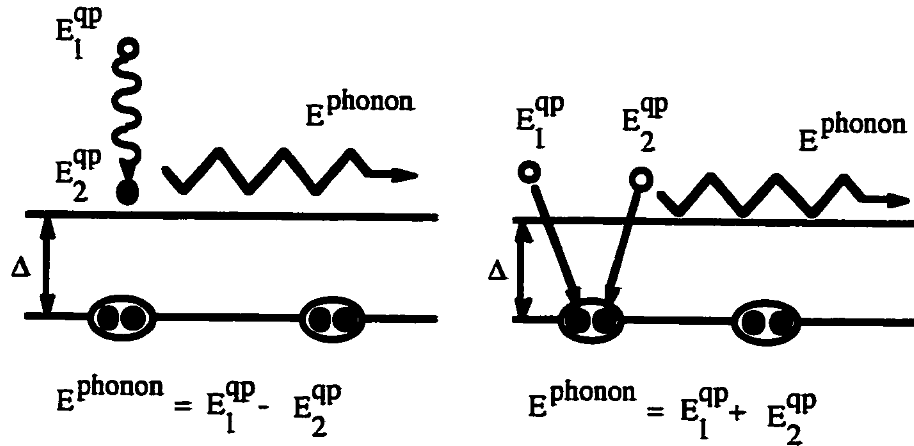

Fig. 4.3.1: Thermalization (left) and recombination (right) are both mechanisms of phonon emission.

4.3 Electron-Phonon Scattering

The mechanism for thermalization of quasiparticles in the trap is by electron-phonon scattering: a quasiparticle scatters to lower energy by emitting a phonon (see Fig. 4.3.1). The energy distribution that the quasiparticles reach before tunneling, i.e. their effective temperature, depends on the scattering time as compared to the tunnel time. Shorter scattering times will result in more cooling and a lower T_{eff}, while longer scattering times will result in less cooling and a higher T_{eff}. In the previous section we saw how the charge versus bias voltage was a measure of the quasiparticle energy distribution and the effective temperature. Here we will use this information to estimate the electron-phonon scattering time.

In addition to the energy distribution, the electron-phonon scattering time also affects the strength of quasiparticle recombination. Two quasiparticles that recombine and form a Cooper pair emit a phonon of energy $E_{phonon} > 2\Delta$ (see Fig. 4.3.1b); therefore the time to recombine is related to the time for phonon emission. The strength of quasiparticle recombination can thus provide another measure of the electron-phonon scattering time. In this section, then, we will see how we can use the experimental evidence from both the charge versus bias (thermalization) and the charge versus temperature (recombination) as a measure of the electron-phonon scattering. Recall from section 3.2 that the characteristic electron-phonon time is the parameter τ_0, so this is what we are interested in estimating.

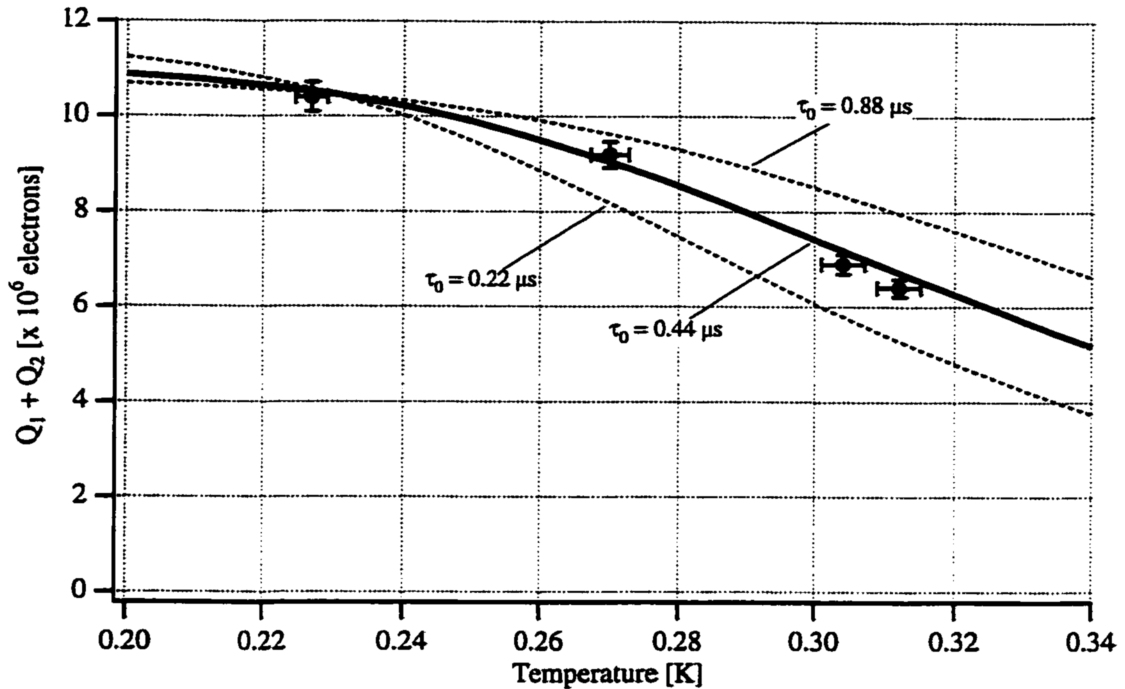

Fig. 4.3.2: Charge versus temperature. The data are fit with the current pulse model, with different values of the electron-phonon time τ_0. (8/7/96)

4.3.1 Recombination

We consider recombination first. The time for an excess quasiparticle to recombine with a thermal quasiparticle was given in section 3.4. It is proportional to τ_0 and inversely proportional to the thermal density of quasiparticles. Note that when we speak of recombination here we are speaking of recombination in the aluminum junctions, not in the tantalum absorber. We show the charge versus temperature in Fig. 4.3.2, where the charge is taken from absorption events at the center of the absorber. Higher temperatures result in a higher density of thermal quasiparticles and a shorter recombination time, so the charge is reduced. Also shown in the figure are three fits from the model. The three fits are using different values of τ_0: τ_0 = 0.44 μs, the theoretical value for Al calculated by Kaplan, et al.; τ_0 = 0.22 μs, two times smaller; and τ_0 = 0.88 μs, two times larger. From the graph it is clear that the theoretical value of 0.44 μs provides the best fit to the data.

The behavior of the charge versus temperature for different values of τ_0 is somewhat complex and is worth discussing. Consider first low temperatures, where the number of thermal quasiparticles is very small. Recombination is negligible, so smaller values of τ_0 give more charge due to improved thermalization. At high temperatures,

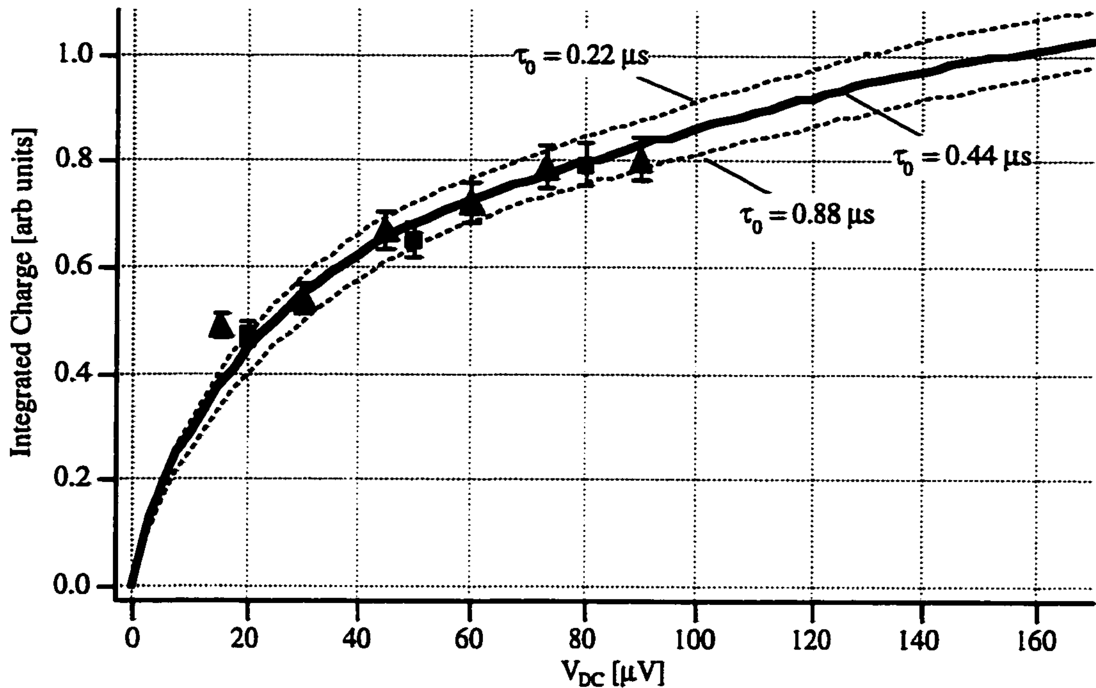

Fig. 4.3.3: Charge versus Bias voltage, fit with different values of τ_0. (1/20/97 and 1/11/99)

however, the number of thermal quasiparticles is significant and recombination dominates. Here smaller values of τ_0 give *less* charge, because the faster inelastic time results in more recombination. Curves for different values of τ_0 will thus cross over, at the temperature where recombination starts to dominate over thermalization. We can see from the graph for our devices that this cross-over temperature is about 0.23 K. By operating our detectors at 0.22 K we are thus in the limit where thermal recombination is almost negligible.

4.3.2 Thermalization

In Fig. 4.3.3 we do the same fitting for the charge versus bias. Note that this is the same experimental data from Fig. 4.2.3, except that we have now added the fits for τ_0 = 0.22 μs and τ_0 = 0.88 μs. Once again the theoretical value of 0.44 μs gives the best fit. However, this evidence is not as strong as the temperature fitting. The effect of τ_0 on the thermalization is much less, as one can see the three curves are much closer to each other than in the case of recombination. In addition, the shapes of the three curves are almost identical, whereas the high temperature behavior for recombination has clearly different shapes for the different values of τ_0. It does show a consistency, though, that the same

value of τ_0 fits both the temperature *and* the bias dependence of the charge. The self-consistency gives us more confidence in our model and its ability to extract the detector physics.

4.4 New Devices

The results presented thus far have all been from a single device, XN93, which was fabricated over five years ago. In this section we will explore the results from two newer devices with different designs which were made in a very recent fabrication run. The objective of the new designs is to test two new ideas for improving the energy resolution. Here we will present the preliminary results. Full experiments on the electronic noise and energy resolution have yet to be performed, but even at this point the devices provide an interesting contrast to the XN93 device. The results are encouraging for the next generation of detectors, with only one or two potential difficulties.

In table 2 below we summarize the differences between the XN93 device and the two new devices: the **small junction device** (F99-11C) and the **backtunneling device** (F99-14C). The small junction device has junctions of smaller length (in the y-direction) and area. It is designed to increase the voltage of the first Fiske mode, such that biasing at higher voltages is possible. It should also have a reduced shot noise, due to its increased normal state resistance. The backtunneling device is designed to enhance backtunneling. It has a tantalum wiring layer, whose large gap should prevent quasiparticles from diffusing away from the counterelectrode. In the table we include the tunnel times from both the trap and the counter-electrode. Note the large difference in tunnel times from the counterelectrode. The backtunneling device has a very small counterelectrode/wiring volume due to the tantalum plug, whereas the small junction device has a very large aluminum wiring layer. In section 2.1 we described difference between the new devices and XN93.

Device	L_{jct} [μm]	A_{jct} [μm²]	d_{trap} [nm]	V_{trap} [μm³]	V_{ce+w} [μm³]	wiring	$t_{tun,tr}$ [μs]	$t_{tun,ce}$ [μs]
XN93	200	1860	1500	700	2800	Al	2.4	9.6
F99-11C	120	560	2100	517	9133	Al	5.0	88
F99-14C	200	1860	2100	839	368	Ta	2.1	0.9

Table 4.2: New device parameters. L_{jct} = junction length; A_{jct} = junction area; d_{trap} = trap thickness; V_{trap} = trap volume; V_{ce+w} = (counterelectrode + wiring) volume; wiring = wiring type; $\tau_{tun,tr}$ = tunneling time, trap; $t_{tun,ce}$ = tunneling time, counterelectrode

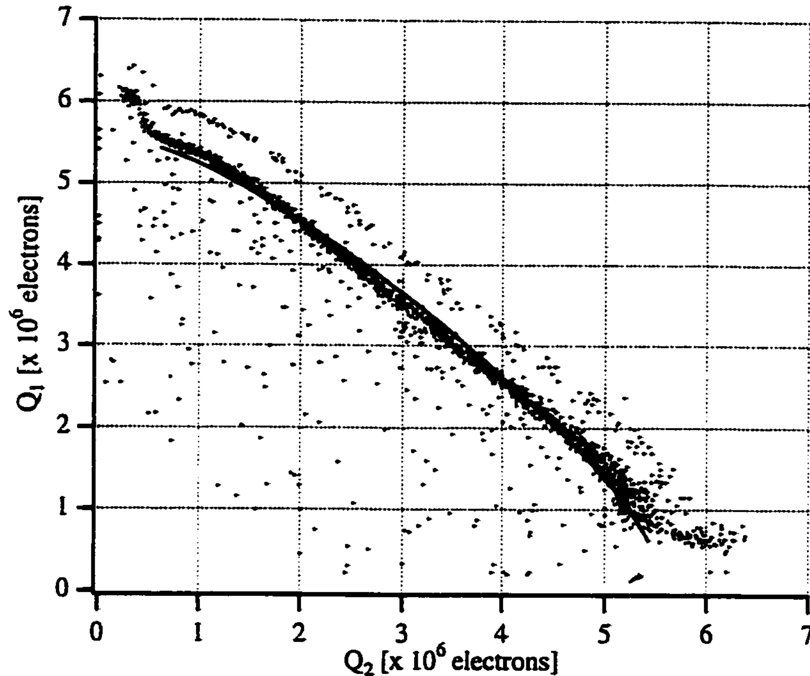

Fig. 4.4.1: Q_1 versus Q_2 for the small junction device F99-11C, with fit. (6/11/99)

The newer devices were cooled down and biased in the usual fashion. The small junction device had very good subgap current (≈ 10 nA) and dynamic resistance (≈ 50 kΩ) for both of the junctions. The backtunneling device, however, had lots of leakage current (≈ 750 nA total subgap current) and very poor dynamic resistance (≈ 90 Ω). The small junction device could indeed be biased at higher voltage, V_{dc} = 100 μV, but not as high as our calculations predicted. The findings from the pulse shapes for x-rays are summarized below.

4.4.1 Small Junction Device

The Q_1 versus Q_2 plot for the small junction device is shown in Fig. 4.4.1. The most striking feature of the graph is the reverse curvature – events from the center give *more* charge than from the edges. This is the opposite effect of quasiparticle loss in the absorber. This illustrates a different effect, which was for the most part absent in the XN93 device: self-recombination of excess quasiparticles in the aluminum trap. The small junction device has a slightly smaller trap volume (517 μm³ compared to 700 μm³ for XN93), and a longer tunnel time (5.0 μs compared to 2.4 μs). The smaller junction volume results in a somewhat higher density of excess quasiparticles, while the longer tunnel time means that the excess quasiparticles spend more time in the trap before they tunnel. Both effects increase the fraction of quasiparticles lost to self-recombination. The

total number of quasiparticles lost to self-recombination is more for events from the edge, since they have higher peak currents and higher quasiparticle densities, in a given trap. This results in the reverse curvature that is observed in Fig. 4.4.1.

The fit from the current pulse model is shown, and it is apparent that the model at least confirms the qualitative aspects of the picture above. The change in trap volume and tunnel time in the new device should give ≈ 2.5 times the self-recombination we saw in the XN93 device. This is not a particularly large difference. The fact that self-recombination is important in this new device whereas it was largely absent in XN93 indicates that the XN93 device is probably very close to having significant self-recombination itself. Future devices need to avoid this, since self-recombination leads to reduced signal, non-linear energy response, and the decreased ability to extract the photon absorption location. We will discuss how to avoid self-recombination in future devices in section 5.6.

The fit from Fig. 4.4.1 assumes very little absorber loss (> 1ms). This is significantly better than XN93 and is obviously good news for future devices. However, one must be cautious: it is possible that the reverse curvature from the self-recombination is hiding some amount of absorber loss. One could achieve a similar fit as Fig. 4.4.1 with some amount of absorber loss and slightly stronger self-recombination (= smaller τ_0). The experiment should be repeated in a device with less self-recombination to be certain of the improved loss time.

The other fitting parameters are similar to XN93. The diffusion constant is almost the same, 9.5 cm^2/s as compared to 8.5 cm^2/s; both are still lower than theory. The initial charge is slightly higher, 8.8 million electrons as compared to 8.0. This, however, would be expected, due to the larger trap thickness in the small junction device. A thicker trap would result in a longer escape time for phonons, meaning that a larger percentage of charge will multiply upon trapping. The 40% increase in thickness would result in a similar increase in phonon escape time. This would predict ≈ 10 – 15% more multiplication, consistent with what is observed. The trapping time for the fit in Fig. 4.4.1 is 10 ns, the same as XN93. The table below summarizes the fitting parameters for the new device.

The outdiffusion time is also similar to XN93, which is somewhat surprising. The small junction device has very wide wiring leads. This is a change from the XN93 device, which has narrow leads that only go off in one direction (see picture in section 2.1). We had anticipated that this change would lead to a significant reduction (~ 10) in the outdiffusion time in the new device. This, however, is apparently not observed. The outdiffusion time is most likely being limited by the slow diffusion in the aluminum

counterelectrode, and as such it will be difficult to make it much shorter in future devices. It may be possible to use a normal metal wiring lead which would act as a quasiparticle sink to accelerate the flow of charge away from the tunneling area.

Device	τ_{trap}	D	τ_{loss}	Q_0	τ_{out}
XN93	10 ns	8.5	30 μs	8.0 x 10^6	7.1 μs
F99-11C	10 ns	9.5	> 1 ms	8.8 x 10^6	5.0 μs

Table 4.3: Parameters extracted from F99-11C compared with those from XN93.

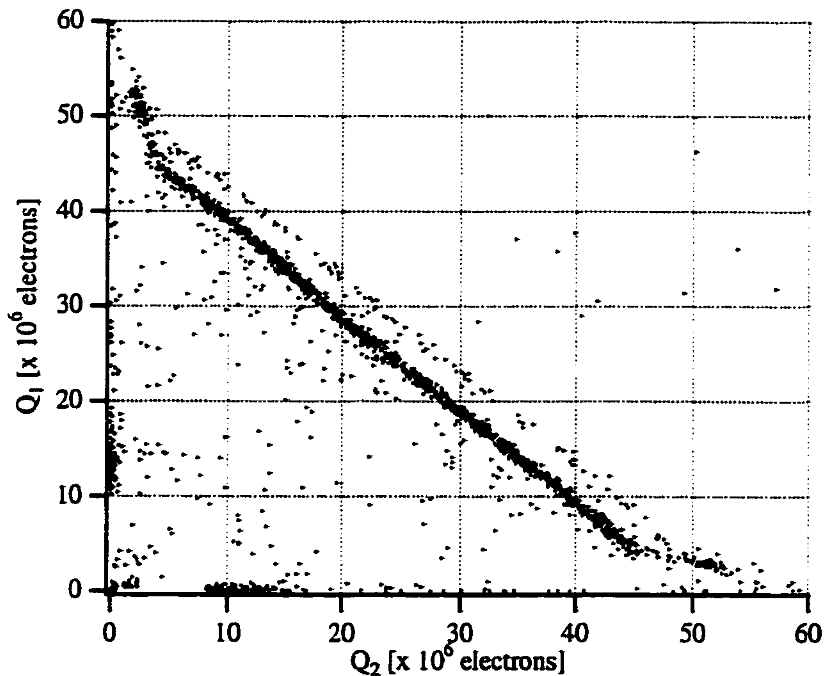

Fig. 4.4.2: Q_1 versus Q_2 for the backtunneling device, F99-14C. (7/9/99)

4.4.2 Backtunneling Device

The major purpose of the backtunneling device is to increase the charge output relative to the electronic noise. The plot of Q_1 versus Q_2 is shown in Fig. 4.4.2. One can see the charge output has increased dramatically, from ≈ 10 million electrons in XN93 to almost 50 million electrons in the backtunneling device. What the plot does not show is that in reality the charge is even larger. The charge has been reduced by over a factor of two from charge division (see section 4.2) due to the low value of quiescent differential resistance (≈ 90 Ω) compared to the amplifier's input resistance. If we assume that the amplifier has R_A = 100 Ω, then the real charge is ≈ 110 million electrons. This is a very

large increase from XN93, more than we had expected, so clearly the Ta wiring has the desired effect. The device also has reasonable energy resolution ($\approx$ 60 eV FWHM) despite the large electronic noise from the high subgap current and the small differential resistance. It is clear that employing backtunneling in future devices is a good idea.

The extreme charge division exhibited in this device precludes a meaningful fit. The low differential resistance affects the charge and the peak current, so the extracted parameters will have little meaning. It is difficult to model the charge division at present without better knowledge of the amplifier and its response, although this will certainly be a topic of future work. From the graph it does appear as if this device, as well as the small junction device, has very little absorber loss. The charge division will have to be accounted for in order to make this statement more strongly. The delay times do indicate a diffusion constant consistent with the other two devices. The outdiffusion time, of course, must be extremely long in order to have the large observed charge increase. This is the major conclusion for this device so far.

• • • • • • •

In short, the new devices look interesting, although more device re-design may still be in order. The backtunneling device gives increased charge, and with fabrication of more devices we should be able to obtain better subgap performance. Such a device may give improved energy resolution (see section 5.6). The small junction device, with its excess self-recombination, may not be as promising. Future junctions should have smaller junction lengths but similar areas, such as to avoid the longer tunnel times which increase the self-recombination. We discuss all the possible improvements in section 5.6.

Chapter 5: Detector Performance

A detector's overall worth is determined by its performance in several key aspects of operation. The most important of these include sensitivity, count rate, quantum efficiency, effective area, energy resolution and spatial resolution. The STJ detector has already been shown to have very good sensitivity and quantum efficiency. The count rate, or dynamic range, is not as good as room temperature detectors, as the low operating temperatures results in long-lived excitations. This, however, is an accepted trade-off; STJs are being applied to low-light level applications where the high dynamic range is not needed. The detector area for STJs has been discussed in chapter 4, as it relates to the intrinsic lifetimes and diffusion times in the superconducting films. At present it is sufficient to say that the active area is good enough for some applications, marginal but improving for x-ray astrophysics.

The remaining questions for the STJ detector, and key to its success as a new technology, are the energy and spatial resolution. The energy resolution has been studied and measured extensively by many groups in the field. It is already good enough at lower photon energies (1-1000 eV) to have started to be used in applications. However, at energies higher than 1 keV, where x-ray astrophysics will benefit, the energy resolution at present is still found to be non-ideal. The spatial resolution has yet to be fully explored by most groups, as work continues mostly on single pixel devices. Our detector has the unique capability to provide intrinsic imaging without the use of multiple pixels. In this chapter, then, we focus on the two main aspects of our detector's performance: the energy and spatial resolution.

5.1 Electronic Noise

The theoretical energy resolution for the STJ detector, discussed in chapter 1, is obtained only in the limit that the electronic readout contributes negligibly to the overall signal fluctuations. Work in our group over the last several years has been heavily concentrated on quantifying and reducing the noise added by the biasing and readout circuits. In the next two sections we will quantify the various components of noise added by the electronics. Despite our overcoming many of the initial problems, the electronic readout is still responsible for the majority of the energy broadening. This is partly related to subtle junction issues which were not realized in past work, most notably the change in the I-V curve during an x-ray pulse (section 4.2). However, it is certainly true that

successful readout of STJ detectors requires the very best in low noise electronic design and components.

First, a word about how the next two sections are arranged. This section, entitled "Electronic Noise", includes noise added by the pulse amplifier to the x-ray signal. We commonly refer to it as the "in-band" electronic noise, because it includes noise at frequencies which are the same as signal frequencies. In the next section, "Bias Voltage Fluctuations", we discuss how low-frequency noise from the amplifier causes the bias voltage to fluctuate from pulse to pulse, which increases the energy width due to the bias dependence of the signal. This is referred to as the "out-of-band" noise, since the low frequency noise is out of the band of typical signal frequencies. Although both components are the result of the electronics, they are in fact qualitatively different.

In this section, then, we quantify the in-band noise. First we will write all noise sources as an equivalent current noise and compare the result to spectral density tests of the noise output. Then we will measure the effect of the current noise on the energy width by injecting current pulses into the amplifier. Finally we will present measurements of the increase in noise from the quiescent state to the dynamic state due to the change in the I-V curve during a pulse.

5.1.1 Current Noise

The circuit design was summarized described in chapter 2. We re-draw the circuit in Fig. 5.1.1 to show the noise components. The junction is represented by an effective resistance R_{eff}, given by the slope of the I-V curve at the bias point. Note that we have eliminated the input capacitance, which would have included the junction, amplifier and lead capacitance. The junction impedance is primarily resistive at signal frequencies so we remove the capacitance in the noise discussion for simplicity. We consider two distinct noise components: parallel current noise ($i_{n,parallel}$), which appears in parallel with the junction, and voltage noise (e_{tot}), which appears in series with the junction and the

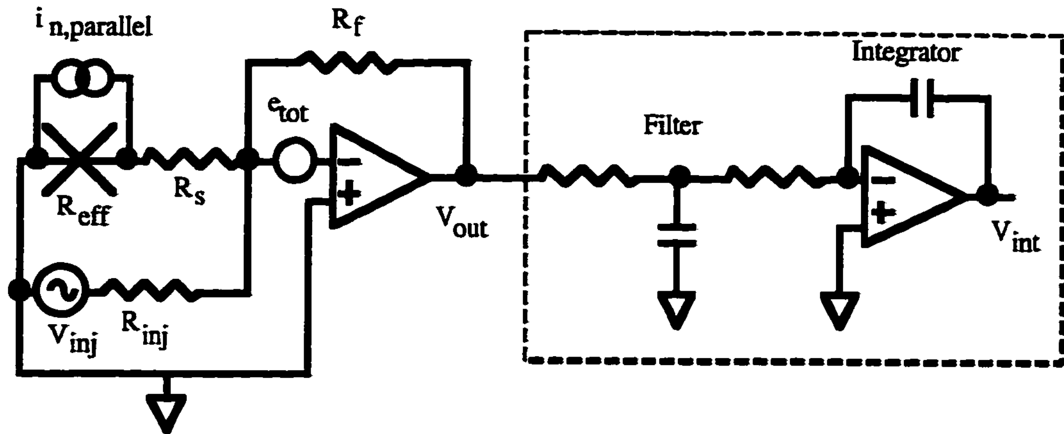

Fig. 5.1.1: Noise schematic of the current amplifier, showing the circuitry for injecting pulses and the post-amplification filtering and integrating.

amplifier. The amplifier is configured in the current sensitive mode, so it is convenient to write all the noise components in terms of an equivalent, total noise current $i_{n,total}$:

$$i_{n,total} = i_{n,parallel} + \frac{e_{tot}}{R_{eff}}. \tag{5.1.1}$$

Note that the voltage noise adds to the total noise current proportional to $1/R_{eff}$.

The parallel current noise comes from two major sources: the Johnson noise of the feedback and injection resistors and the shot noise of the DC bias current. The Johnson current noise is given by the standard formula $\sqrt{(4kT/R)}$. Both the feedback and bias resistor have a value of 1 MΩ and are at room temperature, making each of their noise contribution 0.13 pA/√Hz. The shot noise is given by $\sqrt{(2eI_{dc})}$, and for a bias current I_{dc} = 25 nA has a magnitude of 0.1 pA/√Hz. Other sources of parallel current noise would include the current noise of the FET and nulling loop, but all are too small to be significant.

The voltage noise includes the voltage noise of the FET and the Johnson noise of any lead resistance or extra series resistance. The FET voltage noise is 0.4 nV/√Hz. The lead resistance to the cold stage is small, R_{lead} < 5Ω, and most of it is at cryogenic temperatures making its contribution negligible. Thus the total voltage noise is approximately equal to the voltage noise of the FET: $e_{tot} = e_{FET}$. We have put a variable resistor at room temperature in series with the junction (R_s in Fig. 5.1.1) to add extra voltage noise for diagnostic purposes. The resistance of the junction in the quiescent state is ≈ 20 kΩ; under these quiescent conditions the second term in equation 5.1.1 is negligible. In the dynamic state the resistance is considerably lower (section 4.2), which makes this term larger; we will deal with this later in the section.

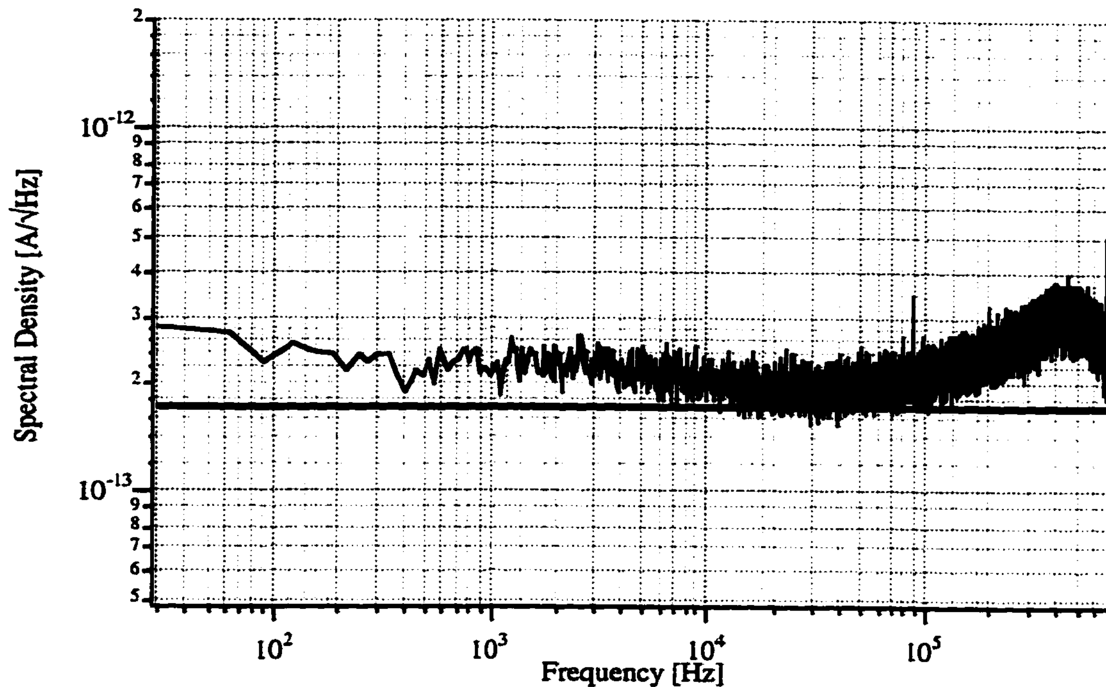

Fig. 5.1.2: Noise spectrum of the junction in quiescent state, with calculated theoretical noise. (3/11/99)

A noise spectrum taken with the junction in the quiescent state is shown in Fig. 5.1.2. The injection resistor was not connected during this test. The noise is white at signal frequencies (≈ 1-100 kHz), with a value ≈ 0.20 pA/√Hz, and starts to increase after that due to the input capacitance and the amplifier peaking (see section 2.3). The amplifier rolls off the noise at high frequency (> 1 MHz). The sum of the noise terms from equation (5.1.2) is shown (solid line), with the significant terms being the Johnson noise of the feedback resistor and the shot noise of the bias current. The sum of the current noise terms agrees reasonably well with the data.

5.1.2 Pulse Injection Tests

Current pulses have been injected into the amplifier with a programmable voltage source through the 1 MΩ injection resistor (see Fig. 5.1.1). The shapes of the pulses are downloaded from the simulation of the current pulse (chapter 3), so they contain approximately the same frequency components. The output pulses are filtered and integrated in the same fashion as the x-ray pulses (see section 5.4) and their "energy width" is measured. The results are shown in Fig. 5.1.3, where we plot energy width (of injected pulses) vs. total current noise in the signal band. The different levels of total current noise are accessible through higher temperatures and trapped flux (see section 2.2). Both effects serve to increase the subgap current and decrease the junction resistance, which increases

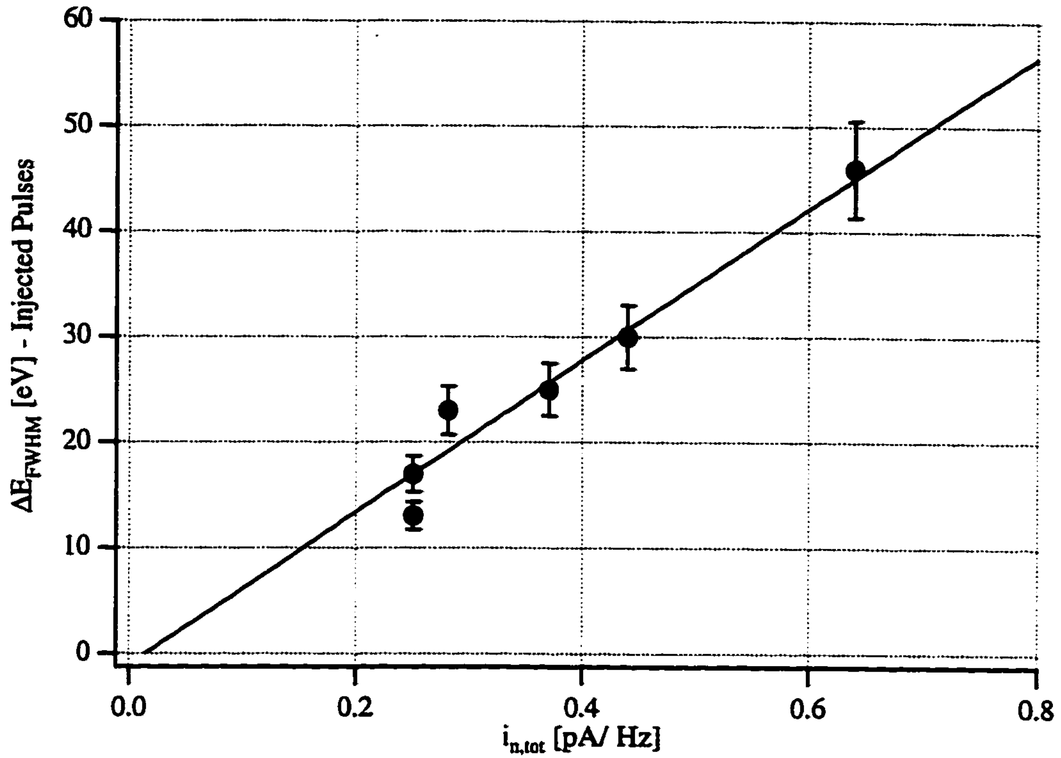

Fig. 5.1.3: Energy width of injected pulses versus total current noise density.

the total current noise (equation (5.1.1)). From the plot we can see that the resolution depends approximately linearly on the total current noise in the signal band. A linear fit to the data has a slope of $m_I = 72$ eV/(pA/√Hz).

The linear dependence is easily understood by looking at the filter and integrator after the current amplifier (Fig. 5.1.1). We draw them as electronic components, although in actuality the filtering and integration are done digitally. The voltage at the output of the current amplifier (V_{out}) is proportional to the total input current. The effect of the filter and the integrator is to multiply the Fourier components of V_{out} by a function of frequency $f(\omega)$: $f(\omega) = 1/(i\omega)$ for the integrator and $f(\omega) = 1/(1+i\omega RC)$ for say a low pass RC filter. As long as the input noise density is white (frequency independent) in the pass-band of the filter, then the fluctuations at the output of the integrator, V_{int}, are still proportional to the fluctuations of V_{out} and the input current noise. The output is also proportional to the total charge; thus the linear dependence is confirmed. The assumption of a white noise density may change in new devices, however, if the pulse frequencies are significantly different.

Using the value of the slope obtained from Fig. 5.1.3, $m_I = 72$ eV/(pA/√Hz), we can conclude that the feedback resistor contributes 0.13 pA/√Hz • m_I = 9.4 eV and the shot noise contributes 0.10 pA/√Hz • m_I = 7.8 eV to the total energy width. During the injection

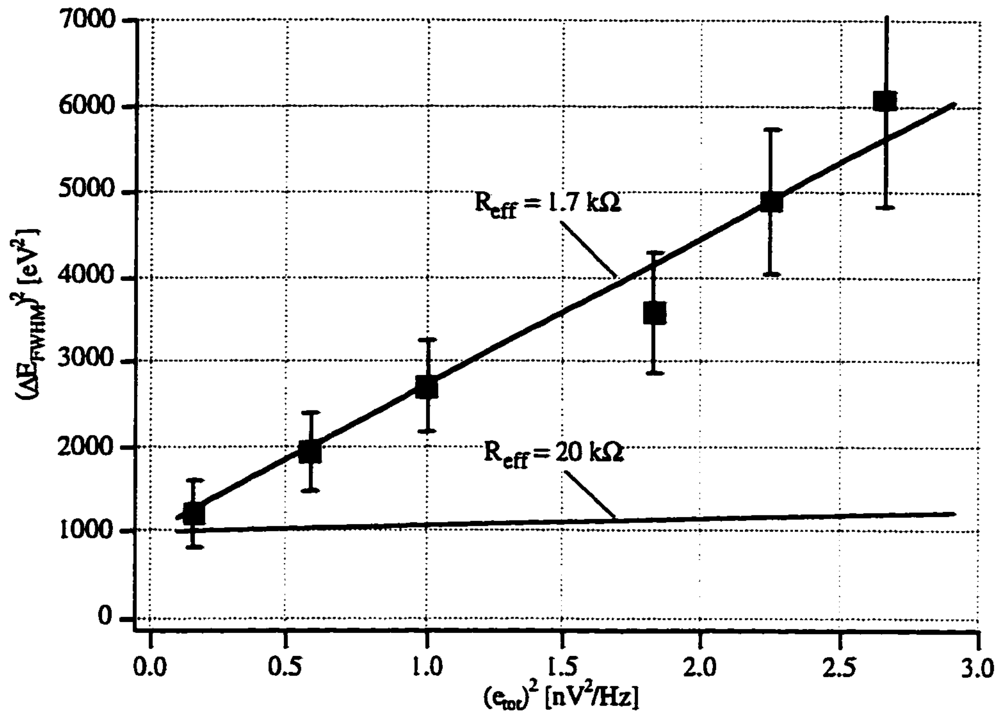

Fig. 5.1.4: Total energy width versus voltage noise. The fit assumes a value of R_{eff} = 1.7 kΩ. (2/26/98)

test we have an additional 9.4 eV from the injection resistor. Adding these sources in quadrature one would expect a width of 15 eV at the lowest value of current noise; that approximately what is observed in Fig. 5.1.3. Note that during the x-ray experiments we do not have the additional 9.4 eV from the injection resistor, as we leave it unconnected.

5.1.3 Noise in the Dynamic State

The above analysis was all done with the junction in the quiescent state, with no x-ray current flowing. The change in the I-V curve (section 4.2) moves the bias voltage to a point of smaller differential resistance during a pulse. This increases the magnitude of the second term in equation (5.1.1), e_{tot}/R_{eff}, thus increasing the overall electronic noise. In order to quantify this effect we have added a variable resistor (R_s) in series with the amplifier. The resistor adds a voltage noise $\sqrt{(4kTR_s)}$ in quadrature with the noise of the FET, e_{FET}, thus increasing the total voltage noise: $e_{tot}^2 = e_{FET}^2 + 4kT/R_s$. This increases the magnitude of the term (e_{tot}/R_{eff}). By measuring the increase in the overall energy width as a function of the total voltage noise, we can estimate the magnitude of R_{eff} during a pulse.

The results are shown in Fig 5.1.4, where we plot total energy width squared (ΔE^2) vs. total voltage noise squared (e_{tot}^2). Note that the energy width plotted before in Fig. 5.1.3 was for *injected pulses*, whereas here it is for pulses due to *x-rays*. The total energy

width does not go to zero at zero voltage noise, due to the noise sources which do not depend on voltage noise. The voltage noise contribution adds in quadrature with all other noise sources, which is why we have plotted energy resolution *squared*. A linear fit to the data has a slope of $(m_V)^2 = [42\ \mathrm{eV}/(\mathrm{nV}/\sqrt{\mathrm{Hz}})]^2$. We will use this number to extract two important quantities: the value of R_{eff} during a pulse, and the excess noise that results.

The value of R_{eff} is calculated by taking the ratio m_I/m_V. The addition of *any* voltage noise e_s adds a current noise e_s/R_{eff}, which from the slope of Fig. 5.1.3 must add an energy width $m_I \bullet e_s/R_{eff}$. This energy width must in turn be equal to $m_V \bullet e_s$, from Fig. 5.1.4. Thus,

$$\begin{aligned} m_I \cdot \frac{e_s}{R_{eff}} &= m_V \cdot e_s; \\ R_{eff} &= \frac{m_I}{m_V}. \end{aligned} \tag{5.1.2}$$

Plugging in the values we find that $R_{eff} = 1.7\ \mathrm{k\Omega}$. This is of course much lower than the value $dV/dI = 15\ \mathrm{k\Omega}$ in the quiescent state, implying that the I-V curve really does change significantly during a pulse. Note that the value of $1.7\ \mathrm{k\Omega}$ is in good agreement with the value found in section 4.2 from the charge division ($1.55\ \mathrm{k\Omega}$). This is a very significant result, one that has been for the most part overlooked by the field thus far.

The noise that results from the lowering of R_{eff} is simply this slope m_V times the voltage noise of the amplifier, 0.4 nV/Hz, since during real x-ray experiments we keep the value of series resistance at zero. This gives an *extra* 16 eV in the dynamic state, which adds in quadrature to the contributions of the shot noise and Johnson noise. Note that the contribution from the reduction in R_{eff} scales with energy, meaning that experiments which look at lower energy photons will not be as affected.

5.2 Bias Voltage Fluctuations

In section 4.2 we saw how the change in the I-V curve during a pulse leads to the integrated charge being voltage dependent at a typical bias point. If the bias voltage is not perfectly constant but rather fluctuates from pulse to pulse, the charge will vary and add uncertainty to the signal. In this section we will quantify the energy width that results from this noise source by measurements of the bias stability. We will then investigate the cause of these bias fluctuations - low frequency noise from the current amplifier. Finally we will present the results for a different biasing circuit, which uses an AC coupled amplifier.

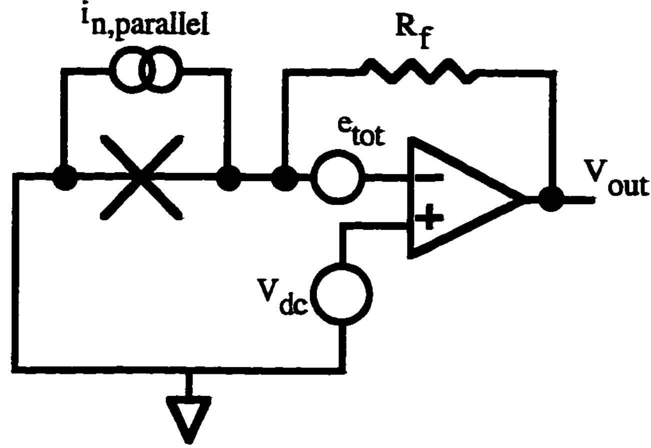

Fig. 5.2.1: Schematic to calculate bias fluctuations.

5.2.1 Energy Width

The energy width that results from bias fluctuations is simply the voltage dependence of the charge (converted to energy) times the rms bias fluctuations (ΔV_{rms}):

$$\Delta E_{biasV} = \left[\frac{E_x}{Q}\cdot\frac{dQ}{dV}\right]\cdot(2.355\Delta V_{rms})\,. \qquad (5.2.1)$$

The first factor is measured from the slope of the Q vs. V curve (section 4.2); we found this to be 30 eV/μV. The second factor is obtained by measurements of the bias stability, which we now describe. The extra factor of 2.355 is to convert rms into FWHM.

In our experiment we DC couple the amplifier to the junction to form an *active* DC voltage bias. This provides a stiff DC load line to help ease requirements on the Josephson current suppression. The drawback, however, is that noise from the amplifier appears on the bias voltage. In Fig. 5.2.1 we re-draw the schematic of the current amplifier, with the injection resistor, series resistor, filter and integrator omitted. We draw in the parallel current noise and the voltage noise and now indicate the bias voltage V_{dc} applied to the non-inverting terminal. Using the ideal op-amp equations and Kirchoff's laws we can write

$$V_{out} = \left(\frac{R_{jct}}{R_f}\right)\left[V_{dc} \pm \left(e_{tot}^2 + i_n^2 R_{in}^2\right)^{1/2}\sqrt{B}\right], \qquad (5.2.2)$$

where V_{out} is the voltage at the output, e_{tot} and i_n are the voltage and current noise densities (here we have dropped the "parallel" from the i_n term for simplicity), and B is the effective bandwidth. The two noises add in quadrature. We will refer to the noise term on the right hand side of equation (5.2.2) as ΔV_{tot}. From the diagram, the voltage across the junction, V_{jct}, is equal to the applied dc bias with a fluctuation given by e_{tot}: $V_{jct} = V_{dc} \pm e_{tot}\sqrt{B}$. From

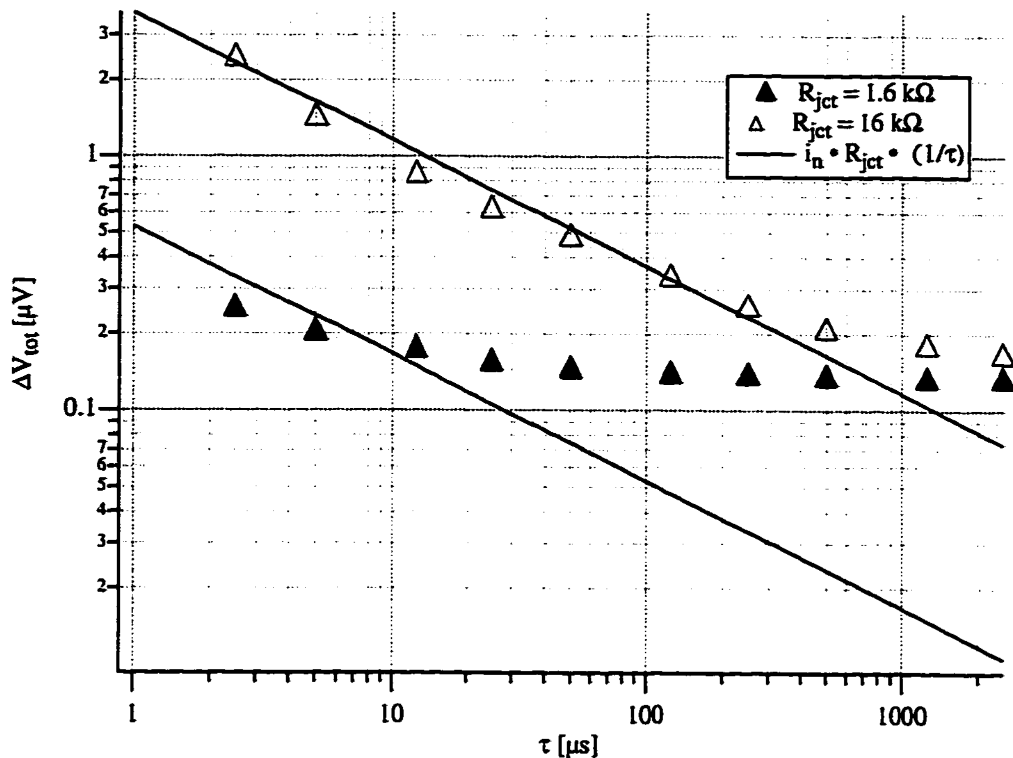

Fig. 5.2.2: Measured bias fluctuations (ΔV_{tot}) referred to the input versus averaging time (τ), for two different junction resistances. The value of ΔV_{tot} at long times gives the rms bias fluctuations. (5/17/99)

equation (5.2.2), a measurement of the fluctuation of V_{out} gives the fluctuation of e_{tot} (and subsequently V_{jct}) *if* $e_{tot} >> i_n R_{in}$. This condition is true at low frequency, below the 1/f knee of the amplifier. In order to measure the stability of V_{jct}, then, we must average V_{out} for long enough times such that the low frequency voltage noise is dominant.

To do the measurement we bias the junction in typical fashion and feed the output of the current amplifier into the oscilloscope. We trigger the scope at a rate of 1 Hz, approximately equal to the arrival rate of the x-rays. Note that this measurement is done without x-rays shining on the detector. We average the voltage at the output (V_{out}) for a time τ, taking several hundred such measurements to get good statistics. The results are shown in Fig. 5.2.2, where we plot ΔV_{tot}, vs. τ. We also plot the quantity $i_n R_{in} \sqrt{B}$, where i_n is measured from the noise spectrum and $B = 1/\tau$. We see that ΔV_{tot} follows the current noise at small values of τ, but as we average for longer the voltage noise eventually dominates. The value of ΔV_{tot} at long times is the value of the rms bias fluctuation (ΔV_{rms}).

In this particular experiment one of the junctions had a small amount of trapped flux, making its resistance smaller. For this junction the voltage noise starts to dominate at

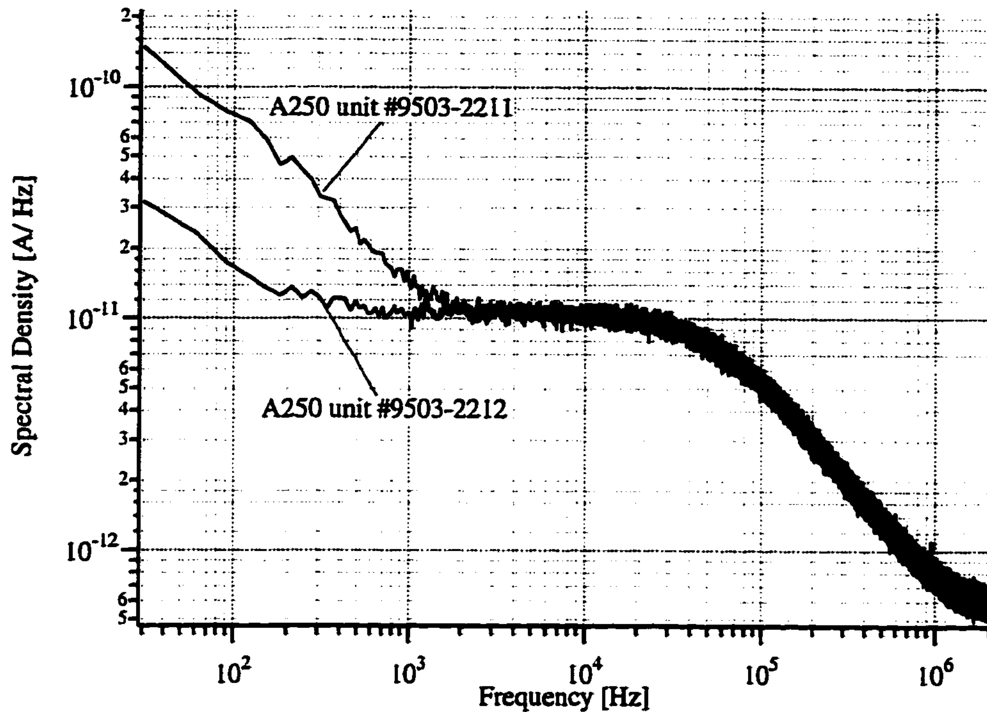

Fig. 5.2.3: Noise spectra of current amplifier with a warm 100 Ω resistor, showing the low frequency noise. The noise is different for different A250 units. (1/27/99)

a smaller value of τ due to the smaller value of R_{in}; however it levels off at the same value of ΔV_{tot} as the higher impedance junction. The same experiment was repeated for a cold 10 kΩ resistor in place of the junction (not shown). All three experiments yielded approximately the same value of ΔV_{rms}: $\Delta V_{rms} = 0.15 \pm 0.03$ μV. The fact that the same result is obtained with three different impedance levels confirms that this is a reasonable measurement, and also shows that the fluctuations are inherently caused by the amplifier. A bias fluctuation of $\Delta V_{rms} = 0.15 \pm 0.03$ μV leads to an energy width $\Delta E_{biasV} = 11 \pm 2$ eV, from equation 5.2.1, using the parameters of the junction studied.

5.2.2 Low Frequency Amplifier Noise

The cause of the bias fluctuations is the low frequency voltage noise from the current amplifier. In Fig. 5.2.3 we show noise spectra of the current amplifier with a warm 100 Ω resistor at the input. The 100 Ω resistor is chosen such that the voltage noise dominates over the parallel current noise. The low frequency noise is indeed significant. The two spectra shown in Fig. 5.2.3 were taken with two different A250 amplifier units, and show significantly different amounts of 1/f noise. This suggests that the A250 is

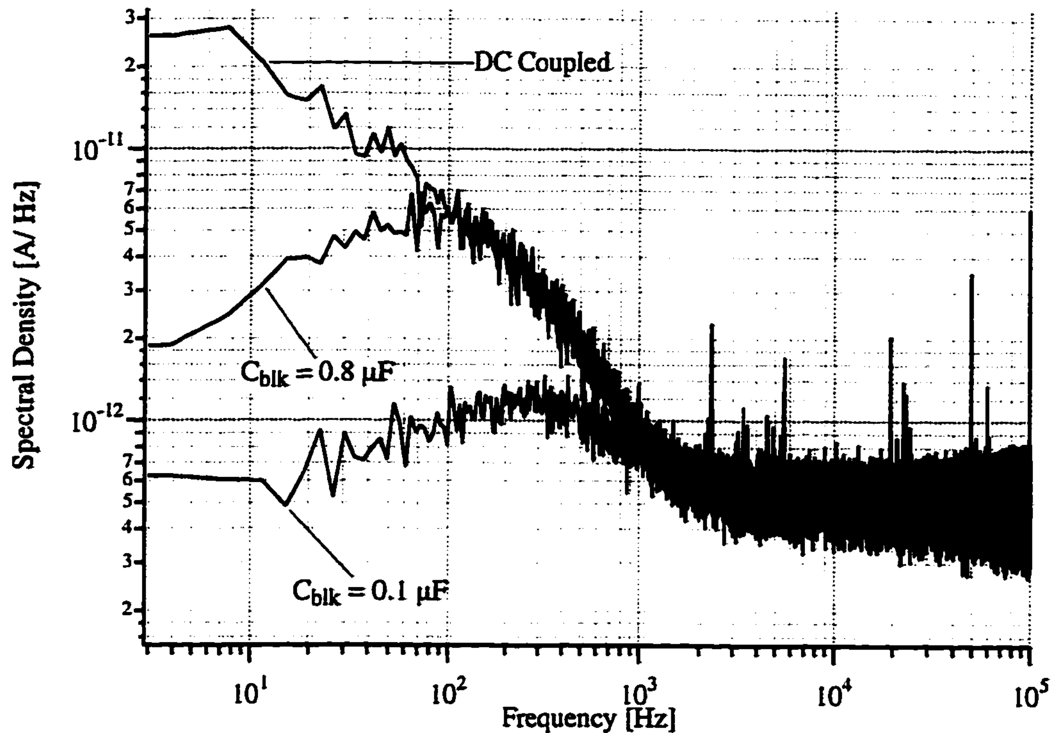

Fig. 5.2.4: Low frequency noise for DC coupling and two different values of blocking capacitor (C_{blk}). Lower values of C_{blk} roll off the noise. (11/9/98)

responsible for the low frequency noise. We often see that the overall energy resolution is better closer to one junction than the other; the different behavior of the A250 units provides a good explanation for this. Work has started in our group to construct a current amplifier using a different transimpedence amplifier than the A250, with less 1/f noise.

Another possible solution for eliminating the low frequency noise is to AC couple the amplifier. In Fig. 5.2.4 we show noise spectra taken with the amplifier AC coupled with a blocking capacitor C_{blk}. Here a cold resistor is used in place of the junction. Smaller values of C_{blk} roll off the noise more, as expected. One could choose C_{blk} small enough such that the energy broadening from bias fluctuations is reduced below the statistical limit for the device. There are two possible drawbacks to such a scheme. First, the blocking capacitor adds extra impedance at signal frequencies in series with the junction; this results in charge division and distorting of the Q_1 vs. Q_2 as we saw in section 4.2. Second, with the AC coupled amplifier one must bias the junction separately with resistors, which does not allow the stiff load line one can achieve with the DC coupled amplifier. The first of these appears to be not a major restriction in our devices; a value of $C_{blk} = 0.1\ \mu F$ gives good reduction of the 1/f noise while not distorting the Q_1 vs. Q_2 too severely. The second drawback, however, is a more serious issue and is discussed at length below.

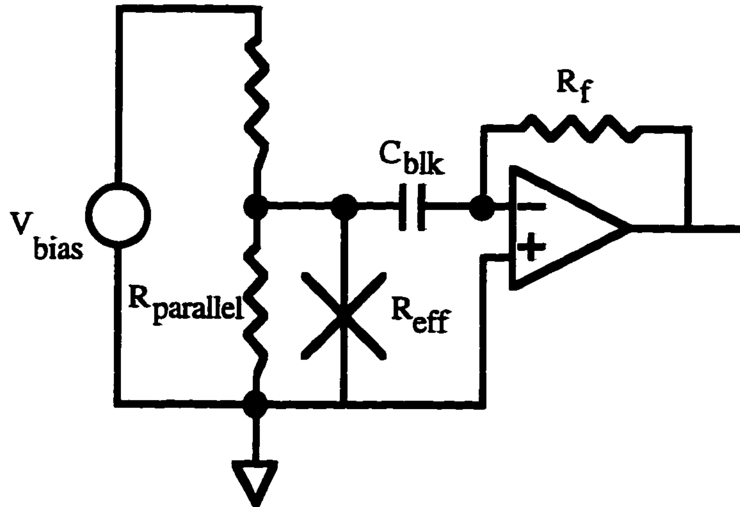

Fig. 5.2.5: Passive voltage bias schematic. The amplifier is AC coupled and the junction is biased with a resistor $R_{parallel}$.

5.2.3 Passive Voltage Bias

One possible biasing scheme with the AC coupled amplifier is what we call Passive Voltage Bias (PVB). The schematic is shown in Fig. 5.2.5. The basic idea is to put a resistor ($R_{parallel}$) in parallel with the junction and bias with a current source. If the magnitude of $R_{parallel}$ is much smaller than the junction resistance, then bias current flows through $R_{parallel}$ and holds a voltage $I_{bias} \bullet R_{parallel}$ across the junction. The blocking capacitor blocks bias currents at DC but allows current to flow through the amplifier at signal frequencies. The value of $R_{parallel}$ must be chosen carefully, however. High values of $R_{parallel}$ result in a shallow load line and biasing instabilities. Low values of $R_{parallel}$ result in a decreased junction impedance: $R_{eff,PVB} = R_{eff} \parallel R_{parallel}$. This magnifies the contribution of the amplifier voltage noise (equation (5.1.1)). In these experiments we used a value of $R_{parallel} = 2$ kΩ, which was found to be a reasonable compromise. The resistor itself was put on the cold stage to reduce its Johnson noise. We also changed the 1 MΩ feedback resistor to 200 kΩ, to reduce the effective amplifier resistance (R_f/A_{0L}) in accordance with the reduced junction impedance.

The total quiescent current noise for the PVB was measured to be 0.45 pA/√Hz, over a factor of two larger than the 0.20 pA/√Hz measured with the active voltage bias (Fig. 5.1.2). The increase was due to the following: (1) the change of the feedback resistor to 200 kΩ, increasing its current noise; (2) the increase of the voltage noise term from e_{tot}/R_{eff} to $e_{tot}/R_{eff,PVB}$ due to the addition of the 2 kΩ in parallel with R_{eff}; (3) the current noise of $R_{parallel}$, which even on the helium bath at T = 1.5 K is still not negligible. Plugging in the magnitude of these noise terms gives a calculated total current noise of 0.43

pA/√hz, in good agreement with the measurement. This is for the quiescent state. In the dynamic state the reduction of $R_{eff,PVB}$ adds additional noise, as it did for the active voltage bias. We did not do the direct "measurement" of R_{eff} as for the active voltage bias case; however, one would assume that the value of R_{eff} during a pulse is independent of the biasing. If this is the case then the R_{eff} is the 1.7 kΩ measured previously. The new value of $R_{eff,PVB}$ = 1.7 kΩ ∥ 2 kΩ is then 1.1 kΩ. This adds an additional (0.4 nV/√Hz) / (1.1 kΩ) = 0.36 pA/√Hz during a pulse. Using the conversion factor of 72 eV/(pA/√Hz) found in the previous section, we find then that the calculated electronic noise should be 31 eV in the quiescent state and an additional 26 eV during a pulse. The statistical noise and the bias fluctuations are small compared to these, so the total calculated noise is $((31\text{ eV})^2 + (26\text{ eV})^2)^{1/2} = 40$ eV.

The detector was exposed to x-rays and the energy resolution was measured. The filtering, integration and location extraction are similar to other x-ray experiments (described in section 5.4). The best results obtained were for a 13 μm range, where the FWHM energy resolution was found to be 58 eV. This does not agree with the calculated noise of 40 eV, indicating that there is probably an unknown source of excess noise in this biasing circuit. We speculate that perhaps the shallow load line, 2 kΩ in this case, plays a role in determining the energy resolution. To bias stably with a shallow load line places more demand on the Josephson current suppression. If the suppression is not ideal, switching events may result and add noise to the signal. Other groups [Friedrich, 1998] have found an improvement in the electronic noise after changing from current bias (shallow load line) to voltage bias (stiff load line), with other parameters held constant. Future experiments will hopefully shed more light on this issue.

5.3 Statistical Noise

In chapter 1 we saw how the ultimate limit for the energy resolution of an STJ detector is set by the statistics of the initial quasiparticle creation. After the quasiparticles are generated, however, they must still diffuse through the absorber, be trapped in the junctions, and tunnel through the barrier in order to register as a collected charge by the amplifier. The statistical limit is obtained only if each and every quasiparticle tunnels *exactly* once. In a real, practical device this is very difficult to achieve because of various gain and loss mechanisms inside the detector. These mechanisms have statistical fluctuation from one photon to the next, thus adding uncertainty to the signal charge. The noise that results is commonly referred to as statistical noise. In this section we will

investigate the various components of statistical noise and their contribution to the energy resolution.

5.3.1 Gain/Loss Mechanisms

We consider five major processes that result in the gain or loss of signal charge:

(1) Quasiparticle creation: The average number of quasiparticles created by a photon, N_0, is equal to the photon energy, E_x, divided by ε, the energy required to create a single charge. This was discussed in chapter 1.

(2) Absorber loss: Generated quasiparticles can be lost in the absorber on route to the junction by recombination with other quasiparticles. We define $\beta = N_{lost}/N_0$, where N_{lost} is the number of quasiparticles that recombine out of a possible N_0. The resulting average number of quasiparticles after loss is then $(1 - \beta) N_0$.

(3) Trapping multiplication: Quasiparticles that are injected into the Al junction from the Ta absorber can emit a phonon of energy $E_{phonon} > 2\Delta_{Al}$, which can break a Cooper pair in the Al junction and create two more quasiparticles. We define $\alpha = (1 + 2N_{mult}/N_0)$, where N_{mult} is the number of quasiparticles that emit a 2Δ phonon which breaks a pair. The resulting average number of quasiparticles after multiplication is then αN_0.

(4) Backtunneling: Each quasiparticle can tunnel multiple times and increase the collected charge. If each of the N_0 quasiparticle tunnels on average $\bar{n}$ times, the total charge will be $(e\bar{n}) N_0$.

(5) Cancellation: Quasiparticles which are at an energy of eV_{dc} or higher above the gap in their respective electrode can undergo a tunneling process which transfers a charge in the reverse direction, subtracting a charge e from the total signal (see section 3.3). We define $\gamma = N_{rev}/(\bar{n}N_0)$, where N_{rev} is the number of tunneling events that transfer charge in the reverse direction out of a total of $\bar{n}N_0$ tunneling events. The total charge after cancellation is $(1 - 2\gamma)(e\bar{n}) N_0$. The factor of two reflects the fact that a forward tunneling event gives

a charge of +1 while a reverse tunneling event gives a charge of −1, the difference between them being a charge of −2. We will explore the implications of this later.

5.3.2 Energy Width

We can now write the total, net charge as the charge of the electron times the net number of tunneling events: $Q_{net} = eN_{net}$. N_{net} is given by the product of all the gain and loss mechanisms listed above:

$$N_{net} = \alpha\,(1-\beta)\,(1-2\gamma)\,\bar{n}\,N_0. \tag{5.3.1}$$

The energy broadening that results from the statistical fluctuation of all these mechanisms is calculated from the standard deviation of N_{net}:

$$\Delta E_{statistics} = 2.355 \cdot E_X \frac{\sigma_{N_{net}}}{N_{net}}. \tag{5.3.2}$$

To calculate $\sigma_{N_{net}}$ we use the propagation of errors formula [Bevington, 1992]. If X = f(U,V,W...) where U,V,W.. are all independent (i.e. the covariance terms are zero) then we can write

$$\sigma_X^2 = \sigma_U^2\left(\frac{\partial X}{\partial U}\right)^2 + \sigma_V^2\left(\frac{\partial X}{\partial V}\right)^2 + \sigma_W^2\left(\frac{\partial X}{\partial W}\right)^2 + ... \tag{5.3.3}$$

Assuming all the gain/loss mechanisms are independent, we apply (5.3.3) to (5.3.1) :

$$\frac{\sigma_{N_{net}}}{N_{net}} = \left[\frac{\sigma_{N_0}^2}{N_0^2} + \frac{\sigma_\beta^2}{(1-\beta)^2} + \frac{\sigma_\alpha^2}{\alpha^2} + \frac{\sigma_{\bar{n}}^2}{\bar{n}^2} + \frac{4\sigma_\gamma^2}{(1-2\gamma)^2}\right]^{1/2}. \tag{5.3.4}$$

In order to calculate $\Delta E_{statistics}$, then, we need to calculate the standard deviation from all the mechanisms: σ_{N_0}, σ_β, σ_α, $\sigma_{\bar{n}}$, σ_γ. We do this below.

(1) Creation: The fluctuation in the number of quasiparticles created is given by

$$\sigma_{N_0}^2 = FN_0 \qquad . \tag{5.3.5}$$

where F is the Fano factor. This was discussed in chapter 1. The value of F is calculated from Monte Carlo simulations of the quasiparticle generation processes [Kurakado, 1982], and is found to be ≈ 0.2 for absorption in niobium and tin. Tantalum should be similar to these materials, so we will assume F = 0.2 for our devices.

(2) Absorber loss: The number of quasiparticles lost in the absorber, N_{lost}, are chosen randomly from the initial N_0 quasiparticles. We define p = (probability that a quasiparticle

is lost) = $N_{lost}/N_0 = \beta$ and q = (probability a quasiparticle is not lost) = $1 - p = 1 - \beta$. The probability distribution for N_{lost} is binomial, so $\sigma^2_{N_{lost}} = N_0 pq$ [Reif, 1965]. From the relation $\beta = N_{lost}/N_0$ we can also write $\sigma^2_\beta = \frac{1}{N_0^2}\sigma^2_{N_{lost}}$. Thus,

$$\sigma^2_\beta = \frac{1}{N_0}\beta(1-\beta). \tag{5.3.6}$$

For our devices the loss near the edge of the absorber is approximately 12 % (section 4.1), so $\beta = 0.12$.

(3) Trapping Multiplication: The number of quasiparticles that emit a pairbreaking phonon, N_{mult}, are chosen randomly from the initial N_0. We define p = (probability that a quasiparticle multiplies) = $(\alpha - 1)/2$ and q = (probability a quasiparticle does not multiply) = $1 - p = (3 - \alpha)/2$. As in the case for simple loss we use the binomial distribution, so $\sigma^2_{N_{mult}} = N_0 pq$. We write $\sigma^2_\alpha = \frac{4}{N_0^2}\sigma^2_{N_{mult}}$ from $\alpha = (1 + 2N_{mult}/N_0)$; thus

$$\sigma^2_\alpha = \frac{1}{N_0}(\alpha-1)(3-\alpha) \tag{5.3.7}$$

In section 4.1 we found a trapping multiplication of $\alpha = 1.6$ in our devices.

(4) Backtunneling: We assume that each quasiparticle has a probability P_1 to tunnel from the trap and P_2 to tunnel from the counterelectrode. We define n to be the number of times that a quasiparticle tunnels; the mean and variance of n have been calculated by Goldie, et al. [Goldie, 1994] and are given by:

$$\bar{n} = \frac{P_1(1+P_2)}{(1-P_1P_2)}$$

$$\sigma^2_n = \frac{P_1 - P_1^2 + 3P_1P_2 + P_1^2P_2}{(1-P_1P_2)^2}. \tag{5.3.8}$$

Each photon produces (on average) N_0 quasiparticles that each tunnel n times; thus the total number of tunneling events *per photon* is $(n_1 + n_2 + n_3 + \ldots n_{N_0}) = \bar{n}N_0$. We want the variance of $\bar{n}$, not of n, so we use

$$\sigma_{\bar{n}}^2 = \frac{\sigma_n^2}{N_0}. \qquad (5.3.9)$$

Goldie, et. al. define a factor G, where $G = \frac{\sigma_n^2}{\bar{n}^2}$. Therefore we can write,

$$\sigma_{\bar{n}}^2 = \frac{1}{N_0}\bar{n}^2 G. \qquad (5.3.10)$$

In our devices $\bar{n} = 2.5$ and $G = 0.84$.

(5) Cancellation: The number of tunneling events that transfer a charge against the bias, N_{rev}, are chosen randomly from the total of $\bar{n}N_0$ tunneling events. We define p = (probability to transfer charge in the reverse direction) = $N_{rev}/(\bar{n}N_0)$ = γ and q = (probability to transfer charge in the forward direction) = $1 - p = 1 - \gamma$. Similar to the case of absorber loss we have $\sigma_{N_{rev}}^2 = (\bar{n}N_0)pq$, and $\sigma_\gamma^2 = \frac{1}{(\bar{n}N_0)^2}\sigma_{N_{rev}}^2$; thus,

$$\sigma_\gamma^2 = \frac{1}{\bar{n}N_0}\gamma(1-\gamma) \qquad (5.3.11)$$

In our devices approximately 15% of the tunneling events transfer charge against the bias ($\gamma = 0.15$).

Having solved for the standard deviation of all the various gain/loss mechanisms, we can now substitute into equation (5.3.4) and equation (5.3.2) to find the total energy width due to statistical noise:

$$\Delta E_{statistics} = 2.35 \cdot \left[F + \frac{\beta}{(1-\beta)} + \frac{(\alpha-1)(3-\alpha)}{\alpha^2} + G + \frac{4\gamma(1-\gamma)}{\bar{n}(1-2\gamma)^2} \right]^{1/2} (\varepsilon E_x)^{1/2} \qquad (5.3.12)$$

We can see the form is very similar to that of just the creation noise, $\Delta E_{creation} = (F\varepsilon E_x)^{1/2}$, except that each gain mechanisms adds its own "effective Fano Factor" (F_{eff}) to the original Fano factor F. We summarize this in the table below, along with the values for the XN93 device. The energy width for each process alone is given in parenthesis.

Process	Gain/Loss	F_{eff} Expression	XX93 value	F_{eff} Value
Creation	N_0	F	$F = 0.2$	0.2 (2.8 eV)
Absorber Loss	$(1-\beta)$	$\frac{\beta}{(1-\beta)}$	$\beta = 0.12$	0.14 (2.3 eV)
Trapping Multiplication	α	$\frac{(\alpha-1)(3-\alpha)}{\alpha^2}$	$\alpha = 1.6$	0.33 (3.6 eV)
Backtunneling	$\bar{n}$	G	$G = 0.84$	0.84 (5.2 eV)
Cancellation	$(1-2\gamma)$	$\frac{4\gamma(1-\gamma)}{\bar{n}(1-2\gamma)^2}$	$\gamma = 0.15$, $\bar{n}=2.5$	0.42 (2.6 eV)

Table 5.1: Statistical noise for the different signal gain processes.

Plugging in the values from the table, we find that $\Delta E_{statistics} = 8.7$ eV. This is over a factor of three larger than just the creation noise alone, indicating that the gain/loss mechanisms are responsible for the majority of the statistical broadening. Note that with the exception of cancellation, we have not "cascaded" the noise sources, i.e. included the change in signal from one mechanism to the next. For example, in calculating the F_{eff} for trapping multiplication we assumed that the number of quasiparticles that multiply are chosen out of the initial N_0 quasiparticles. If there is loss in the absorber before the trapping takes place, there will be not N_0 quasiparticles but rather $(1-\beta)\, N_0$. This will multiply the effective Fano factor for trapping by a factor of $1/(1-\beta)$. Fig. 5.3.1 shows a block diagram for the signal charge, with the gain factor for each mechanism. To cascade two or more of the statistical noises, one simply multiplies the effective Fano factor for a given mechanism by 1/(gain of previous stages). The cascading is most significant for cancellation since the gain from backtunneling can be very large (other groups have seen $\bar{n} = 100$ or higher). In our devices it is the only mechanism where the cascading is numerically significant; that is why we have written the F_{eff} for cancellation including the backtunneling gain.

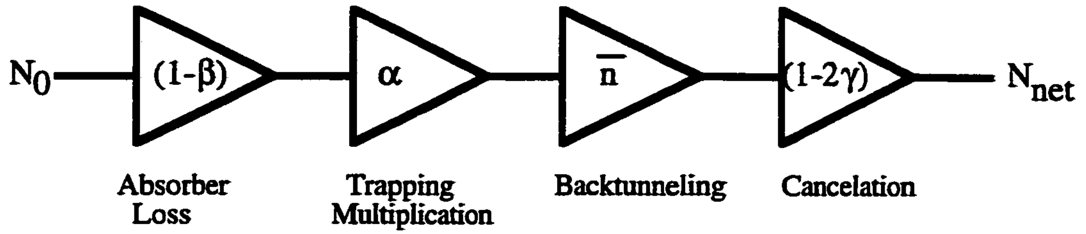

Fig. 5.3.1: Cascading of statistical noises. The noise for each process should be thought of as appearing at the input of each stage.

5.3.3 Loss, Trapping, and Cancellation

The statistical fluctuation for creation and backtunneling have been well known in the field for some years. The fluctuations for trapping and loss have been known to exist, but have not been calculated previously; the fluctuation for cancellation has neither been recognized nor calculated before. Therefore before we end the discussion in this section we will touch on these last few mechanisms briefly.

In Fig. 5.3.2 we plot the energy width for trapping and creation alone versus the trapping multiplication factor α. We see that if none of the quasiparticles multiply or if all of them multiply we recover the initial Fano noise. The case is worst around $\alpha = 1.4$, which is close to the value for our devices. However, relatively speaking this is not a particularly large noise source. A resolution of 5 eV instead of 3 eV is a small price to pay for the strong trapping in our devices, which allows for effective charge division and imaging.

The cancellation noise, however, can in some cases be a much more significant. In Fig. 5.3.3 we plot the energy width for cancellation and absorber loss plus creation verses the net signal gain (Q_{net}/Q_{tot}). The difference between the two processes is the extra factor of two mentioned previously. For a quasiparticle lost in the absorber, the overall signal changes by -1: the quasiparticle adds a charge of +1 if it is not lost, 0 if it is lost. For cancellation, the signal changes by –2: the tunneling event adds a charge of +1 if it is in the forward direction, -1 if it is in the reverse direction. This factor of two makes the cancellation more noisy for the same reduction in signal. It is clear from the graph that in order to obtain resolution close to the Fano limit, it is necessary to collect > 95% of the charge.

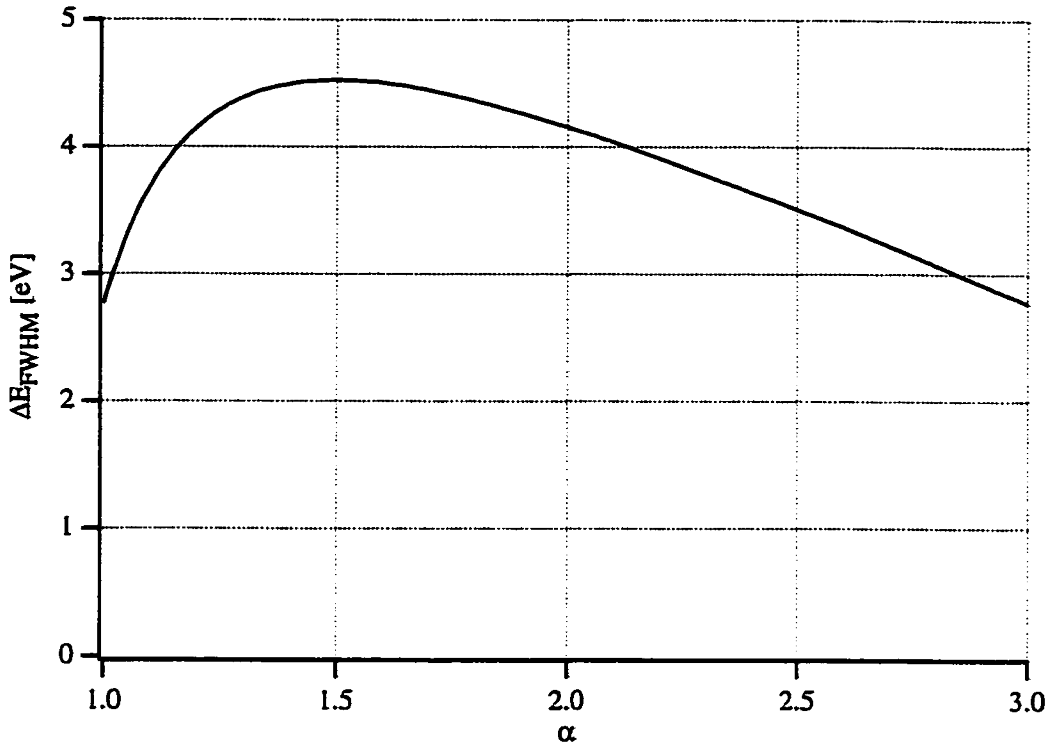

Fig. 5.3.2: Statistical trapping noise plus creation noise versus multiplication factor α. When $\alpha = 1$ the pure Fano limit is reached.

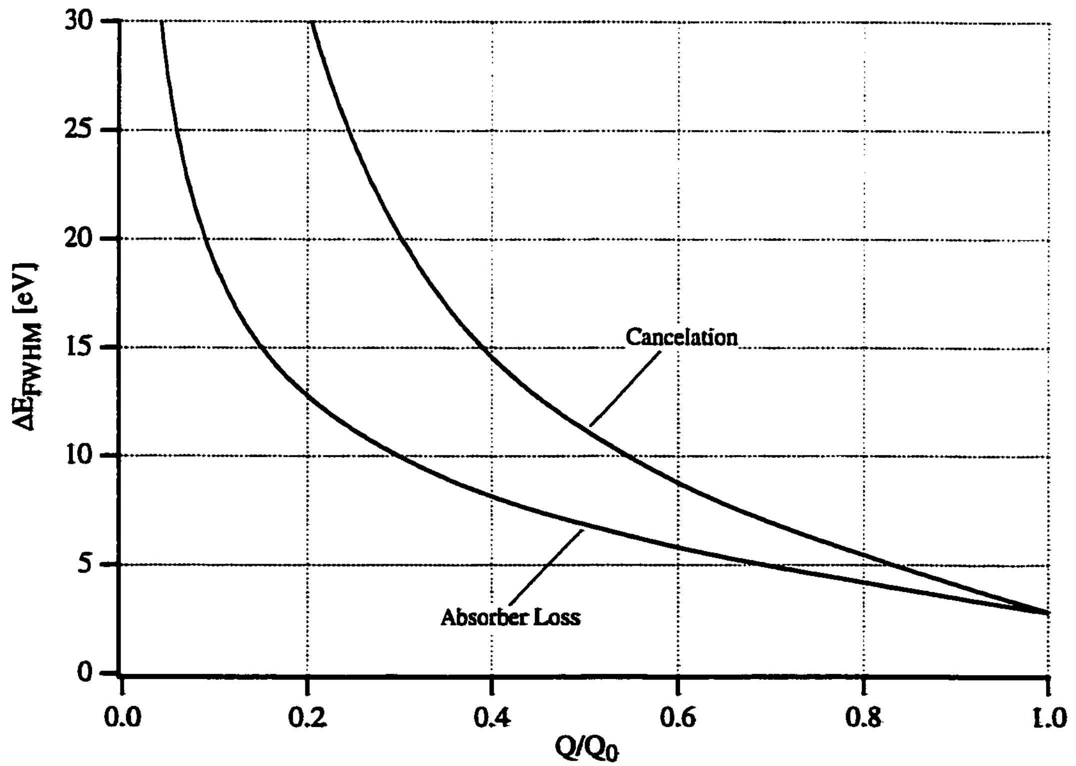

Fig. 5.3.3: Statistical noise from absorber loss and cancellation (both plus creation) versus signal gain.

5.4 Energy Resolution

In the previous three sections we have discussed various noise sources which contribute to the detector's energy resolution. We are now ready to present the measured energy resolution and compare its magnitude to the noise sources that we have identified. First we will describe the digital processing of the pulse waveforms that leads to the extraction of the photon energy and location for each pulse. Next we will present the best histograms and compare the FWHM energy resolution to the results from the previous three sections. We will find good agreement between the measured resolution and the sum of the sources we have already identified. Finally we will comment on some additional noise sources that were omitted from the discussion of sections 5.1-5.3. In the last section of this chapter (section 5.6), we will discuss possible improvements to reduce the known noise sources; these should help bring the energy resolution near the limit predicted by Fano statistics.

5.4.1 Pulse Waveform Processing

The pulses from the current amplifier are fed to an oscilloscope, where they are digitized and then sent to a computer to be recorded on disk. We use the unfiltered data to extract the relevant physical parameters that were discussed in chapter 4. We can then apply digital filters to the pulses to filter out the electronic noise and obtain the best resolution. Because we save the entire waveform of each pulse, we can try many different filters on the same data to optimize the resolution. We use Bessel, Butterworth and Chebyshev filters [Horowitz,1989], with typical lower cutoff frequencies of $\approx$ 1-7 kHz and upper cutoff frequencies of $\approx$ 30-70 kHz. These frequencies agree roughly with the spectral components of the signal and typically give the best energy width. After applying the filters we integrate each pulse numerically to obtain the total charge. Fig. 5.4.1 shows a typical plot of Q_1 vs. Q_2 after filtering. Notice that the total charge has been reduced from that of the plots shown in chapter 4 (for example, Fig. 4.3.3), but that the signal-to-noise ratio has improved.

The filtering and integration yield a pair of charges (Q_1,Q_2) for each photon. We then use the formulas from Kraus [Kraus, 1989] to correct for the absorber losses and extract the photon's energy and location (E,x_0):

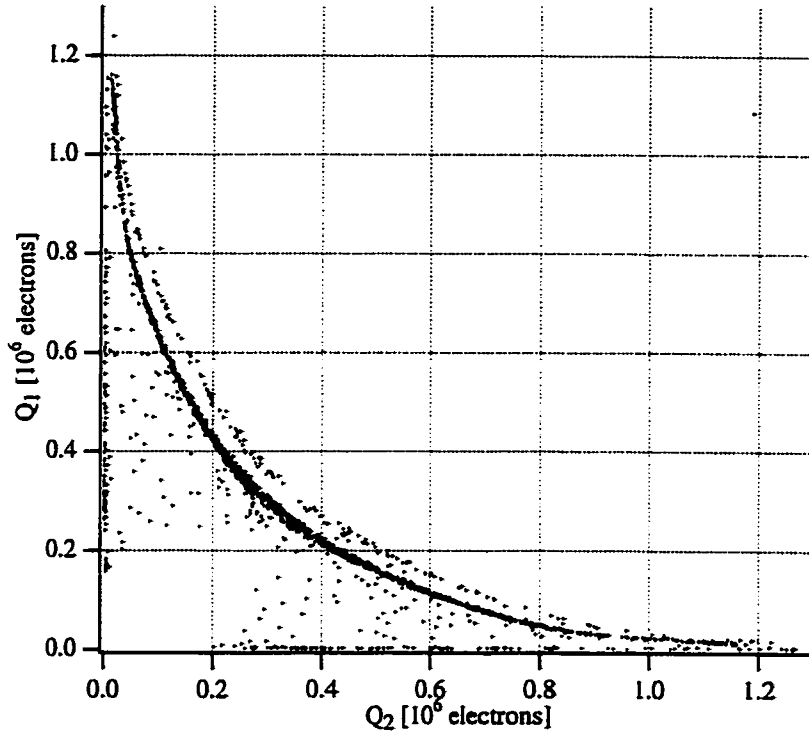

Fig. 5.4.1: Q_1 versus Q_2 after filtering. The filtering reduces the signal, but improves the signal to noise ratio. (1/11/99)

$$Q_{tot} = \sqrt{Q_1^2 + Q_2^2 + 2Q_1Q_2\cosh(\alpha_L)}$$
$$E = \frac{Q_{tot}}{\omega} \qquad (5.4.1)$$
$$x_0 = \frac{L}{2\alpha_L}\ln\left(\frac{Q_1 e^{-\alpha_L/2} + Q_2 e^{\alpha_L/2}}{Q_1 e^{\alpha_L/2} + Q_2 e^{-\alpha_L/2}}\right).$$

Here α_L is a loss parameter and is equal to $L_{abs}/\sqrt{(D\tau_{loss})}$. Q_{tot} is the sum of the charges after correcting for loss, and ω is the conversion of energy to charge. In Fig. 5.4.2 we plot Q_{tot} vs. x_0 for the data of Fig. 5.4.1. We note stronger K_α line at Q_{tot} = 1.5 million electrons and the weaker K_β line at 1.6 million electrons. Notice that total charge Q_{tot} increases approximately 10-15 μm from each end. This is because the Al junctions overlap the Ta absorber in these regions and the average value of the energy gap is smaller, resulting in more created charge. The value of α_L is fit by the computer, constrained to the

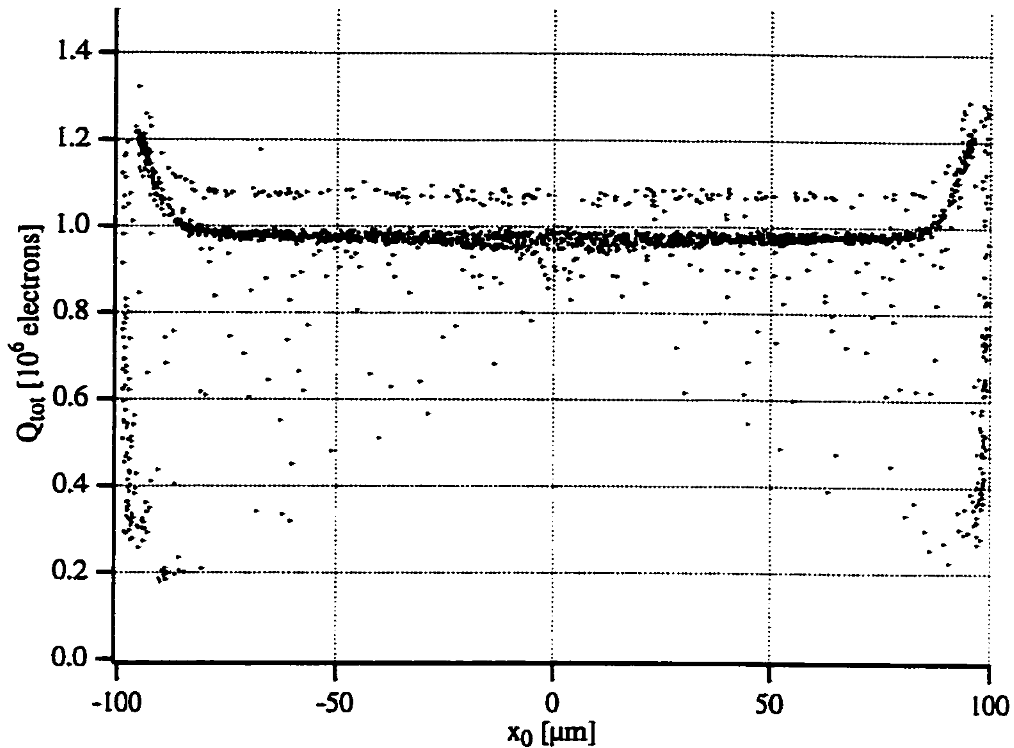

Fig. 5.4.2: Q_{tot} versus x_0 after correcting for absorber losses. The charge increases approximately 10-15 μm from either edge due to the overlap of the aluminum trap. (1/11/99).

value that best takes the total charge Q_{tot} onto a straight line. Note that a single value of α_L fits the whole absorber, other than the end regimes.

5.4.2 Energy Resolution

In Fig. 5.4.2 we can see that the fluctuation of charge is stronger in the center of the absorber than near the edges. We will see later in the section that this is due to the Nb contact to the Ta absorber, which is located in the center of the device. One advantage of having spatial resolution is that we can throw away events near the center and look at the energy width near the edges, where the resolution is better. Of course, in a practical detector one would ideally want the same resolution over the whole absorber, so the extra broadening in the center does need to be addressed. However, for purposes of studying the energy resolution we can for now focus on events near the edges. In Fig. 5.4.3 we show two location cuts, one on each side of the absorber, from two different cryogenic runs. The cut on the right side is over the range +67 μm to +85 μm and was taken on 2/26/98; the one on the left side is from –69 μm to –83 μm, taken on 3/10/99. The data have been filtered with different filters, so their charges Q_{tot} are not equal. The best filter

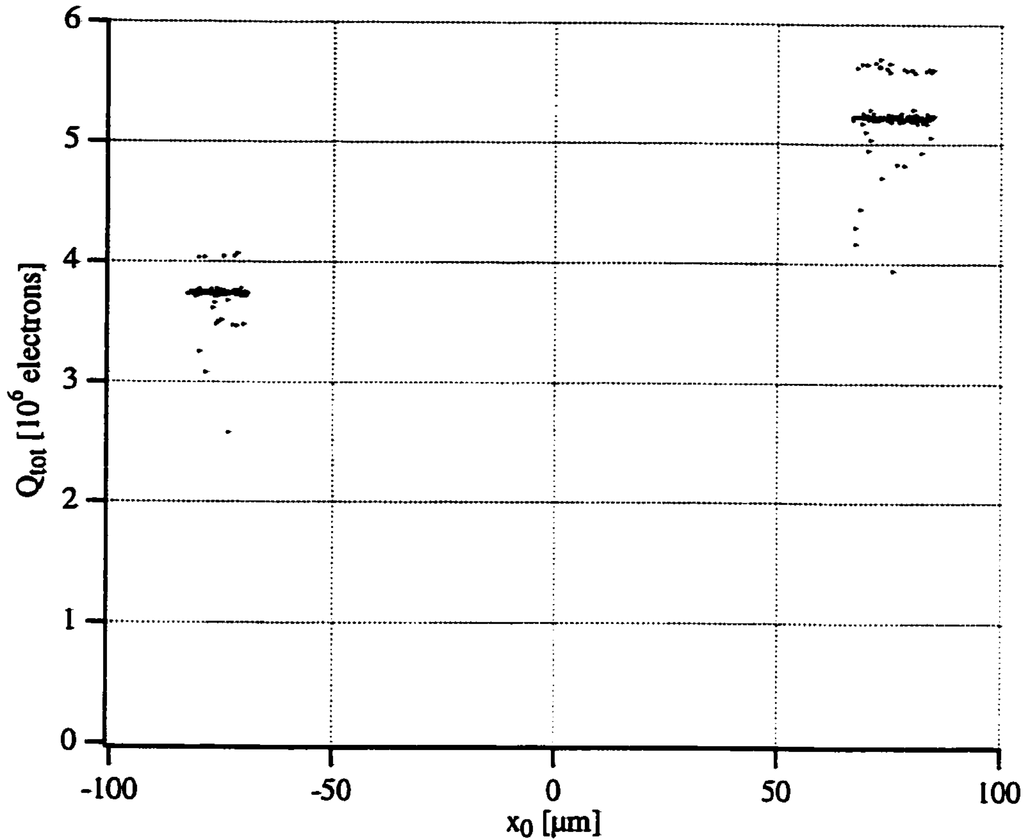

Fig. 5.4.3: Total charge after filtering versus absorption location for two different cryogenic runs (2/26/98 on right, 3/10/99 on left). The charge is different because a different filter optimizes each set of data.

for each run is found by a "filter search": the computer applies a filter, fits the value of α_L, extracts the energy/location, performs the location cut and finds the energy resolution; the process is then repeated for many different filters and the best one is chosen.

The histograms for each location cut are shown in Fig. 5.4.4. We fit each histogram with a double Gaussian function representing the $K_{\alpha 1}$ and $K_{\alpha 2}$ lines, constrained to the ratio [Verhove, 1998] of the peaks and energies ($K_{\alpha 1}$ = 5898.73 eV, relative strength = 100; $K_{\alpha 2}$ = 5887.65 eV, relative strength = 51). The best fit has a FWHM energy resolution of 25.4 ± 2.1 eV for the 2/26/98 data and 26.1 ± 3.6 eV for the 3/10/99 data. We show the fits in Fig. 5.4.4. The location cuts reduce the number of points in the histogram to ≈ 120. This can result in artificially low/high resolution depending on the choice of binning when the histogram is made. We have treated this problem by choosing 100 different possible bin sizes for each data set; the numbers reported here are the average and standard deviation of all 100 resolutions for each device.

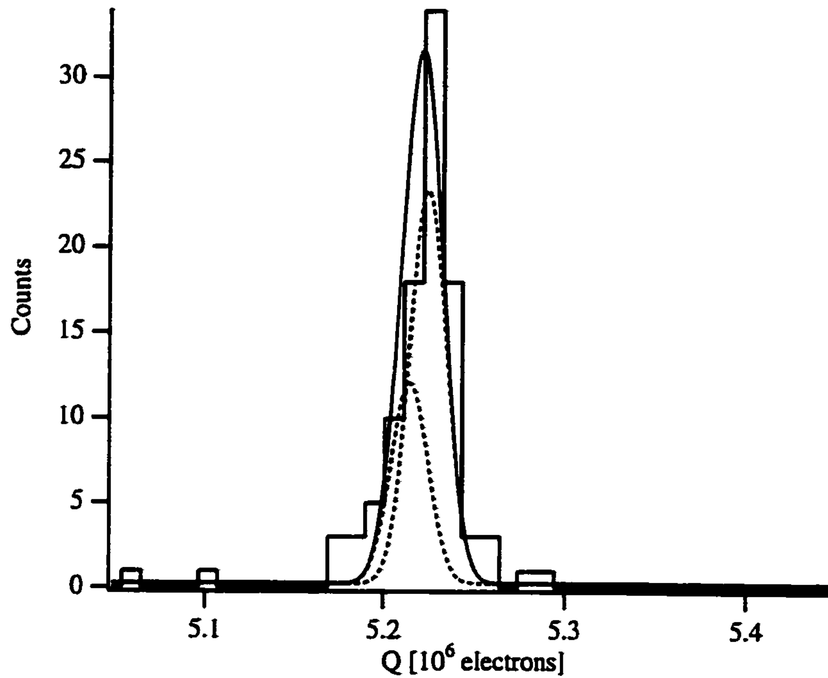

Fig. 5.4.4a: Charge histogram from data of 2/26/98. The resolution is 25.4 eV FWHM. Dotted lines show the two lines $K_{\alpha 1}$ and $K_{\alpha 2}$.

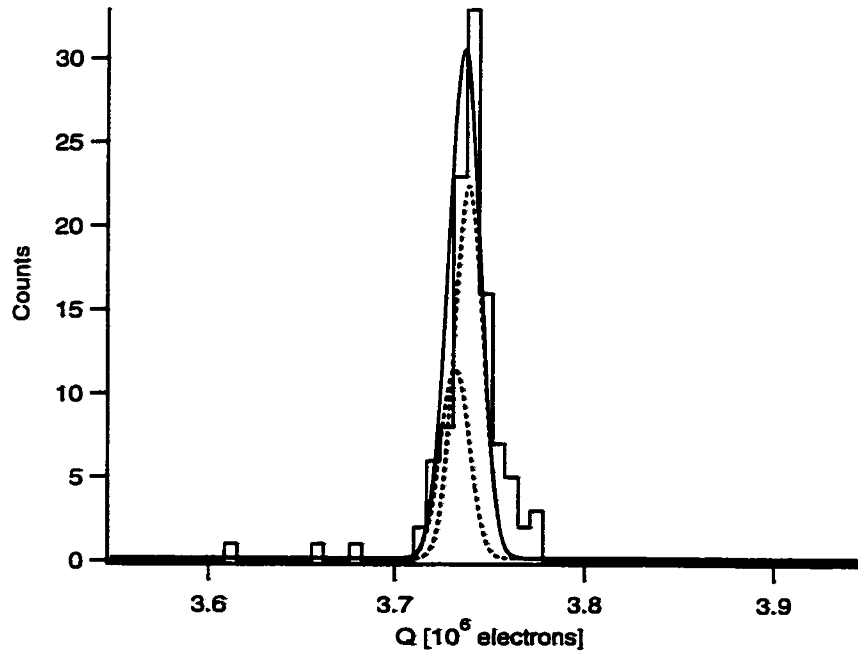

Fig. 5.4.4b: Charge histogram from data of 3/10/99. The resolution is 26.1 eV FWHM.

In table 5.2 below we show the predicted energy widths for the noise sources that we have discussed so far, and then compare with the resolution from Fig. 5.4.4:

Noise Source	FWHM value
Statistical (section 5.3)	$(8.7\ eV)^2$
Shot Noise, DC current (5.1)	$(7.2\ eV)^2$
Johnson Noise, R_f (5.1)	$(9.4\ eV)^2$
Voltage noise/R_{eff} (5.1)	$(16\ eV)^2$
Bias Fluctuations (5.2)	$(11\ eV)^2$
TOTAL:	$(24.3\ eV)^2$
MEASURED: (2/26/98), (3/10/99)	$(25.4\ eV)^2$, $(26.1\ eV)^2$

Table 5.2: Noise sources added together along with measured resolution.

The sum (in quadrature) of the noise sources considered so far add up to 24.3 eV. This agrees well with the measured resolution from the data of Fig. 5.4.4 for XN93. The error bars suggest that there might possibly be unexplained noise sources up to ≈ 10 eV, but it appears that most of the major noise sources have been accounted for.

5.4.3 Additional Noise Sources

The best resolutions for the device are 25.4 ± 2.1 eV obtained on 2/26/98 and 26.1 ± 3.6 eV obtained on 3/10/99. The length of time between the two measurements suggest that the device itself is very robust to aging and thermal cycling. The readout, however, is less than reliable, as the detector is very sensitive to external disturbances. The appearance of these disturbances vary from run to run and often cause the resolution to be larger, in some cases much larger, than 26 eV. The most common external disturbances are electrical and RF pick-up, trapped flux and poor Josephson current suppression. Although most of these disturbances can be avoided with extra care taken in the experiment, a practical detector will need a very stable electromagnetic environment to perform reliably well.

The noise sources discussed so far do appear to constitute the majority of the energy width, as seen in table 5.2. To complete the discussion, however, we will now list three other noise sources which we have identified. From the analysis above, these sources can contribute at most ≈ 10 eV, and in all likelihood contribute less than that. However, their existence is important, as they have either contributed to past experiments or may be relevant for future ones.

(1) Spatial Noise: Absorption events in different parts of the device may result in different signal charges due to spatial asymmetries in the detector. This is commonly referred to as

spatial noise. It is seen by several other groups in the field, and is in fact a limiting factor in the energy resolution for some of them [den Hartog, 1999]. Our detector is less susceptible to spatial noise than most other groups because we employ a *lateral* geometry as oppose to a *vertical* geometry. In a lateral geometry the absorber is to the side of the junction, whereas in a vertical geometry the absorber is on top of the junction. With a lateral geometry the quasiparticles can spread out uniformly in the absorber before they reach the tunneling region, thus obscuring any differences between different absorption locations. Conversely, in a vertically stacked device the quasiparticles can tunnel almost immediately upon being generated, since there is no lateral diffusion. In this case the tunneling current is more sensitive to the absorption location. For example, in vertically stacked devices spatial non-uniformity in the width of the tunnel barrier can cause slightly different tunneling rates for different absorption locations, resulting in extra energy width. Note, however, that there is a trade-off: by using a lateral geometry we reduce the spatial noise but at the same time stretch out the pulse and reduce the signal current relative to the noise. This places larger demands on the electronic noise than for vertically stacked devices.

We consider the different absorption locations in the x, y and z directions in our detector. In Fig. 5.4.5 we re-draw the device to show the orientation. Absorption events at different x values are accounted for in our two junction geometry: the ratio of the charges tells the location in x. If different x values gave different average signal charges we would see this in the Q_{tot} vs. x_0 plots (Fig. 5.4.2). Since we see the same average charge throughout the absorber, we conclude there is not significant spatial noise in the x-direction.

Absorptions at different z values present a possible noise source due to the physics of the initial relaxation (hotspot). For a significant part of the initial relaxation, a majority of the photon energy lies in pairbreaking phonons, which can escape to the substrate. The amount of energy lost to the substrate can depend on the z value of the absorption location: events closer to the absorber-substrate interface might lose more phonons than events closer to the top of the absorber. This results in extra energy width. The total size of the hotspot is large, $\approx$ 3-5 μm, much larger than the thickness of the film. Therefore there is almost certainly some energy loss to the substrate via pairbreaking phonons. How much z-dependence this results in we cannot say for sure, although if it exists at all it is most likely in the $\approx$ 10 eV range, as per above. This could be tested by different size absorbers and/or depositing the absorber on a thin membrane of Silicon Nitride and etching away the substrate [Hypres, 1999].

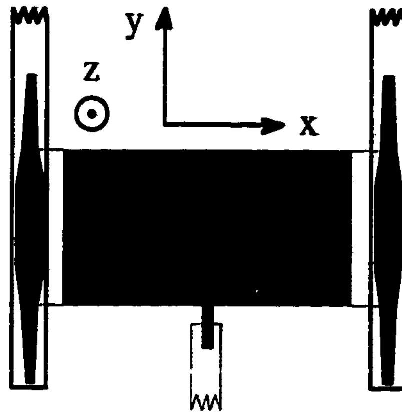

Fig. 5.4.5: Device re-drawn to show orientation for spatial noise.

Spatial noise in the y-direction appears to be relevant in our devices. Earlier in the section we saw how the energy width gets worse in the center of the device. We believe this to be due to quasiparticle loss at the niobium contact. The contact is located in the center of the device, but only contacts the bottom side of the absorber (Fig. 5.4.5). Niobium is well known to form metallic sub-oxides which could form local trapping sites for quasiparticles. For a given x location, the various y locations will be located at different distances from the contact, and hence will lose different amounts of charge. This results in spatial noise. One would expect that, as a function of x, this noise gets worse near the center. This is clearly what is observed in the Q_{tot} vs. x_0 diagram (see Fig. 5.4.2), so this explanation seems to be reasonable.

This source of spatial noise limits the resolution when looking at events from the entire absorber. A histogram (not shown) from the whole absorber shows a resolution of 87 eV FWHM, significantly larger than for the selected ranges above. This would appear to be a serious concern for future detectors, as one would either have to mask off the center region or use a different contact scheme. However, newly made devices do not show this behavior of extra broadening in the center. It is possible that this might be some kind of aging effect. The device with the extra noise was made in 1993, and the experiment was not sensitive enough to see the effect until late 1995, over two years later. We will watch this issue carefully with newly fabricated devices. We have designed and fabricated devices with different contact schemes, but if this effect does not reappear in future devices these new schemes will not be necessary.

(2) Digitizing Noise: One of the major improvements in the energy resolution came with the realization that there is extra noise added by the digitizing of the pulse. The oscilloscope

takes a voltage signal V_{signal} and digitizes it into bins of size ΔV. Since there is noise from the front end amplifier of the oscilloscope, the digitizing adds a fluctuation to V_{signal} of order $\pm \Delta V$. This results in extra noise in the signal if $\Delta V / V_{signal}$ is comparable to $\Delta E/E_x$.

The oscilloscope has 8 bits of voltage resolution, meaning it can resolve a voltage ΔV of $1/(2^8) = 1/256$ times the full scale voltage. The full scale voltage is the voltage per division times 8 divisions. Older experiments had used a scale of 400 mV/division or 3.2 volt full scale, where ΔV = 12.5 mV. This scale was chosen so that events with the highest peak currents are not clipped off. For events near the end of the absorber, the peak current can be as high as ≈ 270 nA, which corresponds to 2.7 volt after the gain of our amplifier. The next scale, 200 mV/division and 1.6 volt full scale (ΔV = 6.25 mV), was too small to include the largest pulses. Since the 400 mV scale has a larger ΔV one might expect some digitizing noise.

In order to determine the magnitude of the digitizing noise there was we injected current pulses into the amplifier and measured their resolution on different scales. We used both a warm 1 MΩ resistor and a cold junction at the input. The injected pulses were chosen to be similar in size to those from the *center* of the absorber, with a peak current of about 60 nA or 600 mV at the output. Thus we could shrink the scale to make ΔV smaller. The results are shown in table 5.3:

Scale	ΔV	Pulses, 1 MΩ	Pulses, Jct.	X-rays
400 mV/div	12.5 mV	28 eV	28 eV	36 eV
200 mV/div	6.25 mV	18 eV	18 eV	25 eV
100 mV/div	3.125 mV	15 eV	17 eV	----

*Table 5.3: Digitizing noise. * From the data of 2/26/98; the data from the 400 mV/div scale was filtered with the same filter as the 25 eV data.*

It is clear that there is digitizing noise on the 400 mV scale, possibly even a little on the 200 mV scale. After doing the injection experiments we started taking x-ray data on the 200 mV scale. This clipped off some of the larger pulses from the edge, but we were still able to get the pulses from approximately –85 μm to +85 μm and see good resolution. This is shown in the table where we took x-ray pulses on two different scales. The change from 400 mV/division to 200 mV/division is consistent with ≈ 21-24 eV of energy width for

both injected pulses and x-rays. We have now purchased a new oscilloscope which has 12 bits of resolution, for which similar tests have shown that the digitizing noise is negligible.

(3) Substrate events: Another significant improvement in the device performance came with the recognition that x-ray events in the substrate can add to the energy resolution. Events in the substrate cause a small signal in the detector due to the creation of $> 2\Delta$ phonons which propagate into the junction and break Cooper pairs. The substrate events add uncertainty to the integrated charge when they overlap in time with a real x-ray event. This has been discussed in detail previously [Friedrich, 1997b]. Analysis of the signals from substrate events suggested that they can cause a charge signal of 10^4 electrons or greater even when the absorption location is as far as 700 μm away from either of the two junctions. This number was confirmed experimentally by counting the number of such events. Our solution to the problem thus far has been to use an x-ray source weak enough such that there are not enough substrate events to have significant time overlap with pulses from the absorber. However, future astronomical observations may have to face this problem when looking at bright sources. The problem can be addressed by masking the substrate or etching it away to leave the device on a thin membrane of Silicon Nitride [Hypres 1999].

5.4.4 Summary

The energy resolution of our device is 25 –26 eV over a range of ≈ 14-18 μm on either side of the detector. The major noise sources that we have identified – statistical noise, electronic noise, and bias fluctuations – add up to approximately the same energy width. The possible remaining noise sources include spatial noise in the Y or Z direction, digitizing noise or substrate events, which combined add up to at most 10 eV of noise. The energy resolution over the whole absorber is limited by Y-dependence from quasiparticle loss at the Nb contact, which broadens the resolution at the center to 87 eV. Newer devices do not show this effect. Elimination of the known noise sources should bring the resolution to near the statistical limit, ≈ 5 eV

5.5 Spatial Resolution

The double junction configuration that we employ in our detectors allows for intrinsic 1-D imaging without the use of multiple pixels and readouts. It is this feature which makes our detectors attractive for x-ray astronomy, since x-ray observations are

done on a rocket or satellite where power and complexity issues are dominant. In this section we will estimate the spatial resolution of the detector.

An estimate of the spatial resolution is possible through a "propagation of errors" formalism. Simply speaking, we compute the location (x_0) by taking the ratio of the two signal charges (Q_1,Q_2), so the uncertainty in the location is related to the uncertainty in the two charges. From equations (5.4.1) we can write the fractional charge uncertainty $\Delta Q/Q$ in terms of the energy resolution ($\Delta E/E$) in the presence of absorber loss. This yields

$$\frac{\Delta Q}{Q}=\frac{\Delta E}{E}\left[2+\sinh^2\left(\alpha_L\left(1/2+x_0/L_{abs}\right)\right)+\sinh^2\left(\alpha_L\left(1/2-x_0/L_{abs}\right)\right)\right]^{-1/2}, \quad (5.5.1)$$

where L_{abs} is the absorber length and α_L is the loss parameter, as before. We have assumed that the charge uncertainties ΔQ_1 and ΔQ_2 are equal ($\Delta Q_1 = \Delta Q_2 = \Delta Q$). Using the same relations we can then solve for the fractional spatial resolution, $\Delta x_0/L_{abs}$:

$$\frac{\Delta x_0}{L_{abs}}=\frac{\Delta Q}{Q}\sqrt{\left(\frac{\sinh\left(\alpha_L\left(1/2+x_0/L_{abs}\right)\right)}{\alpha_L}\right)^2+\left(\frac{\sinh\left(\alpha_L\left(1/2-x_0/L_{abs}\right)\right)}{\alpha_L}\right)^2}\ . \quad (5.5.2)$$

An energy resolution of 87 eV (across the whole absorber) centered about x_0 = 0 µm, corresponds to a spatial resolution of 1.2 µm. Note that L_{abs} = 200 µm, and that $-L_{abs}/2 < x_0 < L_{abs}/2$. An energy resolution of 26 eV centered about x_0 = 75 µm corresponds to a spatial resolution of 0.4 µm. Both calculations assumed a value of α_L = 1.6. A spatial resolution of 0.4 µm over a 14 µm range (-83 µm to –69 µm) is 35 pixels, and over an 18 µm range (+67 µm to + 85 µm) is 45 pixels. A 1.2 µm spatial resolution over the remaining 148 µm is 123 pixels. Combining these we find that we have over 200 pixels across the whole absorber, with just two channels of readout. If we can achieve 0.4 µm across the whole absorber, that would correspond to well over 300 pixels.

A direct measurement of the spatial resolution in our type of detector is somewhat difficult, and has not been done by our group. One would need to confine the x-rays to a spot smaller than the expected Δx_0, i.e. to less than a 1 µm spot. This is difficult to do at present. One could do it lithographically, by fabricating an absorber with a small (> 1 µm) region of increased thickness. This region would then absorb more x-rays, and one could then histogram the resulting x_0 values and measure the FWHM.

5.6 Toward the Fano Limit

Having now quantified what noise sources limit the device performance, the question naturally arises as to what changes can be made to increase the energy resolution. In this section we will outline the suggested improvements to reduce the noise sources that we have discussed. We will consider each change and its effect on the noise sources individually. Each improvement is targeted toward one or two specific noise sources. We will then scale the noise from its present, measured value to a new, predicted value following each improvement, thus giving us a realistic forecast of future performance.

One of the major factors in the noise being at its present value is incomplete thermalization of the quasiparticles, discussed in section 4.2. The incomplete thermalization results in noise from bias voltage fluctuations, a decreased value of R_{eff}, and excess statistical noise from cancellation. Some of the suggested changes are therefore aimed at improving the cooling, such that more quasiparticles are below an energy (eV_{dc} + Δ) in the trap electrode before they tunnel. There are two major ways to do this. The first is to simply bias at a higher voltage, which increases the energy eV_{dc}. The second is to increase the tunnel time, allowing the quasiparticles to scatter to lower energy before they tunnel. Both of these changes involve re-designing the junction, either changing the junction shape, area, or the electrode volumes.

In our devices the bias voltage is limited to $\approx$ 70 μV because of Fiske modes (see I-V curve in Fig. 2.2.1). In order to bias at higher voltage one should re-design the junctions shape such that the Fiske modes are pushed up to higher voltage. This is done by reducing the length of the junction, since the voltage of the first Fiske mode scales inversely with the length [Eck, 1964]. We have fabricated and tested new junction shapes where the length is smaller, and the Fiske modes do indeed move to higher voltage. These devices, however, also have a reduced area, which is not good for x-ray detection (see below).

In redesigning the junction size and trap volume one needs to keep in mind the constraints imposed by recombination. One can easily introduce excess thermal or self-recombination, resulting in the loss of signal. At present we see very little signal loss due to either thermal or self-recombination ($\approx$ 3% for both), so one should try to keep similar conditions with the re-designed junctions. The key is to maintain the same ratio of tunnel time (τ_{tun}) to the recombination times ($\tau_{thermal}$, τ_{self}). The present tunnel time is 2.4 μs, with a junction area of A_{Jct} = 1800 μm^2 and a trap volume of V_{tr} = 700 μm^3. The tunnel time scales directly with the trap volume and inversely with the junction area, so we can write

$$\tau_{tun} = 2.4\mu s \cdot \left(\frac{V_{tr}}{700\mu m^3}\right)\left(\frac{1800\mu m^2}{A_J}\right). \tag{5.6.1}$$

The present self-recombination time is 96 μs, which is calculated from an average quasiparticle density of 0.75 million electrons in a 700 μm^3 trap volume. The self-recombination time scales directly with the volume, so we can also write,

$$\tau_{self} = 96\mu s \cdot \left(\frac{V_{tr}}{700\mu m^3}\right). \tag{5.6.2}$$

At present, the ratio $\tau_{self}/\tau_{tun} = 40$. Combining equations (5.6.1) and (5.6.2) we see that the volume dependence cancels and that in order to keep a ratio of 40 or greater we must keep the junction area greater than or equal to 1800 μm^2. This results in a very important conclusion, namely, *in order to avoid self-recombination we can not reduce the area of the junction.* This was perhaps not recognized previously, as shrinking the junction had always been thought to be a good idea to reduce the shot noise. Note that the same conclusion holds true for increasing the barrier thickness.

The present thermal recombination time is $\tau_{thermal} = 200$ μs, so $\tau_{thermal}/\tau_{tun} \approx 80$. The thermal recombination time is constant with the junction shape and size, as it depends only on the density of thermal quasiparticles. Thus, we must keep τ_{tun} the same in order to keep the ratio the same. One could perhaps increase τ_{tun} by a factor of 2, which would bring $\tau_{thermal}/\tau_{tun}$ down to 40, the same ratio for self-recombination. If the bath temperature is decreased to 0.1 K, however, the thermal recombination time goes up by orders of magnitude, which would allow a much larger increase in tunnel time. Note that the increase will have to be achieved by a larger trap volume, since self-recombination prevents shrinking the junction area.

Two good indicators of the extent of the quasiparticle cooling are the percent of the initial charge that is collected (Q/Q_0) and the slope of the Q vs. V_{dc} (dQ/dV). In Fig. 5.6.1 and 5.6.2 we show these quantities calculated from the simulation of the current pules. Their dependence on bias voltage and tunnel time is shown to indicate the effects of these improvements.

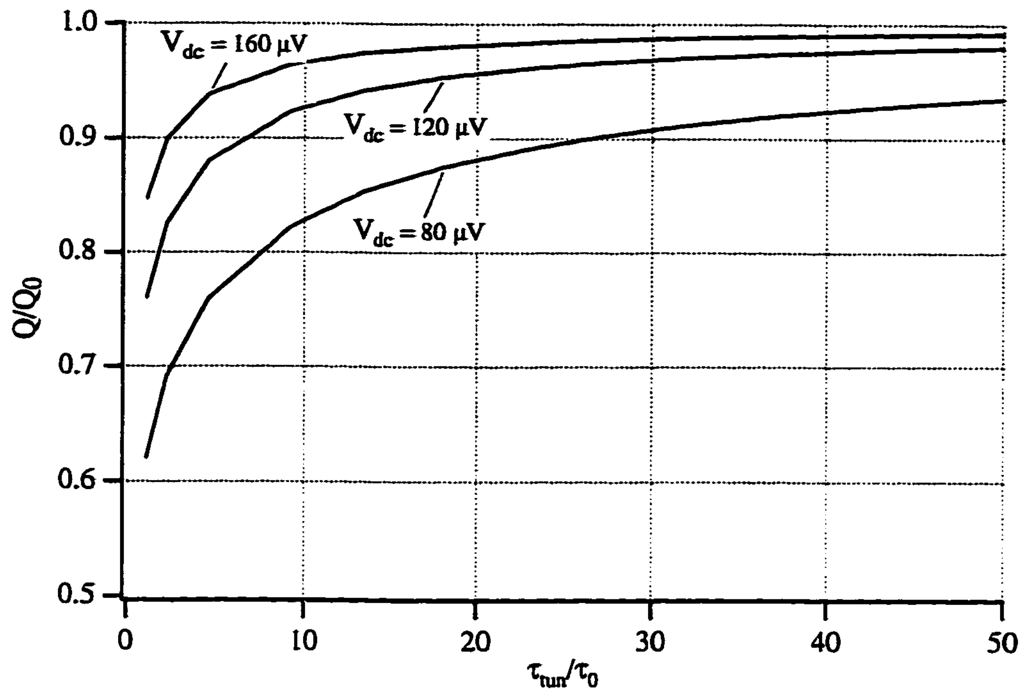

Fig. 5.6.1: Calculated improvement in the charge collection from increasing the tunnel time. Longer tunnel times result in improved thermalization.

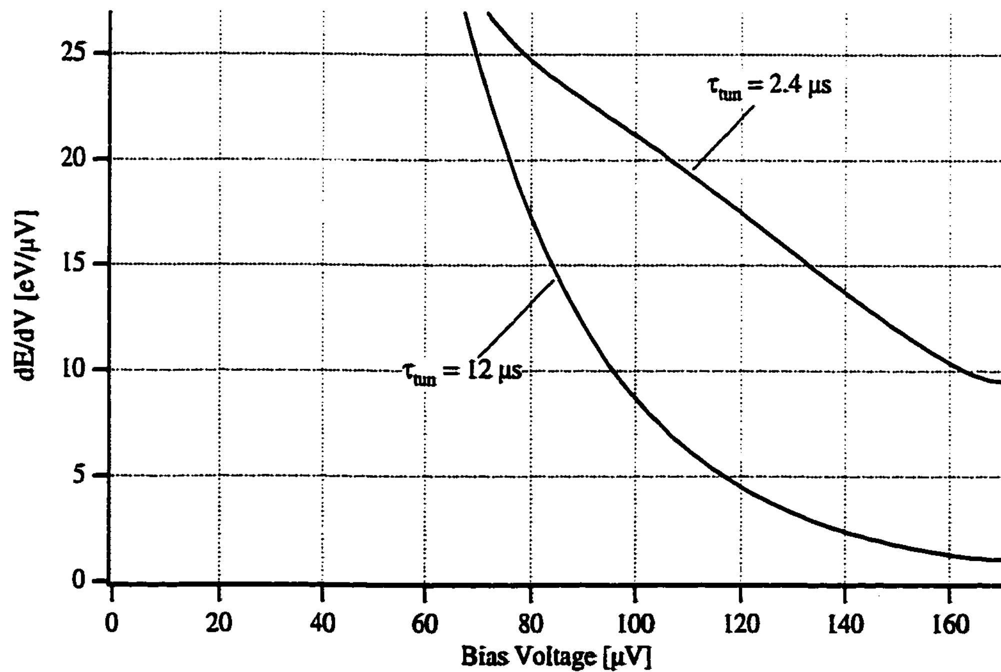

Fig. 5.6.2: Calculated improvement in the slope of the charge versus bias voltage (dQ/dV) due to biasing at higher voltage. The charge has been normalized into energy units (dE/dV).

Besides improving the cooling, other changes will be effective in reducing various noise sources. The shot noise can be reduced by reducing the bath temperature. The feedback resistor can be put on the cold stage to reduce its Johnson noise. The amplifier can be AC coupled to reduce the bias voltage fluctuations, although it is not yet clear in detail how this should be done. A possibility is to use *two* amplifiers which work at separate frequencies, one to bias the junction at DC and one to read out the pulse. One might then be able to reduce the bias fluctuations while still maintaining the stiff load line. Finally, backtunneling can be used to increase the signal relative to all sources of electronic noise (not bias fluctuations, however). At present, we have 5.2 eV statistical noise from backtunneling, but only about a factor of two increase in signal ($\bar{n}$ = 2.5). If we went to the limit of large backtunneling, the statistical noise would only increase to 6.2 eV but the signal increase could be as much as 10 times more ($\bar{n}$ = 20). One should keep in mind that this also lengthens the pulse by the same amount (x 10), which adds $\sqrt{10}$ to all electronic noises because the noise is integrated for longer. However, the gain in signal of more than compensates, as there is an overall improvement in energy width of $(10 / \sqrt{10}) = \sqrt{10}$ for the various components of electronic noise.

We now list each improvement and detail its effect on the major noise sources. We then present a table (table 5.4) of the improvements, with a total, predicted resolution following each change. In the table each change is cumulative, i.e. the resolution is calculated assuming all previous changes. The abbreviations for the noise sources in the table are shown in boldface in the list below. We have assumed that the Fano and trapping noise (**F/T**) stays the same with all changes. The improvements are presented in order of difficulty to implement, taking into consideration that some improvements are only worthwhile after others. In the table underlined entries are the noise sources which were affected by the change for that row.

(1) Newer Devices: The most recent devices made do not show significant absorber losses, nor do they show the extra broadening in the center. This will reduce the contribution from absorber loss (**Loss**).

(2) Higher DC bias voltage (V_{dc} = 150 μV): Discussed above, this results in better cooling. It will be achieved by changing the junction shape. Voltages higher than 150-160 μV seem difficult at this point due to the increase in subgap current observed above $V_{dc} = \Delta/e$. Assuming the tunnel time remains the same, increasing V_{dc} to 150 μV results in an increase in Q/Q_0 from 77% to 94%, which reduces the cancellation noise (**Can.**). It also reduces

the value of dQ/dV by a factor of two, which reduces the bias voltage fluctuations (**Bias**) and the value of R_{eff}, which reduces the voltage noise (**Volt**).

(3) More Backtunneling (BT): This will be achieved by using a higher gap wiring layer to prevent quasiparticles from diffusing away from the junctions. We have seen about a factor of 20 increase in backtunneling ($\bar{n}$ = 20) in such devices made for optical photons, so we assume this is achievable. This reduces all electronic noises by $\sqrt{\bar{n}}$: shot noise (**shot**), Johnson noise of R_f (**R_f**) and voltage noise. The statistical noise from backtunneling (**BT**), however, will increase. Note also that backtunneling further reduces the cancellation noise.

(4) Cold Feedback resistor: The feedback resistor can be put on the cold stage, reducing its Johnson noise by the amount $\sqrt{(300K/T_{bath})} \approx 14$. We have done tests with cold feedback resistors and verified that they do show the correct noise decrease with cold resistors in place of the junction. The stray capacitance from the leads going down the feedback resistor, however, is an issue that needs to be dealt with.

(5) New Bias Circuit: Using a transimpedence amplifier other than the A250 or AC coupling the A250 with a different bias circuit would both be possible. The objective would be to increase the bias stability, ΔV_{rms} from section 5.2. AC coupling the amplifier reduces the bias fluctuations by about a factor of 3, so we will assume that for the table.

(6) T = 0.1 K: Reducing the bath temperature will reduce the junction shot noise. If the thermal current continues to follow BCS, as it does down to T = 0.2 K so far, it will be reduced by a factor of 35,000. This may not in general be true, as leakage current may limit the reduction. However, a factor of 100 would seem reasonable, which would reduce the shot noise by $\sqrt{100} = 10$.

(7) Longer Tunnel Time (5x): This also improves the cooling, as discussed above. This improvement is only possible after reducing the bath temperature to 0.1 K, due to thermal recombination (see above). The longer tunnel time decreases the value of dQ/dV by another factor of 3, so the voltage noise and bias fluctuations will reduce by the same amount. It is also desirable, at this point, to remove backtunneling, as the extra signal is no longer necessary to reduce the electronic noises. Removing backtunneling then eliminates its statistical contribution. Removing backtunneling also reduces dQ/dV by a factor of 3

instead of 2 from the V_{dc} = 150 μV change. This is because backtunneling itself adds a little voltage dependence of its own.

(8) RF-SET: This is the subject of other work presently going on at Yale [Schoelkopf, 1998]. The RF-SET is an amplifier that works at low temperature and has extremely low charge noise. At the point in the table where it is inserted, it will not improve the resolution any, but the low power dissipation and the decreased complexity make it a very attractive option for future astronomical observations.

Change	Shot	R_l	Volt	Bias	BT	Can.	Loss	F/T	Total
Present	7.2	9.4	16	11	5.2	2.6	2.3	4.5	24.3
New Devices	7.2	9.4	16	11	5.2	2.6	1.4	4.5	23.9
V_{dc} = 150 μV	7.2	9.4	8	5.5	5.2	0.9	1.4	4.5	16.9
More BT	2.3	3.0	2.5	5.5	6.2	0.1	1.4	4.5	10.6
Cold Rf	2.3	0.2	2.5	5.5	6.2	0.1	1.4	4.5	10.1
New Bias	2.3	0.2	2.5	1.8	6.2	0.1	1.4	4.5	8.7
T = 0.1 K	0.2	0.2	2.5	1.8	6.2	0.1	1.4	4.5	8.4
5xτ_{tun}/no BT	0.6	0.6	1.8	0.6	0.2	0.1	1.4	4.5	5.2
RF-SET	0.6	0.6	1.8	0.6	0.2	0.1	1.4	4.5	5.2

Table 5.4: Projected improvements in the energy resolution due to changes in the detector and experiment.

The improvements listed above, if successfully implemented, will make these detectors a very valuable tool for x-ray astrophysics. The ability to do high resolution spectroscopy (E/ΔE ≈ 1000) and spatial imaging beyond 50 pixels or so has yet to be accomplished with any existing detector. The fact that this performance can be potentially realized with only a few readout channels means that the long term possibilities for these detectors cannot be overlooked. Our group is presently looking [Li, 1999] into the possibility of doing 2-dimensional imaging with 4 junctions connected to a single absorber. Even with the present energy resolution of 25 eV, such a device could offer thousands of pixels for imaging with only four readout channels. If both the projected spatial and energy resolution can be realized in such a detector, it would indeed be a very useful observational tool.

Of course, it is also clear from above that we are still some ways away from accomplishing these objectives. The work done in this dissertation has taken the next step

toward these goals. We have been able to understand the dominant physical mechanisms that affect the signal and the noise in these devices, and also been able to measure their contribution to the detector's performance. The fact that the known contributions of the noise add up to the measured energy resolution is a big step in this research, and has yet to be accomplished by any other STJ group at 6 keV. However, we still have to take the next step in order to make an impact on actual astronomical observations. If we can do so, and the remaining problems can be solved, these devices could lead to new areas of discovery in astrophysics.

Appendix A: Sample Parameters

	XN93	F99-11C	F99-14C
Dimensions:			
Absorber	200x100x0.6 =>12000 μm^3	200x100x0.57 =>11400 μm^3	200x100x0.57 =>11400 μm^3
Trap	4700x0.15=>700 μm^3	3060x0.21=>517 μm^3	4666x0.21=>839 μm^3
Junction	20x200=>1860 μm^2	8.75x112.5=>459 μm^2	17.5x192.5=>1572 μm^2
CE+Wiring	2800 μm^3	9133 μm^3	368 μm^3
Electrical:			
R_{nn}	0.5 Ω	1.4 Ω	0.4 Ω
I_c	500 μA	205 μA	675 μA
I_{bias}	25 nA	9 nA	760 nA
R_{dyn}	10 kΩ	>50 kΩ	90 Ω
Pulse Fits:			
τ_{trap}	10 ns	10 ns	----
D	8.5 cm^2/s	9.5 cm^2/s	----
τ_{loss}	30 μs	>1 ms	----
Q_o	$8.0x10^6$ e	$8.8x10^6$ e	----
τ_{out}	7.1 μs	5.0 μs	----
$\tau_{tun,tr}$	2.4 μs	5.0 μs	2.1 μs
$\tau_{tun,ce}$	9.6 μs	88.0 μs	0.9 μs
Fabrication:			
Absorber	• 6000 Å Ta, dc sputtered at 40 Å/s • substrate temp.=700 C • RRR=30	• 5700 Å Ta, dc sputtered at 38 Å/s • substrate temp.=750 C • RRR=17	• 5700 Å Ta, dc sputtered at 38 Å/s • substrate temp. = 750 C • RRR=17
Contact	• 2000 Å Nb, dc sputtered at 10 Å/s	• 2400 Å Nb, dc sputtered at 10 Å/s	• 2400 Å Nb, dc sputtered at 10 Å/s
Trap	• 1500 Å Al evaporated at 200 Å/s • RRR=13	• 2100 Å Al, evaporated at 200 Å/s • RRR=12	• 2100 Å Al, evaporated at 200 Å/s • RRR=12
Barrier	• Thermal oxidation at 600 mT for 3 hours	• Thermal oxidation at 500 mT for 2 hours	• Thermal oxidation at 500 mT for 2 hours
Junction	• 700 Å Al, evaporated at 15 Å/s	• 800 Å Al, evaporated at 20 Å/s	• 800 Å Al, evaporated at 20 Å/s
Via	• 1500 Å SiO, evaporated at 14 Å/s	• 2700 Å SiO, evaporated at 15 Å/s	• 2700 Å SiO, evaporated at 15 Å/s
Wiring	• 3000 Å Al, evaporated at 40 Å/s	• 3650 Å Al, evaporated at 30 Å/s	• 3650 Å Al, evaporated at 30 Å/s

Appendix B: Data Analysis Procedure

In our experiment, the data are taken completely raw, with no filtering or analysis performed on it prior to being saved. The extraction of the physical parameters and the energy resolution is all done digitally with software. Here we outline the procedure to analyze a set of data.

A. Overview

1. Display I_1 vs. I_2 and Q_1 vs. Q_2 (can use "Kraus Processor" program). Check magnitude of I and Q versus amplifier gain and scope settings.
2. Using the Kraus formula to extract location (x_0), plot ($I_1 + I_2$) and ($Q_1 + Q_2$) versus x_0.
   - Is device uniformly illuminated? (check triggering if not!)
   - Check for α and β line, check linearity.
   - Correct curvature with Kraus formula, note value of α_L. Generate corrected Q_{tot} wave.
3. Bin values of Q_{tot} into a histogram, check resolution of unfiltered pulses (typically 100-200 eV).
4. Save Q_{tot} and x_0 waves.

B. Pulse Shapes

1. Produce the different waves representing the pulse shapes: Risetime, Falltime, Q_1, Q_2, I_1, I_2, Delay time (for at least 2 different threshold currents). In generating the peak current waves (I_1, I_2) and the delay time waves the pulses should first be filtered digitally with a 500 kHz low-pass filter. This is to get rid of the amplifier overshoot. (The "Digital Processor" program can be used for this step.)
2. Display the waves as: Q_1 vs. Q_2, I_1 vs. I_2, Risetime vs. x_0, Falltime vs. x_0, Delay time vs. x_0.
3. Set the physical constants in the current pulse model: materials constants (density of states, energy gap, electron-phonon time), device constants (absorber length, electrode volumes, tunnel time) and experimental constants (temperature, bias voltage).
4. Do some preliminary fitting with current pulse model to get a general idea of the range of fit parameters needed to match the data. Try to match currents/charge in the center and one point on the side, with educated guesses for the simulation parameters. The loss parameter (α_L) is already known from above.
5. Detailed fitting:
   - Vary τ_{trap} in the model to fit the charge division near the edges. (This will be a somewhat weak dependence).

- Vary the diffusion constant D to fit the delay times. Start with a single location, but check two or three different locations to make sure the fit is good. Check at least two threshold currents.
- Vary the value of Q_0 to match the peak current in the center. Check one or two other locations for quality of fit.
- Vary the value of τ_{out} to match the total charge.

6. Run the "Absorber Scan" program to generate fits for the whole absorber, put the output onto the plots with the data. Repeat step 5 until fits are satisfactory.
7. Iterate 5 and 6 as necessary for different experimental conditions (temperature, bias voltage, series resistance, etc.)

C. Energy Resolution

1. First, look at the electronic noise spectra. Check that the levels agree with amplifier gain and scope settings. Check if the white noise level agrees with the sum of the known noise sources. Check that the high frequency roll-off and the 1/f knee are in the right place. Have an idea what the expected electronic noise is in eV units.
2. Check a few different filters (the best ones from previous runs and/or the best guess for the optimum). Do a preliminary scan of the relevant parameters for each filter:
   - Check the value of α_L, both by hand and letting the computer fit it. It should be different from the unfiltered value above, but approach it as the filtering gets weak. Make sure the computer is fitting it well.
   - Do a charge histogram with events from the whole absorber. Make sure that it is better than the unfiltered value found from above. Restrict the location and note how the resolution improves. Try to get an idea of the "sweet spots" where the resolution is best.
   - Check how the energy resolution depends on the binning of the histogram. Get an idea of the valid range of binning where there are no artifacts.
   - Check how much baseline averaging affects the resolution.
3. Vary the filter cut-off frequencies a little more, try to get an idea where the resolution is best. Re-check location cuts and baseline averaging at a few more filters to make sure the optimum has been found from above.
4. Use the above information to do a filter scan. Include cut-off frequencies above and below the ones found in the preliminary scan to make sure the minimum is found. Average over enough bins to validate the results.
5. Find the optimum resolution of the filter scan. Check by hand any resolution that looks too high or two low (the FWHM values should vary somewhat continuously).
6. Repeat filter scans for different location cuts to find the true minimum, for different experimental conditions, or for electronic pulses.

Appendix C: Dates of Important Data Runs

Date	Summary
1/20/97	First test of bias dependence, followed by explanation of canceling tunneling processes. Poor signal due to shorter outdiffusion time - $\Delta E \approx 90$ eV.
11/21/97	First successful test of combined current/voltage bias. Still need warm series resistance ($\approx 50\ \Omega$) to keep bias stable.
12/16/97	X-rays with different values of series resistance, see curvature in Q_1 vs. Q_2 change. Charge division gives first estimate of R_{eff}. $\Delta E \approx 75$ eV.
2/26/98	Use cold 100 Ω to keep bias stable. Use compensation capacitance of 30 pF to improve amplifier stability. Take x-rays on 200 mV/div scale to reduce digitizing noise. $\Delta E = 25$ eV. Vary series resistance to measure R_{eff}.
4/29/98	Resolution of ≈ 45 eV, but much worse (90 eV) close to one junction than other. Bias drift in that junction.
6/12/98	X-rays with different filtering in the nulling loop and also a different input FET (InterFET 3601). $\Delta E \approx 30$ eV.
8/12/98	X-rays with different values of feedback capacitance and compensation capacitance. Successful test of Passive Voltage Bias with warm $R_{parallel}$.
11/5/98	Cold resistor test with new Nicolet scope. See 1/f noise for the first time.
1/10/99	Warm resistor test reveals that 1/f noise is different for different A250 units.
1/11/99	X-rays with Passive Voltage Bias, cold 2 kΩ for $R_{parallel}$. Use shielded box. Another bias dependence test. $\Delta E = 55$ eV.
3/10/99	Return to active voltage bias, no shielded box or magnetic shield. X-ray measurements reproduce good energy resolution ($\Delta E = 26$ eV).
5/17/99	Measure value of bias voltage fluctuations by DC coupling scope with no x-rays and long averaging. $\Delta E \approx 40$ eV.
6/11/99	First test of small junction device F99-11C. Device shows significant self-recombination in the trap. $\Delta E \approx 45$ eV
7/9/99	First test of backtunneling device F99-14C. Device shows large charge output. $\Delta E \approx 60$ eV across whole absorber.

Appendix D: Active Voltage Bias Circuit diagram

Below we show the details of one channel of the active voltage bias circuit used to bias and read out a detector junction. In an actual experiment two such circuits are used, one for each junction. The electronic biasing and readout is discussed in chapter 2.

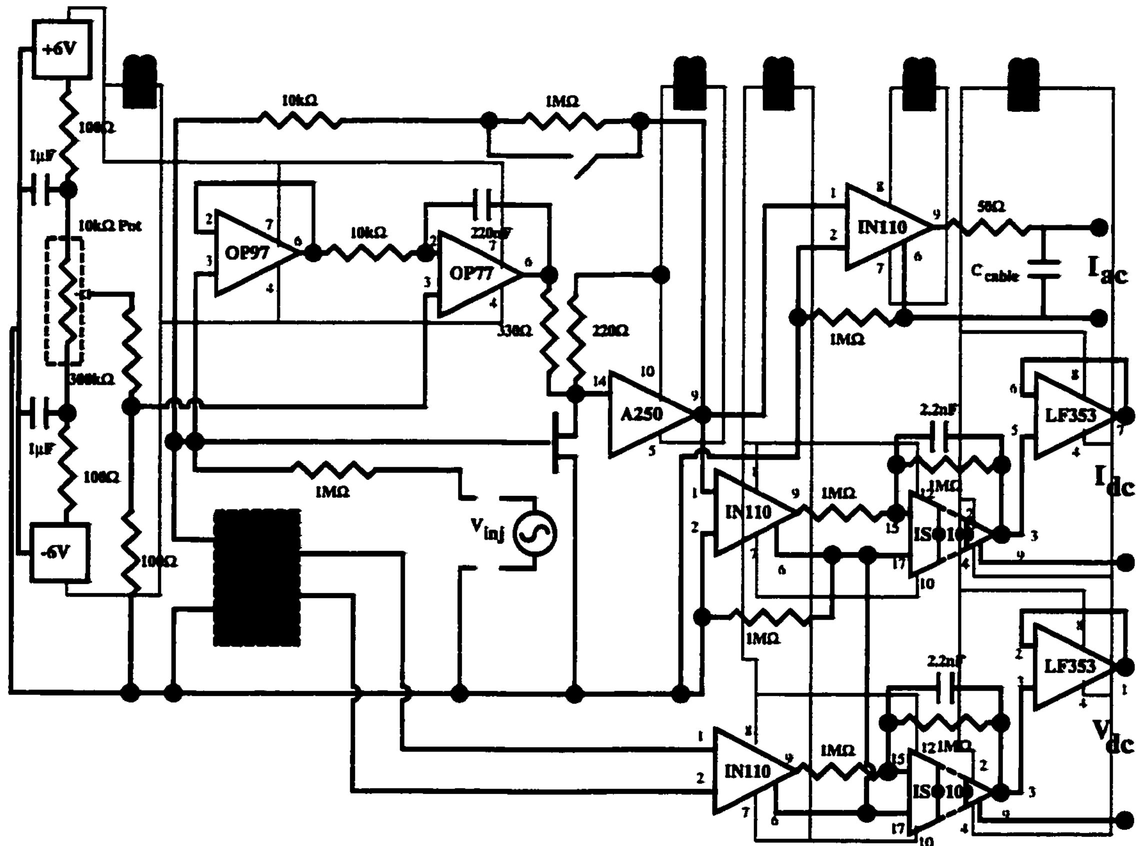

References

Bevington P. R. and Robinson D. K., *Data Reduction and Error Analysis for the Physical Sciences*, McGraw-Hill, New York (1992).

Burden R. L. and Faires J. D., *Numerical Analysis*, PWS-KENT, Boston (1989).

Charles P. A. and Seward F. C., *Exploring the X-Ray Universe*, Cambridge University Press (1995).

Cooper S., *Proceedings of the Seventh International Workshop on Low Temperature Detectors* , Max Planck Institute of Physics, Munich, Germany (1997).

Cristiano R., E. Esposito, L. Frunzio, C. Nappi, G. Ammendola, L Parlato, G. Pepe, H. Kraus and P. Walko, *J. Appl. Phys.* **86**, (1999).

de Korte, P. A. J., M.L. van den Berg, M.P. Bruijn, M. Frericks, J.B. le Grand, J.G. Gijsbertsen, E.P. Houwman and J. Flokstra, *Proc. SPIE* **1743**, 24 (1992).

den Hartog R., P. Verhoeve, A. Peacock, A. Poelaert and N. Rando, *IEEE Trans. on Appl. Supercond.* **9**, 3342 (1999).

Eck R. E., D.J. Scalapino and B.N. Taylor, in *Proceedings of the Ninth International Conference on Low Temperature Physics*, Daunt J. G. Editor, Plenum Press, New York (1964).

Fano U., *Phys. Rev.* **72**, 26 (1947).

Friedrich S., K.Segall, M.C. Gaidis, C.M. Wilson, D.E. Prober, P.J. Kindlmann, A.E. Szymkowiak and S.H. Moseley, *IEEE Trans. on Appl. Supercond.* **7**, 3383 (1997a).

Friedrich S., PhD Thesis, Yale University (1997b).

Friedrich S., K. Segall, M.C. Gaidis, C.M. Wilson, D.E. Prober, A.E. Szymkowiak, and S.H. Moseley, *Appl. Phys. Lett.* **71**, 3901 (1997c).

Friedrich S., private communication (1998).

Gaidis M.C., PhD Thesis, Yale University (1994).

Goldie D. J., P.L. Brink, N.E. Booth and G.L. Salmon, *Appl. Phys. Lett.* **64**, 954 (1994).

Gray K. E., *Nonequilibrium Superconductivity, Phonons and Kapitza Boundaries*, Plenum Press, New York (1980).

Halbritter J., *Appl. Phys.* **A43**, 1 (1987).

Horowitz P. and Hill W., *The Art of Electronics*, Cambridge University Press (1989).

Hypres Inc. and Yale University, *SBIR Collaboration* (1999).

Jochum J., H. Kraus, M. Gutsche, B. Kemmather, F. v. Freilitzsch and R.L. Mossbauer, *Ann. Phys.* **2**, 611 (1993).

Johnson D. E., Johnson J. R. and Hilburn J. L., *Electric Circuit Analysis*, Prentice Hall, New Jersey (1989).

Kaplan S. B., C.C. Chi, D.N. Langenberg, J.J. Chang, S. Jafarey and D.J. Scalapino, *Phys. Rev.* **B14**, 4854 (1976).

Kraus H., F. v. Freilitzsch, J. Jocum, R.L. Mossbauer, T. Peteerreins and F. Probst, *Phys. Lett.* **B321**, 195 (1989).

Kurakado M., *Nucl. Instr. Meth.* **A196**, 275 (1982).

Labov S. E. and Young B. A., *Proceedings of the Fifth International Workshop on Low Temperature Detectors*, J. Low Temp. Phys. **93** (1993).

Li L., L. Frunzio, K. Segall, C.M. Wilson, D.E. Prober, A.E Szymkowiak and S.H. Moseley in *Proceedings of the 8th International Workshop on Low Temperature Detectors, Nucl. Instr. Meth.* (2000) (in press).

Ott H. R. and Zehnder A., *Proceedings of the Sixth International Workshop on Low Temperature Detectors*, Amsterdam, Elsevier (1996).

Press W. H., B.P. Flannery, S.A. Teukolsky and W.T. Vetterling, *Numerical Recipes in Pascal,* Cambridge University Press (1989).

Reif F., *Fundamentals of statistical and thermal physics*, McGraw-Hill, New York (1965).

Schoelkopf R., P. Wahlgren, A.A. Kozhevnikov, P. Delsing and D.E. Prober, *Science* **280**, 1238 (1998).

Segall K., Friedrich S., C.M. Wilson, D.E. Prober, A.E. Szymkowiak, and S.H. Moseley in *Proceedings of the 7th International Workshop on Low Temperature Detectors*, Cooper S. ed., Max Planck Institute of Physics, Munich, Germany, A22 (1997).

Segall K., C.M. Wilson, L. Li, A.K. Davies, R. Lathrop, M.C. Gaidis, D.E. Prober, A.E. Szymkowiak, and S.H. Moseley, *IEEE Trans. on Appl. Supercond.* **9**, 3326 (1999).

Tinkham M., *Introduction to Superconductivity*, McGraw-Hill, New York (1996).

van den Berg M. L., F.B. Kiewiet, M.P. Bruijn, O.J. Luiten, P.A.J. de Korte, J. Martin, and R.P. Huebener, *IEEE Trans. on Appl. Supercond.* **9**, 2951 (1999).

Van Duzer T. and Turner C. W., *Principles of Superconducting Devices and Circuits*, Elsevier North Holland, New York (1981).

Verhoeve P., N. Rando, A. Peacock, A. van Dordrecht, B.G. Taylor, and D.J. Goldie, *Appl. Phys. Lett.* **72**, 3359 (1998).